Fabrication of photonic nanostructures for light harvesting in solar cells

by

Amalraj Peter Amalathas

BSc (Hons) with First Class in Physics, University of Jaffna

A thesis submitted in partial fulfilment of the

requirements for the degree of

Doctor of Philosophy

Department of Electrical and Computer Engineering

University of Canterbury

Christchurch, New Zealand

May 2017

Dedicated to my father, mother, sisters, and brothers

for their love, endless support and encouragement.

Abstract

Reducing optical losses in the solar cells has always been a key challenge in enhancing the power conversion efficiency of the solar cells without increasing significantly the cost. In order to enhance the power conversion efficiency of the solar cells, a number of light trapping schemes have been investigated to manipulate the light inside the absorber layer and to increase the effective optical path length of the light within the absorber layer of a solar cell. In this work, periodic nanopyramid structures were utilized as the light trapping nanostructures in order to improve the performance of the solar cells using low cost maskless laser interference lithography (LIL) and UV nanoimprint lithography (UV-NIL). In addition, a superhydrophobic property of the nanopyramids was explored to add a self-cleaning functionality to the front encapsulation.

Firstly, the inverted nanopyramid structures were fabricated on Si substrate by laser interference lithography and subsequent pattern transfer by combined reactive ion etching and KOH wet etching. Maskless LIL was employed as a high-throughput, high resolution and low cost for the fabrication of large scale periodic nanostructures. The periodic inverted nanopyramid structures on a silicon substrate were used as a master mold substrate for the imprint process. In the first nanoimprint process, the upright nanopyramid structures with light harvesting and hydrophobic properties were fabricated on the glass substrate by simple, high throughput and low cost UV nanoimprint lithography using Si master mold with inverted nanopyramid structures. The upright nanopyramids structured glass substrates were tested for protective cover glass for solar cells applications and were utilized as a mold for the second imprint process.

The diffuse transmittance and haze ratio values were significantly increased for the upright nanopyramid patterned glass, especially, in the wavelength range 300-600 nm

compared to the bare glass. This indicates that antireflection and strong light scattering functions due to the upright nanopyramid structures were achieved. The use of upright nanopyramids as a cover glass, lead to the power conversion efficiency of the encapsulated monocrystalline Si solar cell and commercially made polycrystalline Si solar cell to substantially increased about 10.888% and 8.216%, respectively. This is mainly due to the scattering and prolong the optical path length caused by the upright nanopyramid structures compared to the reference cells with bare glass. In addition, the fluorinated upright nanopyramid structured cover glass exhibited larger contact angle (θ_{CA} ~132°) and excellent self-cleaning properties for dust particles.

In the second nanoimprint process, the periodic inverted nanopyramid structures were fabricated on the monocrystalline solar cell and commercially made polycrystalline Si solar cell front surfaces using a UV nanoimprint lithography. The pyramid coating can be applied after cell fabrication to eliminate any losses due to surface damage by the etching processes. The inverted nanopyramid structures decreased the reflectance and increased the external quantum efficiency over a broad wavelength range. The periodic inverted nanopyramid structure has successfully reduced the Fresnel reflection and led to directing and trapping more incident light into the monocrystalline and polycrystalline Si solar cells, thereby improving the short circuit current density and enhancing the power conversion efficiency. The power conversion efficiency of the monocrystalline Si solar cell and the polycrystalline Si solar cell with inverted nanopyramid structures were improved by 11.733% and 6.869% compared to the planar solar cells, respectively. Moreover, the surface of the solar cells exhibited hydrophobic properties due to increased contact angle caused by the nanostructure patterns and the self-assembled monolayer coating. The enhanced hydrophobicity provided the solar cells with an added self-cleaning functionality.

Finally, the surface morphological, optical and electrical properties of ITO thin films prepared by RF magnetron sputtering and the fabrication of ITO films onto upright nanopyramid structured glass substrate were studied. The ITO films were conformally deposited onto upright nanopyramid structured glass substrate at optimized parameters.

These results suggest that the periodic inverted nanopyramid and upright nanopyramid structures with light harvesting and self-cleaning properties have considerable potential for various types of solar cells and optical systems in real outdoor environments.

Acknowledgements

I would like to express my sincere thanks and appreciations to my supervisor, Professor Maan Alkaisi for his excellent guidance, encouragement and support throughout my research and for his continuous support for publishing journal articles and presenting my work at the international conferences. I would also like to thank him for very careful review of the thesis, and for the comments, corrections, and suggestions in a short period of time. I also thank and acknowledge Associate Professor Martin Allen for serving as a co-supervisor and providing support.

I would also like to express my gratitude to all the people who have helped me in so many ways. In particular, I would like to thank Gary Turner and Helen Devereux for providing technical assistance and for freely sharing their knowledge and expertise. I am very grateful to Senthuran Sivasubramaniam for his tremendous guidance and support in my initial stage. I am also thankful to David Healy for helping me for making imprint mold. I am also grateful to my colleagues and friends Dr Giang Dang, Hari Murthy, Linda Chen, Claude Meffan, Nor Abd Wahid, Cletus Adams and Alana Hyland for a great time and all the invaluable help around the lab.

I would also like to thank Annette Koo, Callaghan Innovation for reflectance and transmittance measurements, Dr Jonathan Halpert and Elijah Peach, Victoria University of Wellington, New Zealand for EQE measurements. I would like to acknowledge the UC Doctoral Scholarship for providing funds during my studies.

My sincere gratitude goes to my friends, well-wishers and all of my former teachers for their support and encouragement of my education so far.

Last but not the least; I am most grateful to my father A Peter Amalathas, my mother Mariyanayaki, sisters and brothers for their endless love and support to my education, I could not have done this without your support!

List of publications and presentations

Some aspects of the work presented in this thesis have been published and presented as follows:

Publication in peer-reviewed journals

1. **Amalraj Peter Amalathas**, Maan M Alkaisi, "Periodic upright nanopyramid fabricated by ultraviolet curable nanoimprint lithography for thin film solar cells", International Journal of Nanotechnology, 14 (2017) 3-14.

2. **Amalraj Peter Amalathas**, Maan M Alkaisi, "Efficient light trapping nanopyramid structures for solar cells patterned using UV nanoimprint lithography", Materials Science in Semiconductor Processing, 57 (2017) 54-58.

3. **Amalraj Peter Amalathas**, Maan M Alkaisi, Upright nanopyramid structured cover glass with light harvesting and self-cleaning effects for solar cell applications, Journal of Physics D: Applied Physics, 49 (2016) 465601.

4. **Amalraj Peter Amalathas**, Maan M Alkaisi, "Effects of film thickness and sputtering power on properties of ITO thin films deposited by RF magnetron sputtering without oxygen", Journal of Materials Science: Materials in Electronics, 27 (2016) 11064-11071.

Publications in peer-reviewed conference proceedings

1. **Amalraj Peter Amalathas**, Maan M Alkaisi, "Enhanced Light Scattering and Hydrophobicity of Glass with Upright Nanopyramid Structure for Solar Cells Using UV Nanoimprint Lithography", Proceedings of 32nd European Photovoltaic Solar Energy Conference and Exhibition (EU PVSEC), (2016) 0245-0248.

2. **Amalraj Peter Amalathas**, Maan M Alkaisi, "Enhancing the performance of solar cells with inverted nanopyramid structures fabricated by UV nanoimprint lithography", Proceedings of IEEE 43rd Photovoltaic Specialists Conference (PVSC), (2016) 0346-0349.

Conference presentations

1. **Amalraj Peter Amalathas**, Maan M Alkaisi, "Nanopyramid Structures with Light Harvesting and Self-cleaning Functions for High Performance Solar Cells", 8th International Conference on Advanced Materials and Nanotechnology (AMN-8) , Queenstwon, New Zealand, Feb 12-16, 2017 (Oral presentation).

2. **Amalraj Peter Amalathas**, Maan M Alkaisi, "Enhanced Light Scattering and Hydrophobicity of Glass with Upright Nanopyramid Structure for Solar Cells Using UV Nanoimprint Lithography", 32nd European Photovoltaic Solar Energy Conference and Exhibition (EU PVSEC 2016), Munich, Germany, June 20-24, 2016 (Poster Presentation).

3. **Amalraj Peter Amalathas**, Maan M Alkaisi, "Enhancing the performance of solar cells with inverted nanopyramid structures fabricated by UV nanoimprint lithography", IEEE 43rd Photovoltaic Specialists Conference (PVSC-2016), Portland, OR, USA, June 5 - 10, 2016 (Poster presentation).

4. **Amalraj Peter Amalathas**, Maan M Alkaisi, "The Formation of Periodic Upright Nano-Pyramids Using UV Nanoimprint Lithography (UV-NIL)", 7th International Conference on Advanced Materials and Nanotechnology (AMN-7) , Nelson, New Zealand, Feb 8-12, 2015 (Poster Presentation).

Table of contents

List of figures

List of tables

List of acronyms

2D	Two-Dimensional
3D	Three-Dimensional
AFM	Atomic Force Microscope
ARC	Anti-Reflection Coating
BCPL	Block Copolymer Lithography
DC	Direct Current
DI	Deionized
EBL	Electron Beam Lithography
EQE	External Quantum Efficiency
FIB	Focused Ion Beam
HEL	Hot Embossing Lithography
INP	Inverted Nanopyramid
ITO	Indium Tin Oxide
LB-ADSA	Low Bond Axisymmetric Drop Shape Analysis
LIL	Laser Interference Lithography
NIL	Nanosphere Lithography
PCE	Power Conversion Efficiency
PVD	Physical Vapor Deposition

RF	Radio Frequency (RF)
RIE	Reactive Ion Etching
SAM	Self-Assembled monolayer
SEM	Scanning Electron Microscope
SFIL	Step and Flash Imprint Lithography
SSIL	Step and Stamp Imprint Lithography
TNIL	Thermal Nanoimprint Lithography
UNP	Upright Nanopyramid
UV-NIL	Ultraviolet Nanoimprint Lithography

Chapter 1 Introduction

1.1 Motivation

The current energy demand has depicted that energy requirement to sustain human life and activities has risen because of the increasing global population and emerging economic development. According to the US Energy Information Administration, it is expected that total world energy consumption increases by 48 percent from 2012 to 2040 [1]. Generating necessary energy to meet this growing demand has been of a major global concern. A number of energy sources are in use for global energy production. Fossil fuel is the primary energy source today that accounts for over 80 percent of the global energy consumption [2], but it is questionable to provide such enormous future demand because of its limited availability. Furthermore, the burning of fossil fuel releases greenhouse gasses into the earth's atmosphere which leads to global warming.

The current world energy system is unsustainable, unreliable, insufficient, not cost effective and environmentally unfriendly. To this end, energy production from renewable sources such as solar, wind, hydroelectric, tidal, bioenergy and geothermal are much desired. The renewable energy sources are free and abundantly available in the environment. Solar energy is one of the best alternatives to fossil fuel among other alternative energy sources because it has the potential to meet future demands at low cost with no detrimental effects to the environment. There are different technologies to harvest this solar energy, and typical examples include solar electric (photovoltaic), solar thermal and solar fuel technologies. Photovoltaic energy conversion, which converts light energy into electricity without any intermediate stage, is a promising technique for solar energy utilization. In the last ten years, the photovoltaic market has shown a very significant

growth of 49% on average in order to reach a cumulative installed capacity of over 135 GW in 2013 [3]. According to the International Energy Agency, it is expected that photovoltaic energy generation would contribute a 16% share in the global energy market by 2050 [3]. Currently, about 90% of the photovoltaic solar cell market is dominated by crystalline Si-based solar cells while only 10% only is represented by different technologies based on thin films of cadmium telluride (CdTe), amorphous silicon (a-Si:H), microcrystalline silicon (μc-Si:H) and copper indium gallium selenide (CIGS) [4].

In order to meet the requirements of the global energy demand using photovoltaics, further conversation efficiency improvements and reductions in production cost are necessary. The advanced nanophotonic light trapping approaches can contribute to both objectives simultaneously. Over the last few years, many light trapping strategies have been proposed to trap the light in order to enhance the light absorption within the active absorber layer, and thereby improving the power conversion efficiencies [5-12]. Moreover, enhancing the optical absorption also allows decreasing the active absorber layer thickness, which influences the production costs. In addition, the solar cells can be easily contaminated in real outdoor environments by dust particles, which interfere with incident light reaching the cell absorption layer and thus reducing the conversion efficiency. Therefore, the nanophotonic structures with a self-cleaning capability at the top surface of the solar cell are necessary to the sustainability and improved performance of the solar cells in dusty environments [13-17].

1.2 Light trapping in solar cells

Optical losses of solar cells may be categorized into reflection from the front surface, preventing light from entering the solar cell, and poor absorption due to the transmission losses. Reducing optical losses in the solar cells has always been a key challenge in improving the power conversion efficiency. Light trapping is needed to maximize the optical path length of sunlight in solar cells and reduce reflections in order to enhance the overall efficiency. Typically, a thicker active layer can improve the absorption of more sunlight whereas the optical thickness of the active layer is enhanced several times its physical thickness is kept unchanged by using light trapping structures in a solar cell.

In general, light trapping techniques have been utilized in the development of high performance and low-cost solar cells by enhancing light absorption without requiring thicker active layers. The most widely used light trapping techniques in the industry are the upright or inverted pyramid structure [18, 19] or random textures [20] for texturing crystalline silicon solar cells, which has a characteristic feature size of typically $3 - 10$ μm [21]. Such large-scale geometries are not suitable for the thin film solar cell where the active region itself is only a few microns or even few hundred nanometers thickness. In addition, micron scale features require deep etching and are known to introduce defects in the material [22].

Therefore, nanostructures are needed in order to achieve light trapping in thin film low cost solar cells. The use of nanoscale surface structures for improving the light absorption of the solar cells is a promising method compared with the traditional micro-sized surface texturing for crystalline silicon solar cells [23, 24]. This is because of the reduced etching depths required to form the nanoscale features and consequently decreases the level of damage to the substrates. Furthermore, reflections are reduced over

a wide range of wavelengths in sub-wavelength nanophotonic structures. It has also theoretically been illustrated that nanophotonic structures can achieve the optical path length enhancement factors beyond the Yablonovitch conventional limit [25]. There are a variety of structures that can be used for nanophotonic light trapping in solar cells. The most common methods for light harvesting can be classified as periodic grating structures [26-28], photonic crystal structures [29-33], nanowires [34-36], random scattering surfaces[37, 38], and plasmonic structures [39-41].

1.2.1 Periodic light trapping nanostructures

The introduced a periodic structure into a solar cell surface is capable of contributing to both measures of reflection reduction and optical path length enhancement. However, depending on the position (front or rear side of the surface), type and dimensions of the surface structure, not necessarily both effects can be exploited. Figure 1.1 shows the potential optical effects caused by textured surfaces. These exemplary cases of three ratios of wavelength λ to structure period Λ are illustrated for periodic features[42].

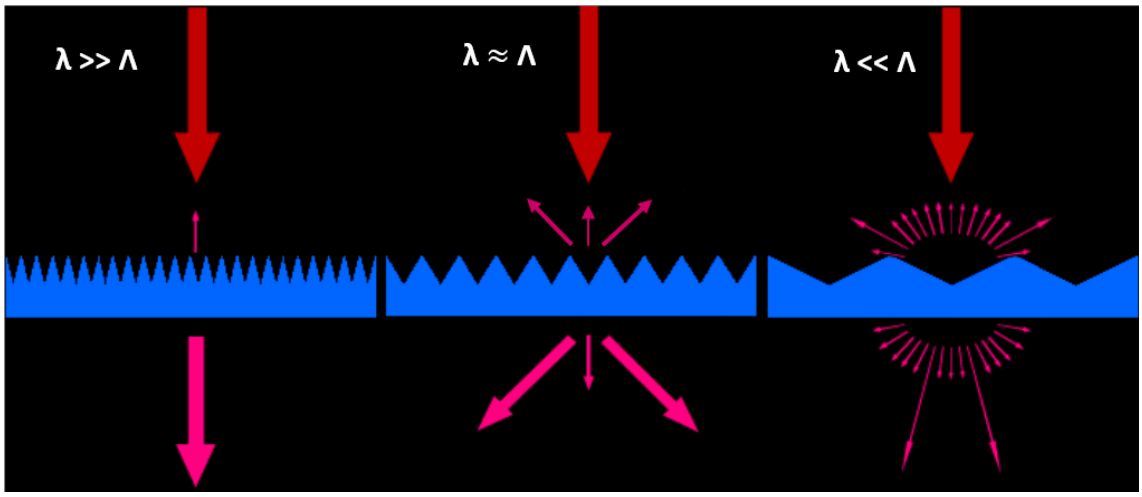

Figure 1.1: Schematic illustration of optical effects caused by periodically textured surfaces of varying special frequency for a given wavelength. λ is wavelength and Λ is the structure period [42].

For $\lambda << \Lambda$, a large number of diffraction orders can propagate through the structure. The shape of the surface pattern strongly influences the intensity distribution of these higher diffraction orders. For a very high ratio of Λ to λ, this effect leads to the geometric optical limit of refraction which can be described by Snell's law. The internal optical path length improvement in solar cells can be achieved due to these effects related to a change of propagation direction. Second effect is that multiple reflections can occur when treating the effects occurring in these large structures geometric optically. This effect additionally decreases the overall reflection at the front surface.

For the interaction of the structure sizes and wavelengths of similar dimensions ($\lambda \approx \Lambda$), interference effects leading to distinct diffraction orders influence the optical behavior. Because of these effects, the behavior of the patterned surface is strongly wavelength dependent in terms of transmission and reflection properties. Well defined structures can be utilized to achieve both reflection reduction as well as a strong optical path length enhancement.

Periodically textured surfaces with features the size of well below the incoming wavelengths can be demonstrated using effective medium theories[43]. This means that the structures are not resolved by the light and therefore act as a medium with an effective refractive index. As a consequence, very efficient and broadband antireflection effect can be obtained. These small features have influence on the amount of reflection and transmission but do not induce any light guidance since no change of light propagation direction occurs.

One, two or three dimensional (1D, 2D, or 3D) periodic nanostructures or gratings are a promising way of achieving light trapping in solar cells and hence enhancing their efficiencies. Figure 1.2 illustrates a schematic diagram of photonic nanostructures used in several ways to improve the solar cell performance [44].

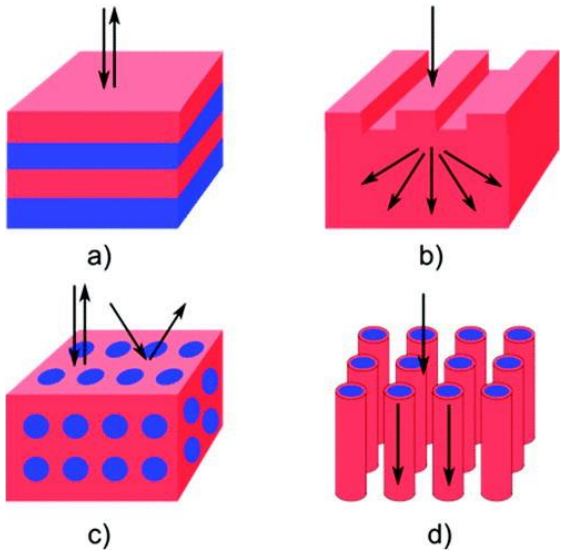

Figure 1.2: Schematic illustration of nanophotonic structures used for enhancing solar cell performance: (a) 1D (Bragg) stacks (b) 2D gratings, (c) Photonic crystal, and (d) Nanowires [44].

Optimized 1D dielectric gratings or Bragg stacks can be utilized as back reflectors that double the path length of light in the active volume of a solar cell. Single period or bi-periodic dielectric structures can be employed for minimizing the reflection from the irradiated surface of a solar cell or for trapping light inside the active volume of the cell [45]. Two-dimensional sub-wavelength gratings are even more promising than one-dimensional grating since the reflectivity does not depend on the polarization of the incident light [46]. In tandem solar cells, 3D periodic nanophotonic structures or photonic crystals can be employed as vastly efficient omnidirectional reflectors [33].

A variety of three-dimensional nanophotonic structures, such as nanocones [47-50], nanorods [51-53], nanopillars [54-56], nanowells [57-59], nanopyramids [60-63] and nanospheres [64, 65], have been extensively studied for enhancing the performance of the solar cells. Wang et al.[66] have demonstrated through numerical studies that by incorporating periodic nanocones structures on the front for antireflection coatings and on back for light trapping, the short circuit current density can be enhanced from 19.7 $mAcm^{-2}$ to 34.6 $mAcm^{-2}$ for a 2 μm thick crystalline Si solar cell. Battaglia et al.[32] have experimentally studied that the efficiency of the a-Si:H solar cells can be increased from 7.9% to 10.9% by depositing the solar cells on glass substrates patterned with a periodic array of nanocavities.

In another notable work, Mavrokefalos et al.[60] have shown that by incorporating inverted nanopyramid light trapping schemes for crystalline Si thin films, less than 10 μm thick crystalline Si films can achieve the light absorption comparable to that of planar crystalline Si films thicker than 300 μm. Sivasubramaniam et al.[61] have experimentally demonstrated that the efficiency of the crystalline Si solar cells can be enhanced by 67% with inverted nanopyramid texturing, compared to planar solar cells. Li et al.[62] have also studied the effect of the inverted nanopyramid structure on the performance of the ultrathin a-Si/c-Si solar cells, where inverted nanopyramid structure is introduced between the top and bottom cells. It has been reported that the short circuit current density can be improved by 48% and 35% due to the superior light harvesting capability for the top and bottom cells, respectively.

It has been shown that inverted nanopyramid structures could be a more suitable candidate for light trapping due to their gradient refractive index tapered profile. In addition, among all studied nanostructures, the inverted nanopyramid structures possess

the advantages of achieving the desired function in relatively low surface area and negligible surface damages, which reduces the electronic losses [60, 62, 67].

1.2.2 Plasmonic light trapping structures

Nanoplasmonics is the study of the interaction of light with small metal structures with dimensions of the order of the wavelength of light [68]. At these length scales the metal structures show unique optical properties and can strongly concentrate and confine light in regions smaller than the free space wavelength [69]. Nanoplasmonic structures can be constructed in three different configuration for light trapping structures as shown in Figure 1.3 [70].

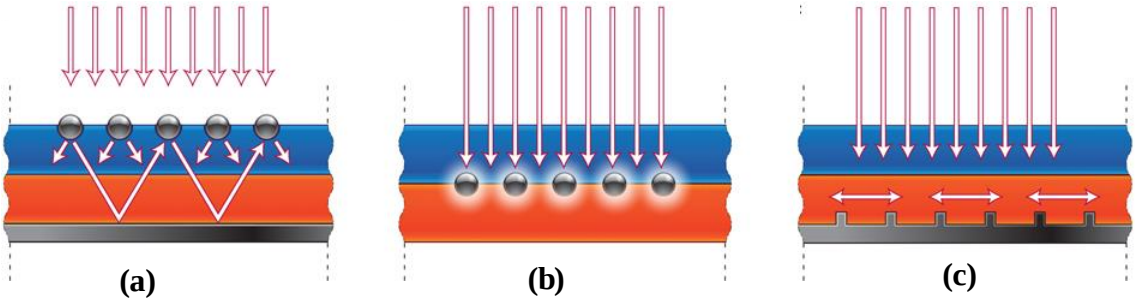

Figure 1.3: Schematic of three different nanoplasmonic light-trapping geometries for thin-film solar cells. (a) Metal nanoparticles placed on top of a solar cell, (b) metal nanoparticles embedded in the semiconductor, and (c) nanostructured metal films placed on the back surface of a solar cell [70].

In the first scheme, metallic nanoparticles can be used as subwavelength scattering elements to couple incident sunlight into solar cells. Properly engineered metallic nanoparticles can support localized surface plasmons, which strongly scatter light at certain wavelengths. If these particles are on top of the solar cells as shown in Figure 1.2(a), the scattered light contributes to light trapping by increasing the optical path length inside the cell. In the second scheme, discrete metal nanoparticles are employed to improve local absorption within the solar cells. This method utilizes highly concentrated near field of nanoparticles embedded within the semiconductor so as to enhance the absorption in the surrounding regions of the cell (see Figure 1.2(b)). In the third scheme,

nanostructured metal films placed on the back surface of a solar cell can couple propagating sunlight into surface plasmon polaritons (SPP) modes (see Figure 2.2(c)). These modes propagate along the metal and semiconductor interface, confining the light along the boundary. It is known that the total absorption within the cell can be increased if the absorption in the semiconductor is higher than that of the metal.

Eminian et al.[71] have demonstrated that the Ag/ZnO back reflector with random arrays of Ag nanoparticles could significantly improve the short circuit current in n-i-p hydrogenated amorphous Si (a-Si:H) solar cells compared to the cells without Ag nanoparticles due to the strong scattering of Ag nanoparticles. Tan et al.[72] have also shown that a back reflector with plasmonic Ag nanoparticles could provide better light trapping performance comparable to the state-of-the-art random textures in n-i-p a-Si:H solar cells. Ferry et al.[73] designed the periodic nanostructured Ag/ZnO plasmonic back reflector by nanoimprint lithography and showed that the nanopatterned n-i-p a-Si:H solar cell improves the red response of the cell, predominantly through a 26% enhancement in short circuit current density.

1.3 Nanoimprint lithography for light management schemes in solar cells

Nanostructures can be fabricated by a variety of methods, including electron beam lithography [74], Deep ultra-violet (DUV) lithography [75], laser interference lithography (LIL) [76], nanoimprint lithography (NIL) [77], nanosphere lithography (NSL) [78] and hole-mask colloidal lithography (HCL)[79]. However, NIL is one of the most promising low-cost methods for nanostructure patterning over a large area with high throughput, high fidelity, and high resolution manufacturing technology [80]. Table 1.1 summarizes the advantages and disadvantages of the most well- known available nanopatterning methods.

Table 1.1 Summary of lithography methods relevant for nanopatterning. (++ = very high, + = high, - = low, -- = very low).

Technique	**NIL**	**Photolithography (DUV)**	**LIL**	**EBL**	**HCL**
Resolution	++	+	+	++	+
Flexibility	-	--	+	+	++
Precision	++	++	-	++	--
Throughput	++	-	+	--	+
Complexity	+	++	-	+	+
Cost	-	-	-	++	-
PV Industrial applicability	++	+	-	--	+
	[81]	[75]	[10]	[82]	[79]

In general, NIL can be classified into two fundamental types; Hot Embossing Lithography (HEL) also known as Thermal Nanoimprint Lithography (TNIL), and UV-based Nanoimprint Lithography (UV-NIL) [83]. Currently, many different variations of lithographic techniques have been developed based on NIL, typical examples include step and flash imprint lithography (SFIL) [84], laser assisted NIL [85], microcontact printing [86], reverse imprint lithography [87], and step and stamp imprint lithography (SSIL) [88].

In the last decades, several authors [89-98] have demonstrated that NIL could be successfully utilized in solar cells to enhance the performance of the solar cells. Paetzold et al.[97] have reported on the development and implementation of a nanophotonic front electrode for perovskite solar cells via UV-NIL. It has also been shown that the

nanopatterned perovskite solar cells show a relative enhancement of 5% in short-circuit current density compared to the planar cell due to the reduction of parasitic reflection losses. Chen et al. have studied that by incorporating nanostructures into ITO layer using UV-NIL, the short-circuit current density of the organic solar cells can be increased from 7.07 $mAcm^{-2}$ to 10.76 $mAcm^{-2}$ due to the enhanced effective optical path of absorbed light resulting from the light trapping and scattering by the nanostructures.

Han et al.[99] have shown that transmittance of the glass substrate with imprinted moth-eye-like structures on one or both sides can be improved by 2% and 4%, respectively compare to the bare glass substrate. It has also been demonstrated that the use of the patterned glass substrate as a protective cover glass, the power conversion efficiency of the solar cell can be increased up to 2.5 % for normal incidence. Jiao et al.[100] have demonstrated that by imprinting of moth-eye-like structures on the front side of monocrystalline Si solar cell surface, the power conversion efficiency can be enhanced by 19% compared to the reference solar cell by coupling incident light into the absorber layer. This approach of surface texturing differs from other approaches such as texturing the active material or using metal nanostructures. This approach improves solar cell performance without introducing additional surface recombination and also provides excellent self-cleaning functionality.

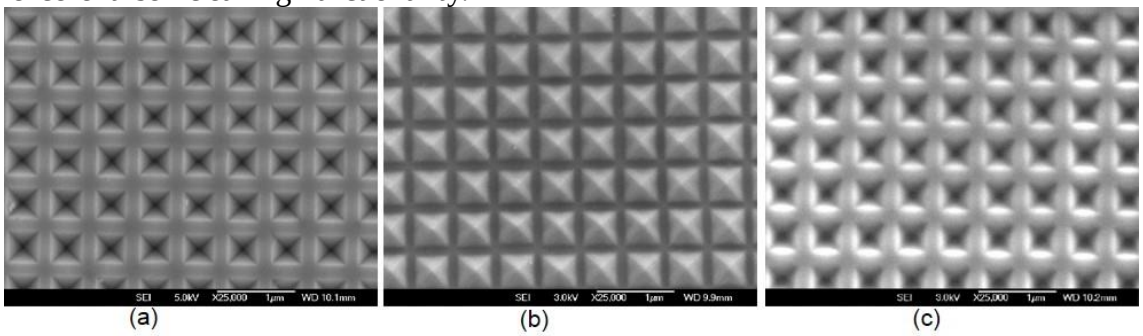

Figure 1.4: Top view of SEM image of (a) the inverted nanopyramid Si master mold, (b) the upright nanopyramid replica stamp (c) the periodic inverted nanopyramid imprinted onto the surface of the solar cells.

However, the periodic inverted and upright nanopyramid structures have not been demonstrated on solar cells by means of UV nanoimprint lithography. In this work, periodic upright and inverted nanopyramid structures as shown in Figure 1.4 were used as the light harvesting nanostructures to improve the performance of the solar cells using UV-NIL.

1.4 Objectives and outline of the thesis

The objective of this thesis is to develop the periodic upright and inverted nanopyramid structures as the light harvesting nanostructures to improve the performance of the solar cells using a combined LIL and UV nanoimprint lithography (UV-NIL). In addition, a superhydrophobic property is explored to add a self-cleaning functionality to the front encapsulation layer. This study investigates especially in the following points.

- Develop the periodic inverted nanopyramid structures on Si master mold by using laser interference lithography and subsequent pattern transfer by combined reactive ion etching and KOH wet etching.
- Develop the periodic upright nanopyramid resist-coated glass substrate as an anti-reflection coating and as a protective cover glass using UV-NIL and evaluate the potential of its light trapping and self-cleaning properties for monocrystalline Si solar cells and polycrystalline Si solar cells.
- Develop the periodic inverted nanopyramid structures on the front side of the monocrystalline Si solar cells and polycrystalline Si solar cells using UV-NIL to reduce the optical losses in solar cells and to also enhance the self-cleaning functionalities.
- Investigate the dependence of surface morphological, optical and electrical properties of the ITO thin films at different film thicknesses and sputtering RF

power and evaluate the optimum properties of ITO thin films for the photovoltaic applications.

- Develop the upright nanopyramid textured transparent electrodes to be applied for enhancing light harvesting efficiencies in organic, perovskite and thin film Si solar cells.

This thesis is organized as follows. The motivation of the thesis and research background are explained in **Chapter 1**. The objectives and outline of this research work are also presented in this Chapter.

Chapter 2 describes a brief overview of the experimental techniques utilized in the fabrication, processing as well as characterizations of structures employed in this work. The first section discusses the various deposition and processing techniques that were used for the fabrication and replication of nanopyramid structures and the solar cell fabrication including the ITO sputter deposition processes. The various characterization tools that were used either for solar cells or textured substrates analysis are described in the second section.

The fabrication process of periodic inverted nanopyramid structures is presented step by step in **Chapter 3**. First, the description of experimental setup details and basic theory of laser interference lithography (LIL) are introduced. Then, the sample preparation and LIL exposure process are explained, followed by subsequently pattern transfer process using reactive ion etching. As the last point of this chapter, formation of inverted nanopyramid structures on Si substrate using wet chemical etching is described.

In **Chapter 4**, the development of the ultraviolet nanoimprint lithography (UV-NIL) and imprint processes for the replication of upright nanopyramid and inverted

nanopyramid structures are presented. First, the sample preparation processes and the tools required for the NIL were developed within this work and described. Then, imprint processes for the replication of upright nanopyramid and inverted nanopyramid structures and patterns analysis are discussed in detail.

In Chapter 5, the effect of upright nanopyramid structured cover glass with light harvesting and self-cleaning functions on the device performance of monocrystalline Si solar cells and commercially made polycrystalline Si solar cells are presented. The upright nanopyramid structures were fabricated on the surface of the glass substrate through UV nanoimprint lithography using Si master mold with inverted nanopyramid structures. The surface wetting behavior and optical properties of the upright nanopyramid structured cover glass are presented. The electrical performance of the solar cells with upright nanopyramid structured cover glass were compared to bare cover glass and discussed in detail.

In Chapter 6, it is demonstrated that periodic inverted nanopyramid structures can enhance the power conversion efficiency of monocrystalline Si solar cell and commercially made polycrystalline Si solar cell by minimizing reflections, improving light trapping process in addition to its self-cleaning functionality. The fabrication process of periodic inverted nanopyramid structures on the front side of the monocrystalline Si solar cell and polycrystalline Si solar cell surfaces using a UV nanoimprint lithography are discussed. The reflectance, external quantum efficiency, current-voltage measurements and wettability of the monocrystalline Si and polycrystalline Si solar cells with and without the inverted nanopyramid structures are also investigated.

The effects of film thickness and sputtering RF power on the surface morphological, optical and electrical properties of Indium tin oxide (ITO) thin films were studied in

Chapter 7. The chapter also details the deposition of ITO films onto upright nanopyramid structured glass substrates. In addition, optimization of film thickness and sputtering RF power to produce high performance ITO (high transparency and low resistivity) suitable for solar cells applications are demonstrated.

Chapter 8 presents the general conclusions of this thesis as well as the suggestions for future research in this area. Perspectives for future developments of the light management schemes are suggested based on the research works in this thesis.

Chapter 2 Fabrication, processing and characterization techniques

In this thesis, a number of fabrication, processing, and characterization technologies were employed. This chapter describes a brief overview of the experimental techniques utilized in the fabrication, processing as well as characterizations. Section 2.1 discusses the various deposition and processing techniques that were used for fabrication and replication of nanopyramid structures, the solar cell fabrication, and for ITO deposition. The various characterization tools that were used for solar cells and textured substrates analysis are described in section 2.2.

2.1 Fabrication and processing techniques

The inverted nanopyramid structures with a width of about 450 nm, a height of about 310 nm and separation of about 125 nm were fabricated on Si substrates using laser interference lithography (LIL) and subsequent pattern transfer by combined reactive ion etching and KOH wet etching. The LIL was used for defining the periodic nanoscale patterns on photoresist over the large area of 15 × 15 mm^2, which is discussed in Chapter 3. Prior to LIL, the multi-layer stack sample was prepared using thermal oxidation, thermal evaporation of SiO2, and imaging layer spin coating techniques. The pattern transfer process was performed by reactive ion etching (RIE). The nanopyramid replication process conducted by UV-NIL and is explained in Chapter 4. For monocrystalline Si solar cell fabrication, spin coating of resist or spin on dopant, photolithography for metallization, furnaces for diffusion of doping elements and DC magnetron sputtering techniques for metal deposition were used. The ITO thin films were deposited by RF magnetron sputtering, and metal contact was deposited by e-beam evaporation for electrical contacts and measurements.

2.1.1 Magnetron sputtering

Sputter deposition method has been widely used technique for the deposition of metals, alloys, transparent conductive oxides, and dielectric thin films onto the substrates. This technique is a type of physical vapor deposition (PVD) techniques, which includes thermal evaporation, pulsed laser deposition, and e-beam evaporation. The sputtering process is the ejection of atoms from a solid target material due to the bombardment of the target by energetic particles generated in a glow discharge plasma. There are a number of ways to improve this process. The most common way to do this is the use of a magnetron source surrounding the target area, known as a magnetron sputtering. Magnetron sputtering is where the application of a magnetic field in a plasma causes traveling electrons to spiral along the direction of the magnetic field near the target instead of being attracted toward the substrate.

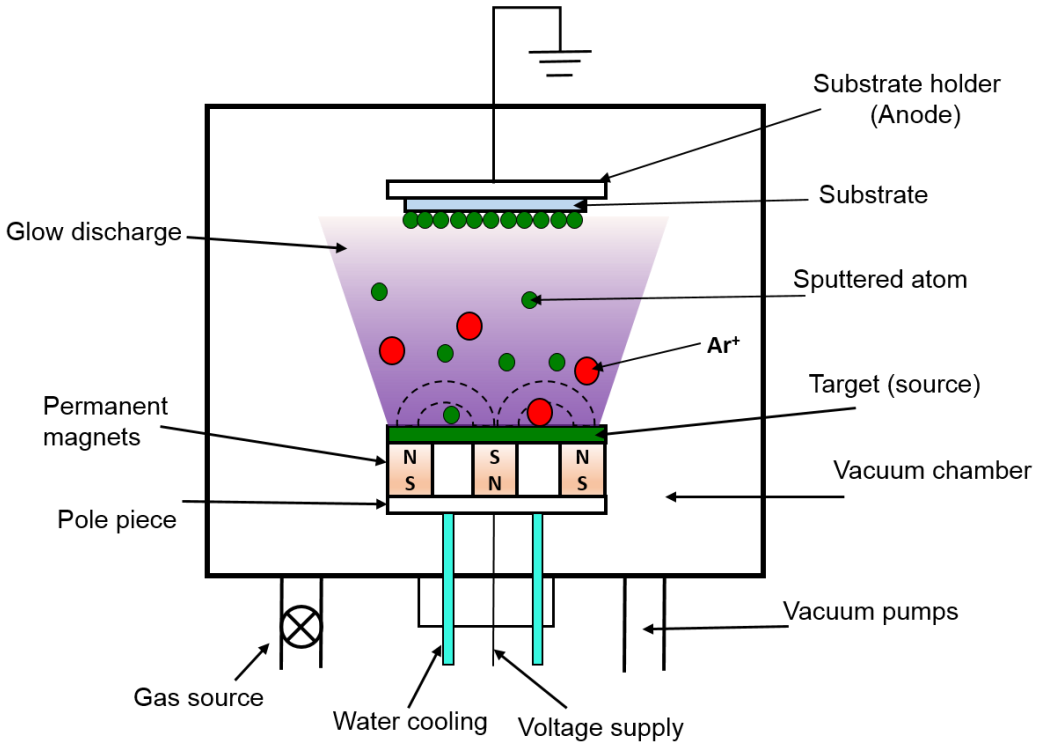

Figure 2.1: The schematic illustration of a magnetron sputtering system.

Figure 2.1 illustrates the schematic of the key components of the magnetron sputtering system. The basic sputtering process as follows. The inert gas such as Argon is introduced into a vacuum chamber at a vacuum pressure of 1 to 10 mTorr. An RF voltage is applied between the substrate and target which ionizes the Argon atoms and forms a plasma, consisting of Argon positive ions and electrons. The target is bombarded with the heavy ionized Argon atoms, ejecting atoms from the target which condenses on the relatively cooler substrate forming a layer of thin film on the substrate. The plasma is confined near the target surface due to the magnetic field, resulting in faster deposition rates at lower pressure and high-quality film.

In this study, an Edward Auto500 Magnetron Sputtering system as shown in Appendix A - Figure A-1, was used for depositing metallic, semiconducting and dielectric materials. This system is equipped with radio frequency (RF), direct current (DC) magnetron sources and an electron beam evaporation attachment. DC magnetron sputtering was mostly utilized for metal deposition and RF magnetron sourcs was commonly used for non-metal deposition such as metal oxides, semiconductors, ceramics, and dielectric materials.

In this work, DC magnetron sputtering was mainly used for depositing aluminum layer as a metal contact layer for solar cells. On the other hand, RF magnetron sputtering was used for depositing the ITO layer as a transparent conductive layer for solar cells base contact.

2.1.2 Thermal evaporation

Thermal evaporation is one of the most commonly used physical vapor deposition (PVD) techniques for thin film deposition. Figure 2.2 illustrates the schematic of the main components of the thermal evaporator system. In the thermal evaporation deposition

technique, the target that contains the deposition material is heated in a vacuum chamber until its surface atoms have the necessary energy to leave the surface. The energy is generated from a high electrical current passing through a metal plate or a filament. The vaporized material is then condensed in the form of a thin film on the substrate mounted over the evaporating material on the top side of the chamber.

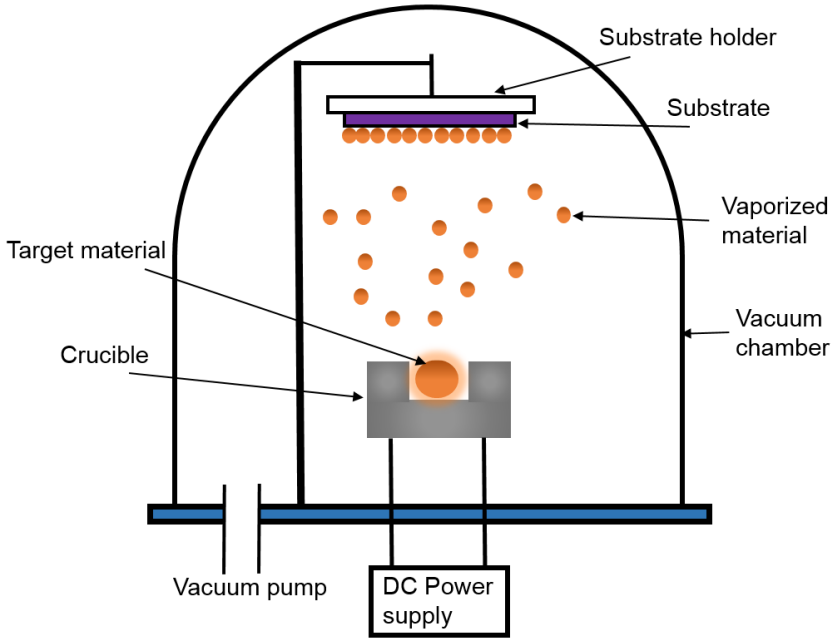

Figure 2.2: The schematic illustration of a thermal evaporator system.

Refractory metals like molybdenum (Mo), tungsten (W) or tantalum (Ta) are generally used in the form of wire, boat or crucible having different shapes and sizes as resistance based heating elements. The variables used to control the material evaporation are vacuum chamber pressure, source material purity and evaporation DC power. These parameters also determine the evaporation rate. In order to achieve a good quality material deposition, the pressure in the vacuum chamber is desired to be as low as possible so that the point where the mean free path is longer than the distance between the evaporation material and the substrate. The mean free path (l) is the average distance traveled by an atom or molecule before the collision with another moving particle in a vacuum chamber, which can be estimated by the following formula.

$$l = \frac{kT}{\sqrt{2}\pi d^2 P} \qquad (2.1)$$

Where k is the Boltzmann constant, T is the temperature in *Kelvin*, d is the particle size, and P is the vacuum pressure in *kPa*.

In this work, A Balzer 510A thermal evaporator as shown in Appendix A - Figure A-2 was employed for depositing silicon oxide film as a pattern transfer masking layer. This evaporator system allows multisource sequential evaporation, where two different materials can be deposited onto the substrate without breaking the vacuum. The thickness of the deposited film was monitored by Sigma SQM-160 crystal monitoring system positioned near the substrate.

2.1.3 Electron beam evaporation

Figure 2.3 shows the schematic illustration of a common electron beam evaporation system. Unlike thermal evaporation, in an electron beam deposition technique, the target material is placed in the crucible and bombarded by a flux of electron beam generated by a heated Tungsten filament under high vacuum. The produced electrons are focused as a beam and directed towards the target material in the crucible by several bending magnets. This electron beam generates a localized heating on the crucible system, where the target material is only heated above its melting point while the crucible is cooled to avoid cross contamination problems. The evaporated material is condensed on the substrate directly mounted over the substrate.

In the UC Nanofabrication lab, a 5KeV electron beam evaporator unit is embedded within the Edward Auto500 Magnetron Sputtering system. This system consists of a multiple source crucible unit, where up to four different materials can be deposited onto

the substrate without breaking the vacuum. In this work, electron beam evaporation was employed for the deposition of Ti and Au as a metal contact for the electrical measurements.

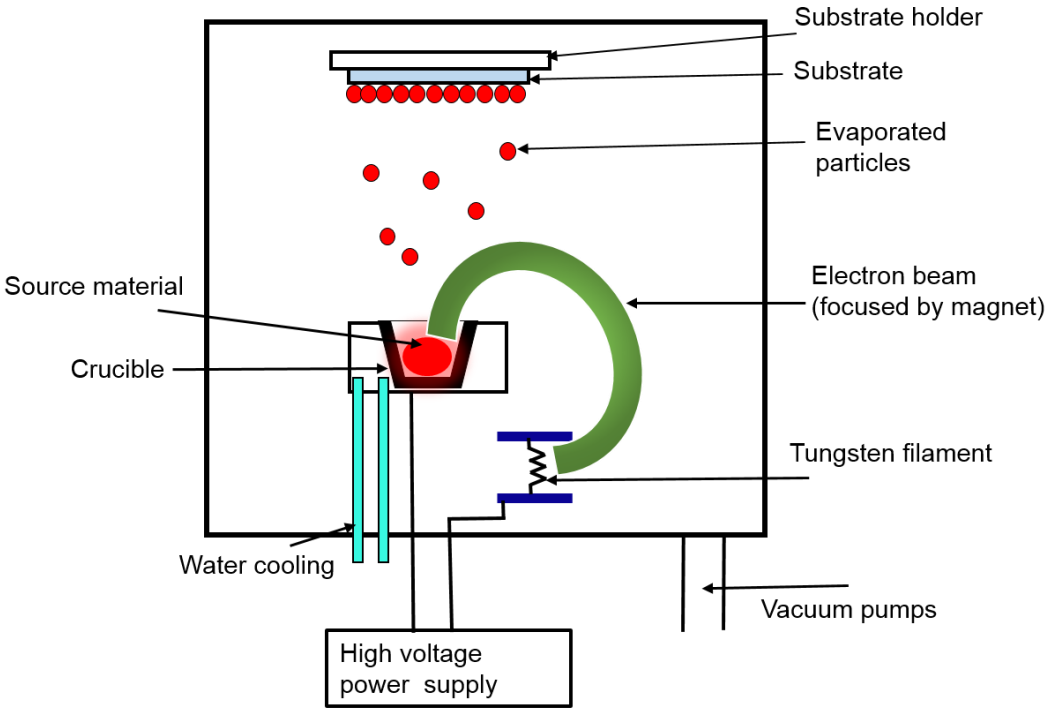

Figure 2.3: The schematic illustration of the electron beam evaporation process.

2.1.4 Reactive ion etching

Reactive ion etching (RIE) is a plasma etching process utilizing chemical reaction with process gases and physical damage by ion bombardment to remove the material. RIE is commonly used to transfer the developed pattern into the substrates as a high selectivity and anisotropic etching technology. Unlike the isotropic wet etching process, RIE is a unidirectional etching process due to the vertical path of reactive ions and induced biased electric field on the substrate.

Figure 2.4 shows the schematic view of the parallel plate electrode RIE system. In the RIE system, a plasma is generated in the gas mixture by a radio frequency (RF) electric field source operating at 13.56MHz that breaks the gas molecules into ionized atoms and electrons. In the vacuum chamber, these free electrons are electrically accelerated up and down by the alternative electric field and hit the chamber walls or the electrically insulated wafer platter. When electrons strike the insulated wafer platter, the negative charge builds up, resulting in a large negative bias voltage on the wafer platter, leaving the plasma positively charged. The ions in the plasma drift towards the samples due to the potential difference between the negatively charged wafer platter and positively charged ions. These ions react chemically with the surface of the sample and at the same time, physically etch due to the high kinetic energy of the ions. A number of parameters such as process gas types, background and process pressure, temperature, RF power and the gas flow rate can be adjusted to obtain the anisotropic etching profiles.

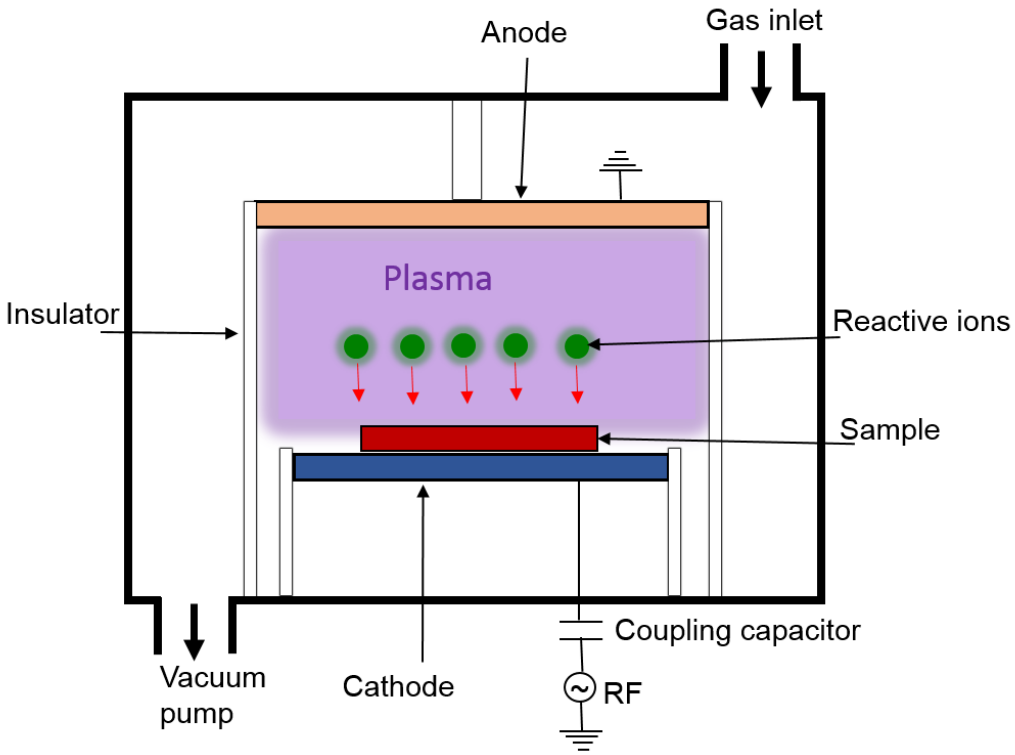

Figure 2.4: The schematic view of the parallel plate RIE system.

In this study, Oxford Plasma 80plus RIE System as shown in Appendix A - Figure A-5 was employed for dry etch the patterned nanoholes structures into the Si substrate for the fabrication of the master mold inverted nanopyramid structures. The optimized RIE process parameters for the pattern transfer process which consist of selecting the pressure, the mixture of gasses, temperature, RF power, gas flow rate and etching time are discussed in details in Chapter 3, section 3.5.

2.1.5 Photolithography

Photolithography is the process of transferring geometric patterns from a photomask onto the thin layer of photosensitive material called photoresist covering the surface of the substrate using a UV light source. The system consists of a photomask, a UV light source, and photoresist coated substrate or the layer to be patterned. The main steps involved in the photolithographic process are mask making, photoresist application, mask alignment, exposure, and development.

The mask comprises of patterned shapes of Chrome metal on soda lime glass plate corresponding to the patterns to be transferred to the resist layer. Chrome on glass masks for photolithography was designed utilizing L-Edit computer aided program and made by a mask writer with a diode laser of 405 nm wavelength. A µPG 101 Laser Mask Writer system as shown in Appendix A - Figure A-3 was employed to make the masks for the oxide window opening and top contact patterning of solar cells in this work.

There are two types of photoresist for transferring the patterns, such as negative and positive photoresist. When exposing a photoresist film with the UV light, the exposed positive photoresist area becomes more soluble, and exposed negative photoresist area becomes less soluble in a resist developer. In this work, the Headway PWM32-PS-R790

spin coater as shown in in Appendix A - Figure A-7 was employed to coat the AZ1518 positive photoresist onto the silicon substrates for transferring the designed features onto

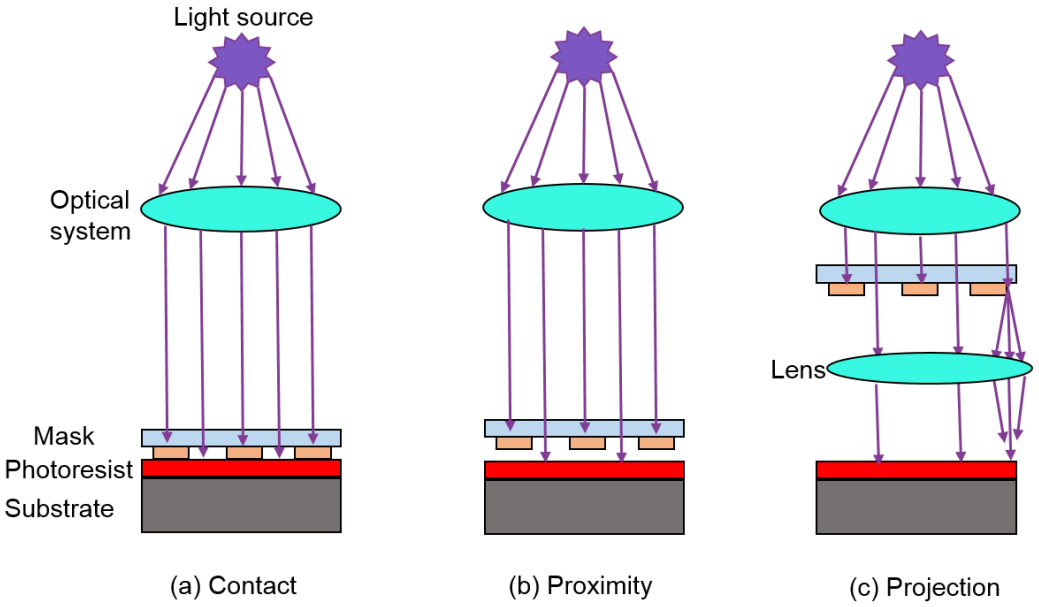

Figure 2.5: The schematic diagram of optical lithographic exposure methods (a) contact printing, (b) proximity printing and (c) projection printing.

the sample.

One of the most key steps in the photolithography process is mask alignment and exposure methods. There are three different primary exposure methods: contact, proximity, and projection printing. The schematic illustration of these methods is shown in Figure 2.5. In contact printing, the mask is brought into physical contact with the resist coated substrate during the exposure. The high resolution is possible in contact printing, but this method generates defects in the mask and causes defects in pattern features. In proximity printing, the mask and the resist coated substrate are brought very close to one another separated by a small gap during the exposure. The gap in the range of 10 to 50 µm is maintained between the mask and substrate during the exposure. This gap minimizes the mask defects. In projection printing, a projection system is placed between the mask and resist coated substrate, which refocuses the diffracted light into the resist

coated substrate. This printing technique avoids the mask defects entirely, but the resolution of the projection is limited by the diffraction effect.

A Karl Suss MA-6 mask aligner system as shown in Appendix A - Figure A-4 was employed for all the photolithographic exposures. It is capable of performing several contact and proximity printing modes, including soft, low vacuum, high vacuum, proximity, and hard contact. The Karl Suss MA6 system is equipped with a 350W UV lamp source which produces exposure light in the wavelength range of 350 nm - 450 nm. This system was mainly used in vacuum contact modes to transfer the pattern onto the AZ1518 resist coated substrate for the oxide window opening and top contact patterning of solar cell.

2.1.6 Diffusion and Oxidation techniques

The schematic diagram of a quartz tube furnace is shown in Figure 2.6. Diffusion, thermal oxidation, and annealing process were performed in this system. The system consists of three cylindrical fused quartz tubes, resistance heating elements, a temperature controller system, and a source cabinet. The NiCr wire resistance heating elements are spaced along the furnace tube length to provide three heating zones. Distribution of process gasses is maintained at the source cabinet.

The quartz tube furnace as shown in Appendix A - Figure A-8 was used in this work for emitter diffusion, thermal oxidation, and annealing process. This furnace has three separate tubes. The emitter diffusion process is performed in various ways. In this work, a phosphorous spin-on-dopant coating was applied to the Si wafer surface. The wafers were then put in the furnace to diffuse a small amount of phosphorous atoms into the silicon surface. The diffusion process parameters are described in Chapter 5, section 5.2.2. The silicon can be oxidized into thermal silicon oxide layer under the high temperature

of about 900°C to 1200°C. Thermal oxidation process includes the wet oxidation and dry oxidation. In this work, the thermal oxide layer was grown on the Si substrate for pattern transfer process and also defining individual cells. The thermal oxidation process parameters are discussed in Chapter 3, section 3.3.2.

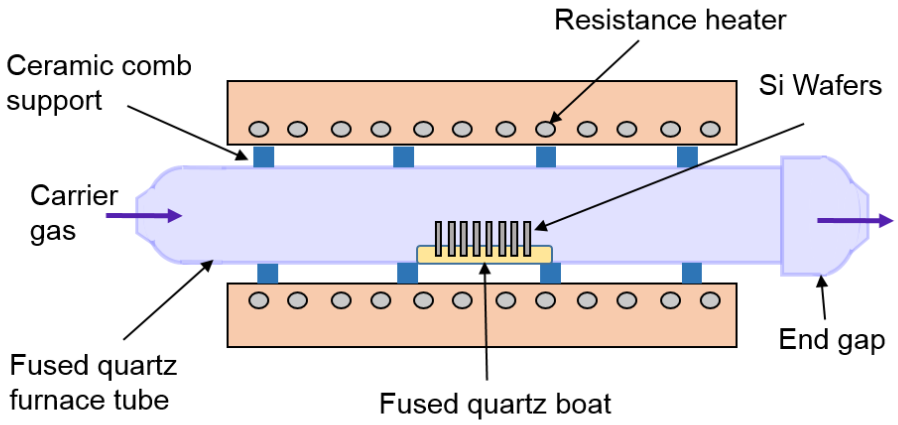

Figure 2.6: The schematic diagram of a resistance heated fused quartz tube furnace.

2.2 Characterization techniques

In this work, all fabricated samples were characterized using a variety of characterization techniques. The scanning electron microscope (SEM) and atomic force microscope (AFM) were utilized to investigate the morphology, surface roughness and dimensional measurement of features of the fabricated nanostructures. A UV-visible spectroscopy was used to evaluate the optical properties of the samples. The current-voltage and external quantum efficiency (EQE) measurements were performed for evaluating the performance of the fabricated solar cells. The Hall Effect measurements were employed for measuring the electrical properties of the ITO thin films. Contact angle measurements were performed for evaluating the self-cleaning properties and the anti-adhesion properties.

2.2.1 Scanning electron microscopy

The scanning electron microscope (SEM) is a type of electron microscope that uses a beam of electrons instead of light to examine the object on a very fine scale. The SEM has many advantages over the optical microscope. The SEM has a large depth of field, which allows the focusing on the large area of the specimen. The SEM also has a much high resolution for the imaging of closely spaced specimens. The main components of the SEM are illustrated schematically in Figure 2.7.

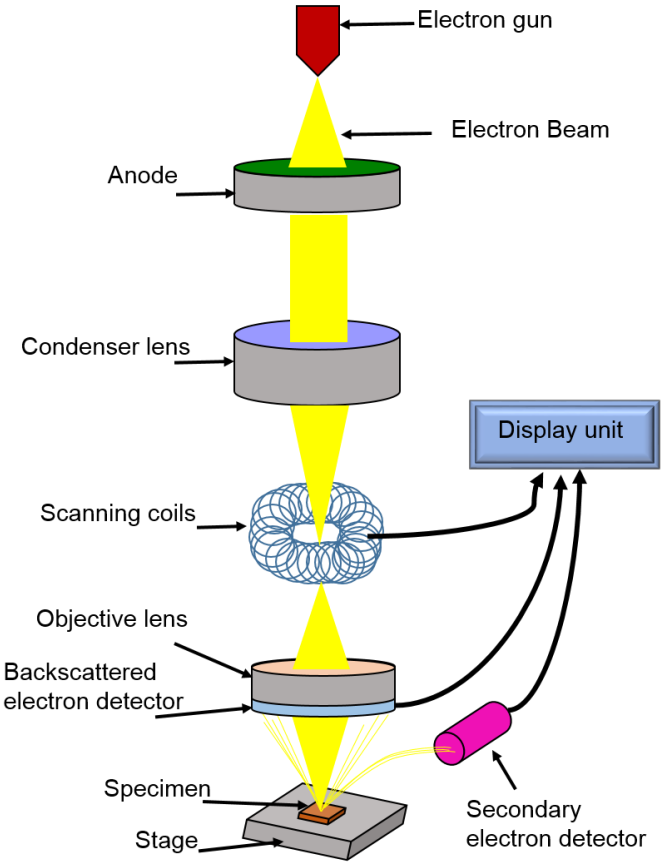

Figure 2.7: The schematic diagram of a scanning electron microscope.

The SEM works by using a beam of electrons, which is generated in a high vacuum by a suitable electron source, typically a tungsten filament or a field emission gun. The

electron beam is accelerated toward the specimen using a positive electrical potential. This accelerated beam is confined and focused into a thin beam of elecrons using a system of apertures and electromagnetic lenses, and then the beam scans across the surface of the specimen by scanning coils. As a result of the interaction of the electron beam and the atoms at the specimen surface, a number of signals are generated. These signals are then detected by suitable detectors. The examination of the specimens with the SEM can give important information about the sample, including topography, morphology, composition, and crystallographic information.

The secondary electrons emitted from the sample are the main source of information for SEM imaging. The secondary electrons can be released just from the surface of the sample due to the main electrons bombardment. The released secondary electrons are detected by a scintillator that generates flashes of light from the electron. The light signal is then detected and amplified by a photomultiplier tube. The resulting signal is converted to an image by an amplifier to project the image of the specimen on a monitor.

In this work, a Raith-150 electron beam lithography (EBL) system as shown in Appendix A - Figure A-13 and the JEOL JSM 7000F field emission SEM as shown in Appendix A - Figure A-17 were employed for SEM measurements.

2.2.2 Atomic force microscopy

The atomic force microscope (AFM) is a type of high resolution scanning probe microscopes. It uses the force existing between a sharp probe or tip and the specimen surface to build an image of the object. Different models of the AFM provides images of the specimens with atomic resolution in almost any environment including an aqueous solution. In AFM, images are obtained by feeling with the probe with the help of piezoelectric device rather than looking at specimens optically or electronically. Figure

2.8 shows the schematic illustration of the AFM detection using the laser beam deflection method.

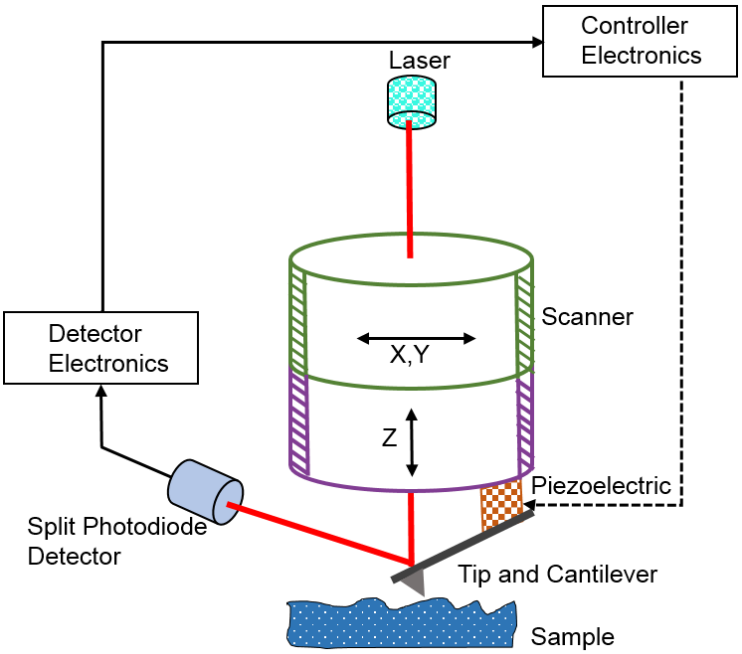

Figure 2.8: The schematic representation of an atomic force microscope detection using the laser beam deflection method.

A nanometer sharp AFM tip is attached at the free end of a flexible cantilever that is utilized as a transductor of the interaction between the specimen and the tip. The movement of the cantilever is monitored by the reflection of a laser beam at the backside of the cantilever into a photodiode detector. The scanner is then moved up and down in the vertical Z direction to maintain a constant force between the tip and the surface of the specimen. For imaging, the tip is scanned horizontally over the specimen. The cantilever deflection is measured at each position, from which the topographic map of the surface features can be constructed.

There are three primary imaging modes of operation in AFM: contact mode, non-contact mode, and tapping mode. In contact mode, the probe is brought into mechanical contact with the specimen surface during scanning. This mode can result in the specimen

damage due to the forces generated on the specimen surface by the probe. In non-contact mode, the probe of the cantilever does not contact the specimen surface. The cantilever is oscillated at near its resonance frequency and above the surface of the specimen such that it is no longer in the repulsive regime but in the attractive Van der Waals regime. The non-contact AFM imaging is quite difficult in ambient conditions when moisture is present on a specimen. Damage to a specimen can be minimized by a method called tapping mode AFM. In this mode, the cantilever is oscillated at its resonant frequency, and the probe makes intermittent contact with the specimen surface during the scanning. The tapping mode AFM allows topographic and internal structural information of the specimens to be collected with high resolution.

In this study, the Digital Instruments (Veeco Instruments Inc.) Dimension 3100 AFM system as shown in Appendix A - Figure A-11 was used for the AFM measurements in tapping mode. The processing and the analysis of the AFM images were performed with NanoScope Analysis software.

2.2.3 Contact angle measurement

Contact angle measurements are often utilized to evaluate the surface wetting properties. One of the most popular methods for measuring the contact angle is the sessile drop method, which involves placing a liquid drop on a solid surface and determining the angle between the solid surface and the tangent at the drop boundary. If the drop stops spreading sometime after deposition, the equilibrium contact angle can be easily determined through contact angle goniometry principles.

Figure 2.9 shows a sessile drop of probing liquid in contact with the solid surface. The equilibrium contact angle is given by Young's equation.

$$\cos\theta_C = \frac{\gamma_{SV} - \gamma_{SL}}{\gamma_{LV}} \qquad (2.2)$$

In this equation, θ_C is the equilibrium contact angle, and γ_{SL}, γ_{SV}, *and* γ_{LV} *are* solid-liquid, solid-vapor and liquid-vapor interfacial tensions, respectively. If the surface energy of the solid surface is high, the liquid will wet the solid surface, resulting in lower contact angle. Conversely, if the surface has a low surface energy, it will undergo poor wetting and anti-adhesiveness of the liquid drop, resulting in larger contact angle.

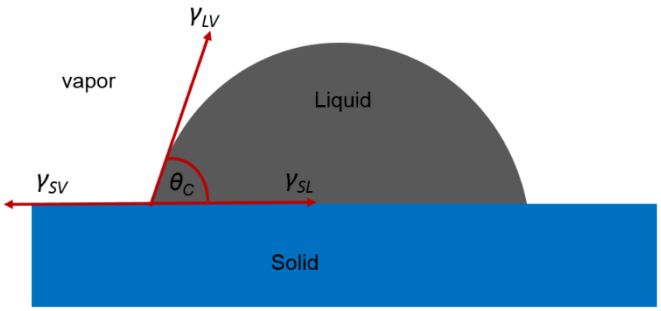

Figure 2.9: The schematic illustration of contact angle formed by sessile liquid drop on a solid surface.

In this work, the contact angle goniometer with Edmund Scientific Camera as shown in Appendix A - Figure A-20 from Department of Chemistry at UC was employed for measuring surface wettability. A 1.0 µl drop of deionized water was dispensed on the top surface of the substrate, and the image was manually captured by the system. The contact angle of the droplet image was calculated by using a low bond axisymmetric drop shape analysis (LB-ADSA) plugin in ImageJ software.

2.2.4 Current-voltage characterization

The electrical performance of a solar cell, which is determined from the current density-voltage (J-V) measurements of the illuminated cell, is typically measured under air mass 1.5 (AM1.5) simulated irradiation at a given intensity of 100 $mWcm^{-2}$ and temperature of 25 ^{o}C. Figure 2.10 shows a typical J-V curve of an illuminated solar cell. From the J-V curve, the short-circuit current density (J_{SC}), the open-circuit voltage (V_{OC}), and the fill factor (FF) are obtained as illustrated in Figure 2.10.

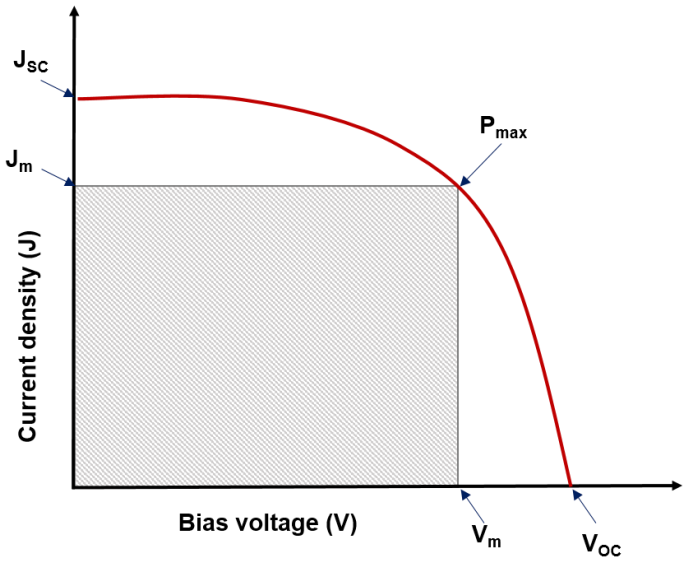

Figure 2.10: Typical current density– voltage (J-V) characteristics of a solar cell under illumination.

The open-circuit voltage (V_{OC}) is the maximum voltage available from a solar cell, and this occurs with no current flowing through the external circuit. The short-circuit current density (J_{SC}) is current density flowing through the solar cell at which no voltage is applied across the solar cell. The fill factor (FF) is the ratio of the maximum power that can be generated from a solar cell to the product of the short-circuit current density and the open circuit voltage and describes the 'squareness' of the J-V curve.

$$FF = \frac{J_m V_m}{J_{SC} V_{OC}} \qquad (2.3)$$

where V_m and J_m are the voltage and current at the maximum power output (P_{max}) point, respectively. The power conversion efficiency (η), which is defined as the ratio of the maximum power output to the power input to the solar cell.

$$\eta = \frac{J_{SC} V_{OC} FF}{P_{input}} \qquad (2.4)$$

where P_{input} is the input power of 100 mWcm^{-2} of the AM1.5 spectrum.

In this work, the current-voltage measurement setup as shown in Appendix A - Figure A-15 was employed to measure the current density–voltage characteristics of the solar cells. This experimental setup consisted of a computer controlled Keithley 2400 source measure unit and a solar simulator (ABET Sun3000) with AM 1.5G filter. The light intensity was set at 100 mWcm^{-2} with a spectrum and all the measurements were done at room temperature.

2.2.5 External quantum efficiency measurement

The external quantum efficiency (EQE) of a solar cell is defined as the ratio of the number of electrons in the external circuit produced by an incident photon at a given wavelength. The value of EQE is routinely measured to evaluate the performance of a solar cell by using monochromators. The EQE of a solar cell at a particular wavelength is given by the following equation.

$$EQE\ (\lambda) = \frac{J_{SC}}{P_{in}(\lambda)} \frac{hc}{e\lambda} \qquad (2.5)$$

where $P_{in}(\lambda)$ is the total incident power per unit area at an incident wavelength of λ. The intensity of the monochromatic light, $P_{in}(\lambda)$, is normally monitored by a the calibrated silicon photodiode. The intensity of the monochromatic light can be written as follows:

$$P_{in}(\lambda) = \frac{J_{SC}^{Si}(\lambda)}{SR_{Si}(\lambda)} \qquad (2.6)$$

where $J_{SC}^{Si}(\lambda) and\ SR_{Si}(\lambda)$ are the short-circuit current density of the silicon diode and its spectral response. The EQE of a solar cell is also given by the following equation.

$$EQE(\lambda) = EQE_{Si}(\lambda)\frac{J_{SC}}{J_{SC}^{Si}} \qquad (2.7)$$

where $EQE_{Si}(\lambda)$ is the EQE of the calibrated silicon photodiode.

In this work, a homebuilt typical EQE setup as shown in Appendix A - Figure A-19 at the Victoria University of Wellington was used to determine the EQE values of the solar cells. This EQE setup consisted of tungsten –halogen lamp in combination with a monochromator (CS130 1/8m). The photocurrent density of the solar cell, $J_{sc}(\lambda)$, and the photocurrent density of calibrated silicon photodiode density, $J_{sc}^{Si}(\lambda)$, were measured at a particular position and room temperature in the wavelength range of 400 nm - 900 nm. The EQE values were calculated by using equation (2.7) with the known spectral response of the photodiode and measured photocurrent density of the photodiode and the solar cell as a function of wavelength. All the EQE measurements presented in this study were carried out at zero bias voltage.

2.2.6 Reflectance-Transmittance measurements

The spectrophotometer has been extensively used for the evaluation of optical properties of thin films and textured substrates. This technique allows the measurement of reflectance and transmittance of a specimen as a function of incident light wavelength. In a typical spectrophotometer, a source of light hits on diffraction gratings, which are able to select a specific wavelength of light. The selected beam of light passes through the series of mirrors and is directed towards the specimen. The light transmitted or reflected by the specimen is then captured by the detector. Data from the detector is compared wavelength by wavelength to reference spectra. The measured spectra are thus obtained in percentage.

In this work, the Cary Spectrophotometer 619 as shown in Appendix A - Figure A-18 at Department of Physics, UC was mainly used to evaluate the optical properties of the ITO thin films. More details of the optical properties of the ITO films obtained from the transmittance measurements are described in Chapter 7, section 7.3.3. One major limitation of the Cary Spectrophotometer 619 used in this work is its inability to measure the diffused components of reflected and transmitted light.

However, an in-house built spectrophotometer setup equipped with an integrating sphere at Callaghan Innovation was employed for measuring the total and diffused components of transmitted and reflected light in this work. Its main component is the integrating sphere which makes it possible to measure the total and diffused components of reflected and transmitted light. The diffused components of reflected and transmitted lights are especially significant for light trapping textured substrates.

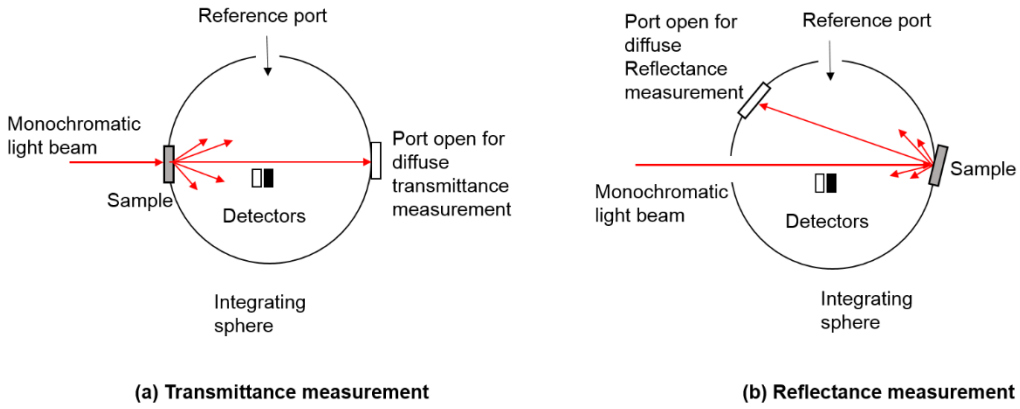

Figure 2.11: schematic diagram of total integrating sphere configuration and position of the sample for (a) the transmittance and (b) reflection measurements.

Figure 2.11 illustrates the sketch of the total integrating sphere configuration and position of the sample for the reflection and transmittance measurements. The integrating sphere has a diameter of 80 mm with the internal surfaces coated with a highly reflective material. For the transmittance measurements, the monochromatic light beam enters through the specimen, which is perpendicular to the optical axis. The total transmittance can be measured due to the multiple internal reflections. In order to measure the diffused transmittance, the cap is removed at the reflectance port and the specularly transmitted light can leave the sphere through the hole. The haze of transmitted light can be calculated with these measurements. For the total reflectance measurements, the light beam enters the integrating sphere through a port and hits the specimen at the reflection port with an angle of 6° incidence so that specularly reflected light is away from the entrance port.

The total and diffuse transmittance of upright nanopyramid patterned glass and the total reflectance of the monocrystalline and polycrystalline Si solar cells with and without the inverted nanopyramid structures were obtained over the wavelength range of 300–1200 nm in this study.

Chapter 3 Fabrication of inverted nanopyramid structures

3.1 Introduction

Nanostructure applications have attracted increasing interest in many fields ranging from nanoscale electronics to bionanotechnologies in last few decades [101-103]. Nanostructures can be fabricated by various techniques including electron beam lithography [46], focused ion beam lithography (FIB) [104], laser interference lithography (LIL) [26, 105], nanoimprint lithography (NIL) [106, 107], nanosphere lithography (NSL) [108] and block copolymer lithography (BCPL) [109].The electron beam lithography and focused ion beam lithography are commonly used in forming nanometer scale patterns. However, these technologies have a slow fabrication speed, and a high cost of equipment, which limits their applications in large-area structure fabrication [110]. In contrast, LIL is a maskless, high-throughput, and low cost for the fabrication of large area surface patterns in a short period time with tunable periodic structures [111-113].

LIL is a simple method used to produce periodic and quasi-periodic structures with nanoscale features over the large area. The principle is based on the interference between two coherent laser beams that form a standing wave for the grating pattern which can be recorded on a photosensitive layer. This technique allows to create periodic arrays of line, dots, and holes as well as other asymmetric 2D periodic structures with different feature sizes, pattern shapes and periods. The nanopatterning structures by LIL have been demonstrated for numerous applications areas, including nanofluidics for biological separations[114], nanomagnetics for high density data storage[115], templates for nanoimprint lithography[116] and self-assembly[117], optical applications such as solar

cells[10, 61, 73], sensors[118] and microlens arrays[119] for enhanced optical interactions.

In this research work, the inverted nanopyramid structures were fabricated on Si substrate by LIL and subsequent pattern transfer by combined reactive ion etching and KOH wet etching. The fabricated inverted nanopyramid structures on Si Substrate were used as a master mold in the replication process of ultraviolet nanoimprint lithography (UV-NIL). The replication process of inverted nanopyramid structures will be discussed in Chapter 4.

In this chapter, the fabrication process of periodic inverted nanopyramid structures is discussed step by step. First, the description of experimental setup details and basic theory of LIL are introduced in section 3.2; the design and preparation of the multilayer stack substrates for LIL are explained in section 3.3; the aspects of the single and double LIL exposure process are discussed in section 3.4; followed by hole patterns transfer from the soft resist into thermal SiO_2 hard mask layer using reactive ion etching and formation of inverted nanopyramid structures on Si substrate using wet chemical etching are discussed in section 3.5; finally the chapter summary is concluded in section 3.6.

3.2 Lloyd's Mirror Interference Lithography

There are various types of interference lithography methods such as Mach-Zehnder Interferometer [120], Scanning Beam Interference Lithography [121] and Lloyd's Mirror Interference Lithography[122], used for different applications. In this work, Lloyd's mirror interference lithography was used to obtain the periodic patterns on photoresist over the large area. The major advantage of this method is that the period of the pattern can be controlled more easily by rotating the stage comparing with other two beam interference methods.

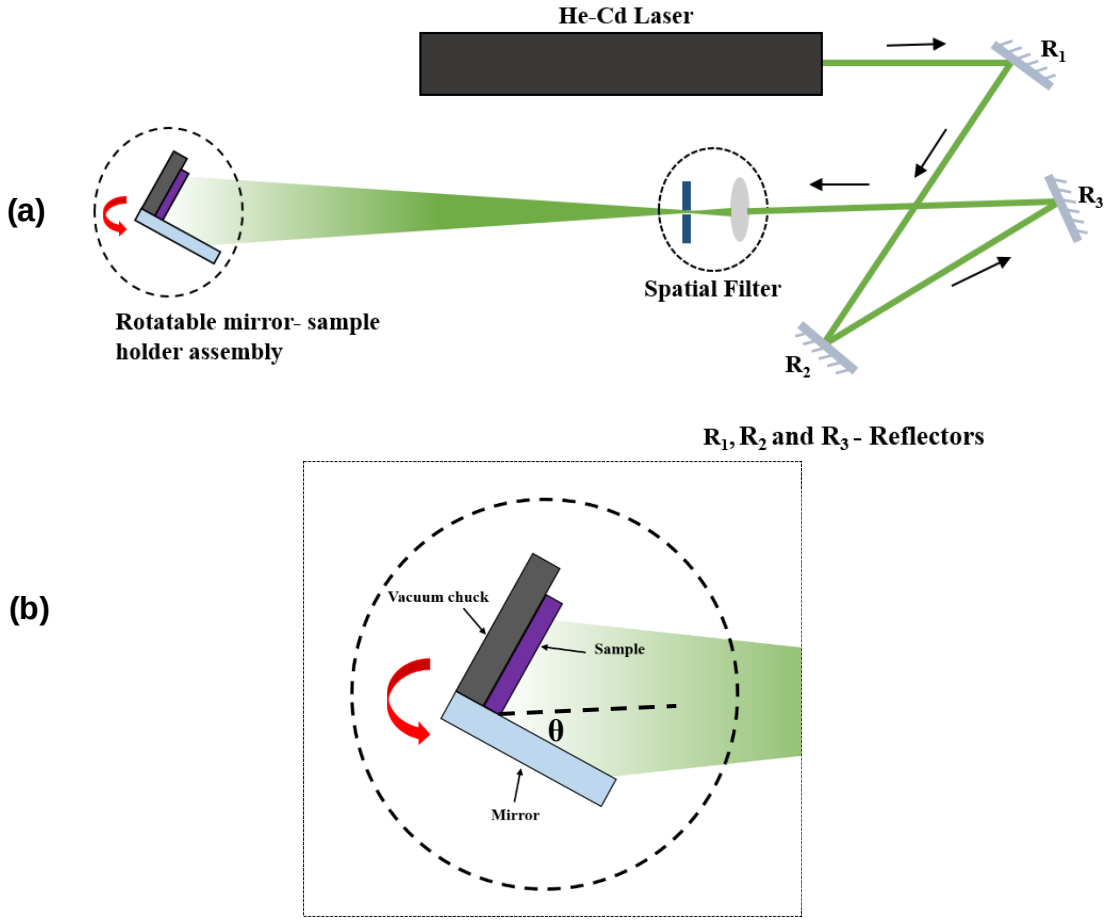

Figure 3.1: The schematic diagram of optical setup of Lloyd's mirror interferometer (a), with detail of the rotation stage (b).

A schematic diagram of Lloyd's mirror interferometer optical setup is shown in Figure 3.1(a). In this work, a 50 mW HeCd laser with a coherence length 30cm at 325 nm was used as a light source. A commercial spatial filter consists of a UV objective lens with a focal length of 5.77 mm and a 5μm diameter pinhole, which removes the high frequency noise from the beam to achieve a clean Gaussian profile. The Lloyd's mirror consists of a sample holder and an aluminum mirror, both placed perpendicular to each other to the rotation stage, as shown in Figure 3.1(b). A UV-enhanced aluminum coated mirror was used due to its enhanced reflectance in the UV region over a broad range of angles compared to other mirrors. The complete optical setup was built on the actively damped table in order to prevent vibrations, which could affect the interference pattern. The center of the substrate and mirror assembly was located on the optical axis.

The laser beam is expanded and spatially filtered through a pinhole to create a coherent beam at Lloyd's mirror interferometer. A coherent beam illuminates both the mirror and the substrate. There are two parts of the expanded light, which strike on the substrate. The part of the expanded light which is directly illuminating the substrate and interferes with the part of the expanded light that is reflected from the mirror surface. This interference gives a line pattern with a periodicity given by Equation 3.1. The two dimensional arrays such as dots, holes and variations on them can be recorded by double exposure with a sample rotated by 90° after the first exposure. The period of the pattern depends on the wavelength of the light source and the incident angle between the two beams. The horizontal standing wave interference periodicity, p, of the fringe pattern of the two interfering beams, can be described by the following equation [123].

$$p = \frac{\lambda}{2 \sin \theta} \qquad (3.1)$$

Where λ is the wavelength of the laser, and θ is the half angle between the incidence beams. The period of the pattern can easily be controlled by changing the angle θ which is equivalent to the rotation stage. The greatest advantage of Lloyd's mirror is the ease of period control. However, the UV-enhanced aluminum coated mirror's quality (related to flatness and perfections) is a key factor that influences the quality of patterns.

The main reason for any undesired pattern is the possible presence of second vertical standing wave interference. In addition to the primary standing wave formed parallel to the sample, there is a second standing wave in the vertical direction that can form perpendicular to the sample, caused by surface reflection as shown in Figure 3.2. This undesired standing wave is especially for highly reflecting substrates such as metals or silicon.

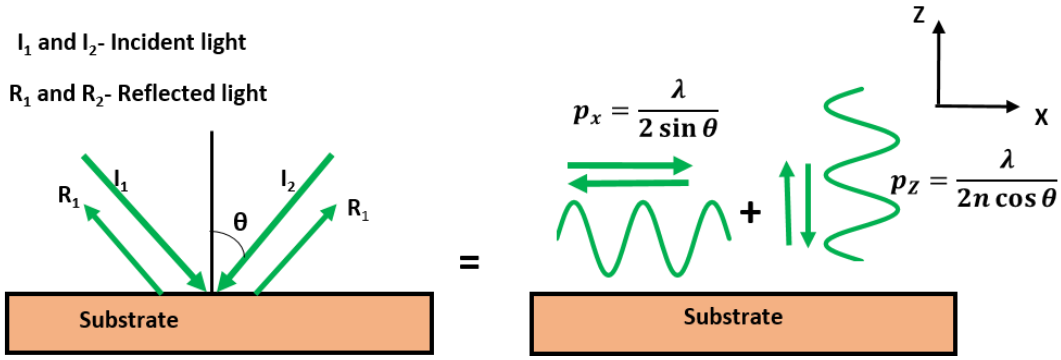

Figure 3.2: Primary and second standing wave formed parallel and perpendicular to the substrate by respective components.

The period of the vertical standing wave is determined by the factors mentioned in equation 3.1 and the refractive index (n) of the photoresist layer. It is given by the following equation 3.2 [124].

$$p_{vertical} = \frac{\lambda}{2n \cos \theta} \qquad (3.2)$$

One way to reduce the effect of the vertical standing wave is to decrease the reflectivity at the interface. In order to prevent these reflections, an extra layer can be added underneath the photoresist layer. This layer should absorb the light and also reflect the light with out of phase from the surface. In general, an anti-reflection coating (ARC) is used to suppress the reflections at the interface. Thus, both the refractive index and the thickness of an ARC play a vital role to suppress the vertical standing wave. An interlayer between the photoresist and the ARC is also sometimes utilized to simplify the pattern transfer (will be discussed in section 3.3.4).

3.3 Sample preparation

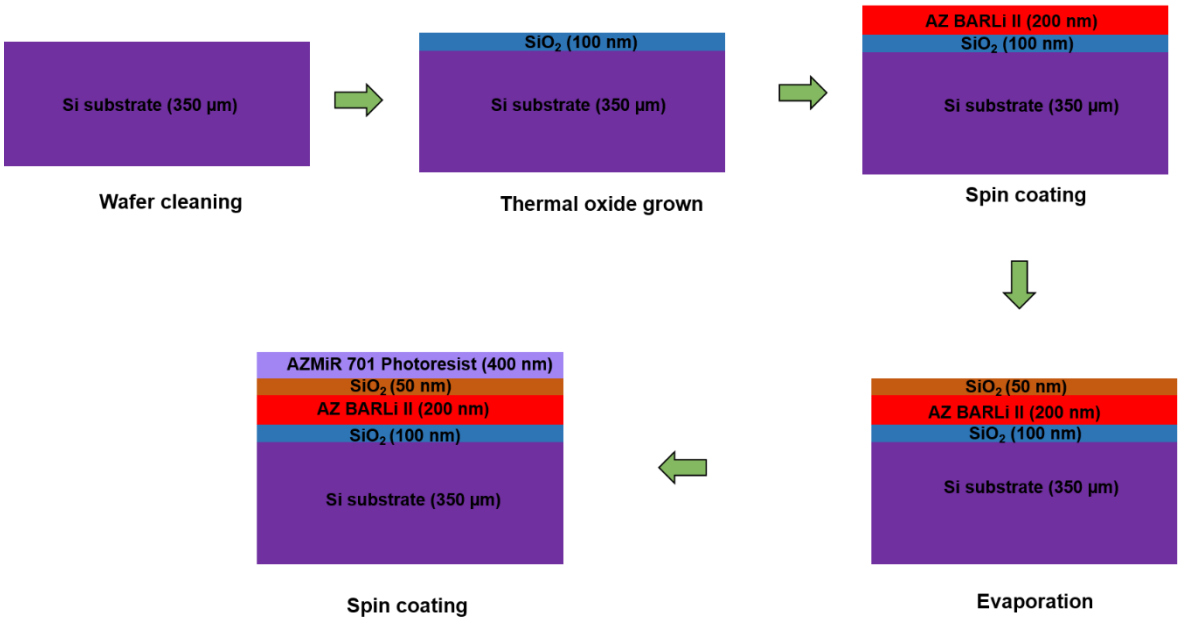

Figure 3.3: Schematic diagram of multilayer stack preparation process for LIL exposures. Note that illustrations are not to scale.

In this work, silicon wafers were mainly used as substrates for the LIL exposures. A silicon oxide layer on the silicon was thermally grown, whereas the silicon oxide layer on the interface between the ARC and photoresist layers was deposited by evaporation

method for further pattern transfers. The overall process steps involved in the typical sample stack preparation are shown in Figure 3.3 for LIL process.

3.3.1 Substrate selection and cleaning

Single-side polished, Czochralski (CZ) grown, 350µm thick, Boron doped p-type silicon wafer with <100> crystal orientation and resistivity of 0.5-1.0 Ωcm was used as substrates. The wafer was immersed in a hot mixture of sulfuric acid (H_2SO_4) and hydrogen peroxide (H_2O_2) (3:1 ratio by volume) for 10 minutes and rinsed with deionized water. This cleaning procedure was used to remove the metals and organic contamination. Then the naturally formed silicon oxide layer on the wafer was removed by immersing the wafer in diluted Hydrofluoric (HF) acid with DI water (1:10) for 10 seconds. After that, the wafer was rinsed by DI water and finally blown with Nitrogen gas.

3.3.2 Thermal silicon oxide layer formation

In order to make the inverted nanopyramid structures on Si, Silicon oxide layer was used as a pattern transfer layer and a hard mask during the RIE etching and KOH wet etching without delamination, respectively. 100nm thick thermal oxide layer was grown on the cleaned Si wafer using quartz tube furnace. The process parameters are listed in Table 3.1. Oxygen gas was bubbled through the water at 95 ^{o}C into the oxidation tube to perform the oxidation in a wet oxygen environment. The chemical reaction of the wet oxidation is given by

$$\mathrm{Si\ (solid)} + 2\mathrm{H_2O\ (vapor)} \rightarrow \mathrm{SiO_2\ (solid)} + 2H_2 \qquad (3.3)$$

Table 3.1 Oxidation process parameter.

Parameters	Conditions
Temperature	1000 °C
Oxidant species	Wet O_2
Film thickness	100 nm
Oxidation time	12 minutes

3.3.3 Anti-reflection coating (ARC)

The optical reflections at the interfaces due to the high reflective substrate could disturb the lithographic pattern results in the LIL process. ARC was employed to reduce the negative effects of the undesirable reflections on the interfaces, more details already discussed in section 3.2. In this work, AZ BARLi II from MicroChemicals GmbH was used as an ARC resist for the interference lithographic exposures. It is designed to perform with positive photoresist without intermixing.

200nm ARC (AZ BARLi II) was deposited onto the thermal oxide Si substrate by spin coating at 2250 rpm for 60sec. Spin-coating is a very widely used method for resist spinning. The sample was then soft baked on a hot plate at 200°C for 60sec.

3.3.4 Evaporated silicon oxide mask layer formation

The sample preparation will vary depending on which pattern transfer method will be performed for fabrication of final hard mold. A bi-layer stack consists of ARC at the bottom layer and photoresist at the top layer is enough for nickel electroplating method, but a tri-layer stack has a thin SiO_2 interlayer between ARC and photoresist. It is required to make subsequent reactive ion etching much easier for silicon mold fabrication. It solves selectivity problem between photoresist and ARC during O_2 plasma etch for etching the ARC layer.

50nm SiO_2 deposition was performed onto the ARC layer using vacuum thermal evaporation (Balzers BA510A). The base pressure of the chamber was in the range of about $3 \times 10{-}6$ mbar and the source material was heated by supplying a high current through the molybdenum aluminium oxide boat of the crucible.

3.3.5 Photoresist spinning

In this work, commercially available i-line positive photoresist (AZMiR 701) was used to record the periodic fringe pattern during LIL process. The undiluted AZMiR 701 resist thickness in the normal spin coating produce thicker layers than the 200-400 nm thickenss required. Hence it was diluted in a ratio 1:3 with PGMEA (1-methoxy-2-propyl-acetate) to achieve lower resist thickness.

In order to improve the adhesion between the photoresist and SiO_2 layer, an adhesion promoter, Hexamethyldisilazane (HMDS, $[(CH_3)_3Si]_2NH$) was applied to form a monomolecular layer on the substrate surface. After the deposition of evaporated SiO_2 layer, Hexamethyldisilazane (HMDS) was spun onto substrate and 400nm diluted positive resist was immediately spin coated using a spinning speed of 3000 rpm for 60 sec and soft baked on a hot plate at 90 ^oC for 60 sec to remove any adsorbed moisture. After that, the prepared Si wafer was cut into 2 cm^2 samples.

3.4 Pattern definition using LIL and development

Once the sample stack preparation was complete, Lloyd's mirror setup was performed to pattern the photoresist. The basic process step to record the interference patterns was as follows: The prepared Si sample was fixed on the substrate holder rotation stage as shown in Figure 3.1. The rotation stage angle was set as calculated from Equation 3.1 for the targeted pattern period. The sample was exposed for the required amount of time using a

50 mW HeCd laser beam operating at 325nm. A time controlled shutter was placed between the spatial filter and rotation stage to control the exposure time during each exposure. The grating pattern was recorded on photoresist with the single exposure. Holes, dots and variations of patterns were recorded by a double exposure with a sample rotated by 90° after the first exposure.

After the exposure, the exposed sample was immersed and carefully agitated in diluted Microchemicals AZ MIF 326 developer solution for 30 seconds. At this stage, the exposed part of the photoresist was dissolved, leaving the required pattern on the photoresist. The sample was rinsed immediately with deionized water (DI) and finally blown with Nitrogen gas. The developed samples were examined by scanning electron microscope (SEM). More details will be presented in the following section 3.4.1 and 3.4.2.

3.4.1 Single exposure pattern

For positive photoresist in LIL, in a single exposure and development step, the periodic line grating pattern will be produced. In order to evaluate the exposure results, an important parameter of the LIL technique the so-called "duty-cycle" (DC) is introduced in this section. The DC is defined as the ratio of the line width (W_{line}) of the periodic structure generated by LIL to the period ($P_{grating}$) and described by Equation 3.4. As described in Equation 3.1, the periodicity of the pattern depends on the wavelength of the light source and the incident angle.

$$Duty\ Cycle = \frac{W_{line}}{P_{grating}} \qquad (3.4)$$

In this case, the wavelength of the laser (325 nm) is a constant value. For a fixed period, the line width value could be controlled by changing the DC value, which depends on the exposed dose. The exposure dose (D) was calculated by multiplying the intensity of the incident laser light (I_0)by the time of exposure (t), yielding a value in energy per unit area [125]. It can be seen that the intensity of the laser and exposure time are the most significant parameters which can impact the exposure results. The intensity of the incident laser light at a fixed incident angle could be considered as a constant value. Thus, there is a linear relationship between the exposure dose and time. The DC value can be controlled by varying the exposure time at a fixed incident angle.

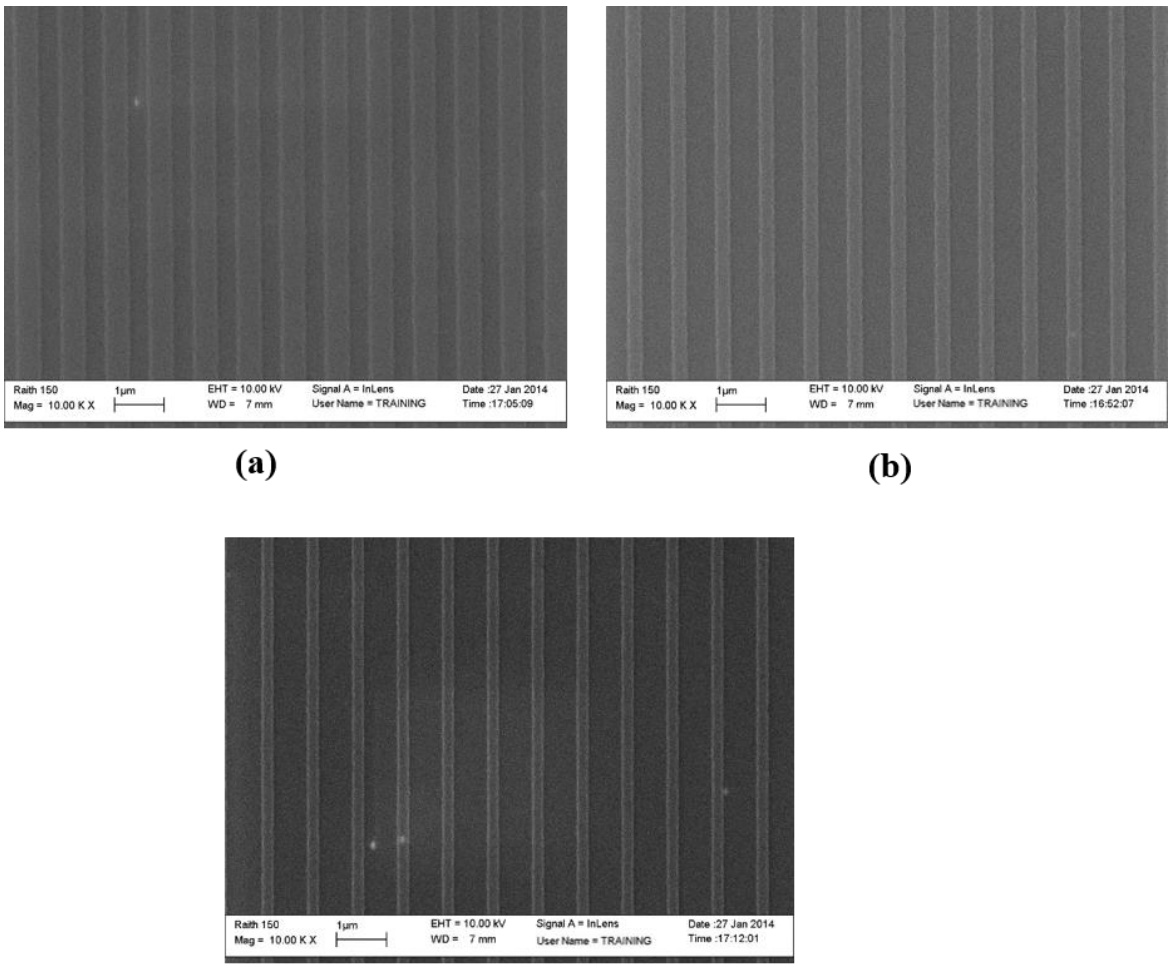

Figure 3.4: SEM images of 900 nm period line grating pattern on photoresist with different line width and exposure time (a) 520nm and 120 sec, (b) 310nm and 240 sec and (c) 250nm and 360 sec.

Figure 3.4 shows the SEM images of the 900 nm period line grating pattern with different exposure time of 120 sec, 240 sec and 360 sec. In this case, the intensity of exposure (0.15mW) and rotating angle of the sample holder ($\theta = 10^o24'$) remained constant. As shown in Figure 3.4, the pattern line width/DC value decreased by increasing the exposure times at a fixed incident angle and intensity. Therefore, it can be concluded that the exposure time is the most important parameter which can influence the exposure results at a fixed incident angle.

For LIL exposures for different periods, one cannot simply assume a constant exposure time, even under identical exposure conditions. As shown in Figure 3.5, the light power density on the sample surface in the case of oblique incidence is lower than that of normal incidence due to increasing the exposed area by the laser at oblique incidence angles. As described in Equation 3.1, the incident angle for a smaller period is larger than that for a larger period. It can be deduced that longer exposure times are required for smaller structure period.

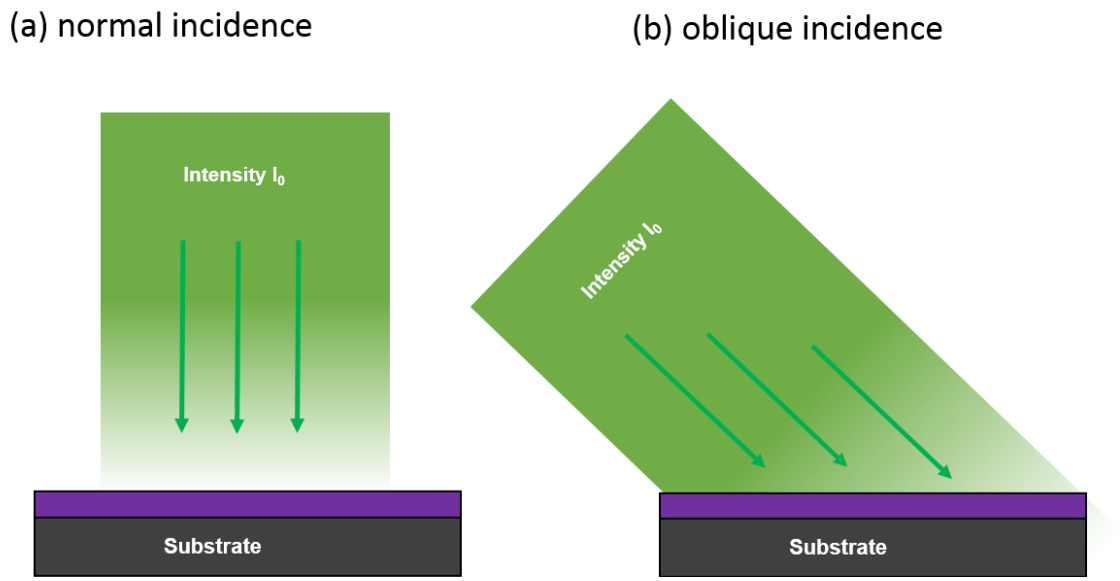

Figure 3.5: Schematic illustration of exposed area at normal incidence and oblique incidence for fixed laser intensity. The substrate area illuminated by laser is larger at oblique incident angles.

Systematic experiments were performed in this work in order to investigate the relationship between the angle of incidence and exposure time. Figure 3.6 shows the resulting SEM images of line grating pattern having 900 nm, 700 nm and 300 nm period with the exposure time of 120 sec, 150 sec and 270 sec, respectively. In order to achieve the period of 900 nm, 700 nm and 300 nm, the angles of incidence were adjusted to 10°24', 13°25' and 32°47', respectively. The exposure time has to increase from 120 sec to 270 sec by using a higher angle of incidence. Thus, larger incident angle (smaller period) requires longer exposure times.

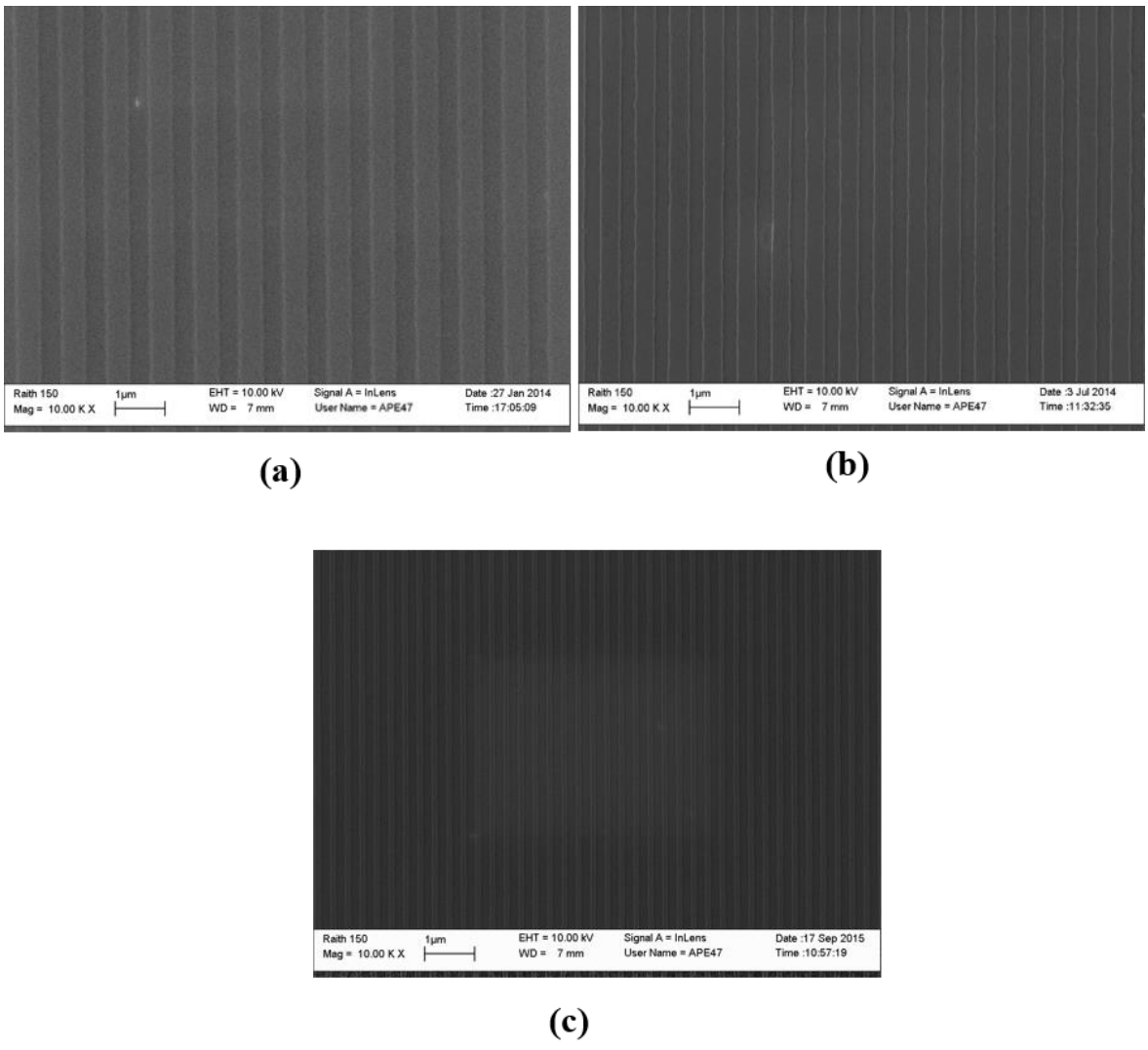

Figure 3.6: SEM images of line grating pattern on photoresist with different period and exposure time (a) 900 nm and 120 sec, (b) 700 nm and 150 sec and (c) 300 nm and 270 sec.

3.4.2 Double exposure pattern

For positive photoresist LIL system, after the double exposure and development, periodic holes or dots will be obtained. Figure 3.7 shows the developed pattern of resist holes and dots with a period of 700 nm square array. The patterns were formed by double exposure IL with the sample rotated by 90° between the two exposures. Exposure times of 70 sec to 120 sec with a 10 sec increment for each experiment were used. In order to achieve the period of 700 nm, the angle of incidence was adjusted to 13°25'. As explained in the previous section, exposure dose depends mainly on the exposure time for a constant laser intensity at fixed incident angle.

Even at the lowest exposure dose, a pattern of holes was formed as shown in Figure 3.7(a), although there was a little variation in the size of holes. With exposure dose increasing, the size of the holes increased and become more uniform as shown in Figures 3.7(b) and (c), then holes disappeared but some dots still linked together as shown in Figure 3.7(d). Increasing the exposure dose further, results in discrete dot array as shown in Figure 3.7(f). It can be clearly seen that exposure time is the most important parameter which can significantly influence the size and type of pattern structures. In order to fabricate the inverted nanopyramid on Si substrate, a pattern of resist holes was used in this work. More details about the pattern transfer and formation of inverted nanopyramid will be discussed in the next section.

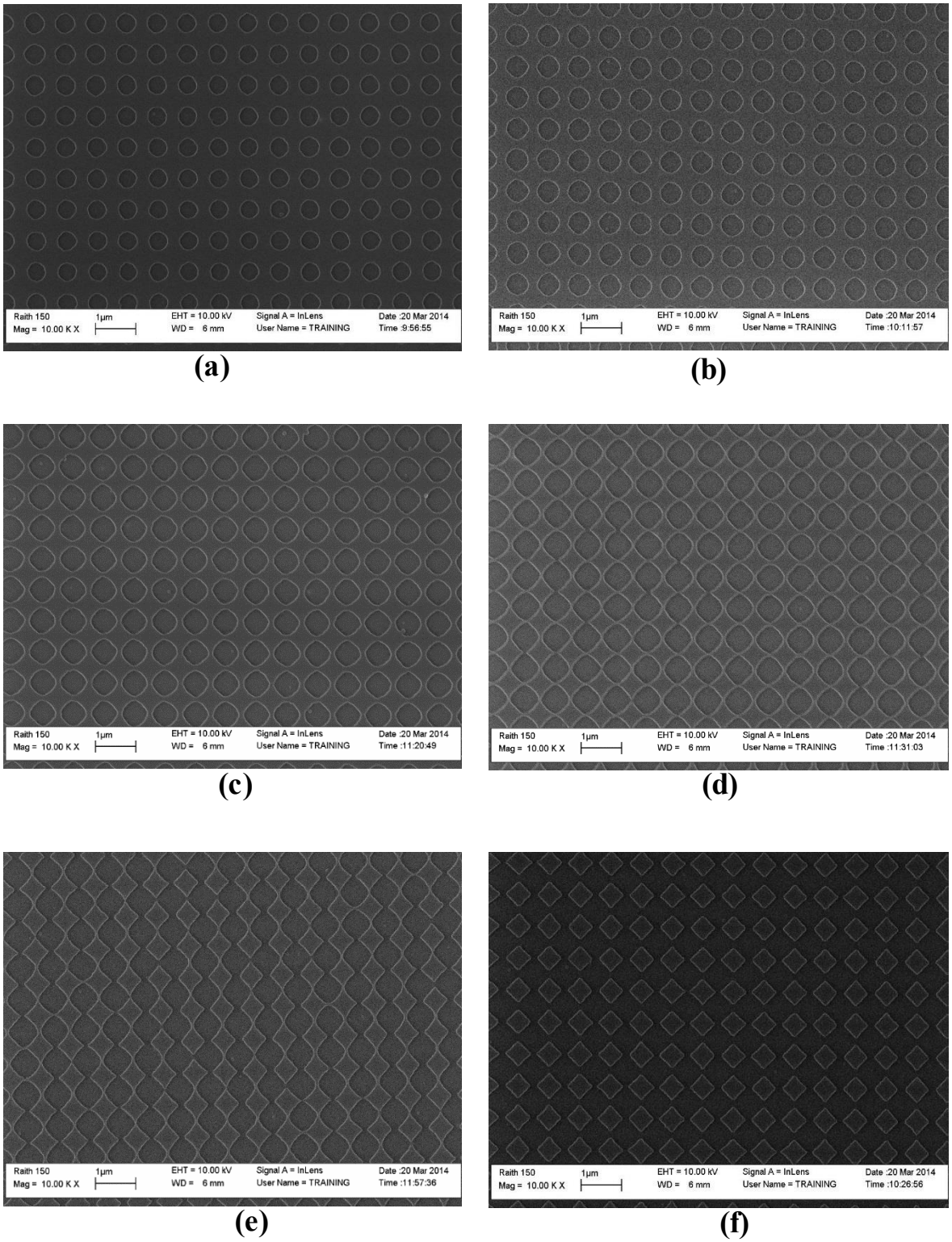

Figure 3.7: SEM images of holes and dots pattern on photoresist produced by double exposure IL with a period of 700 nm and exposure times of (a) 70 sec, (b) 80 sec, (c) 90 sec, (d) 100 sec, (f) 110 sec, and (d) 120 sec for each exposure. The samples were rotated by 90° between the two exposures.

3.5 Pattern transfer and formation of inverted pyramid

The periodic inverted nanopyramid structures were fabricated on Si substrate by laser interference lithography and subsequent pattern transfer by combined reactive ion etching and KOH wet etching. The schematic illustration of the fabrication process of inverted nanopyramid structure on Si substrate is shown in Figure 3.8. After the LIL patterning of photoresist, the resist pattern of holes was transferred onto the thermal oxide layer through a subsequent Reactive Ion Etching (RIE) steps. Then, the inverted pyramid structures were formed by KOH wet etching. Finally, the thermal oxide layer was removed by buffered Hydrofluoric etching. More details of the fabrication process will be discussed in the next section.

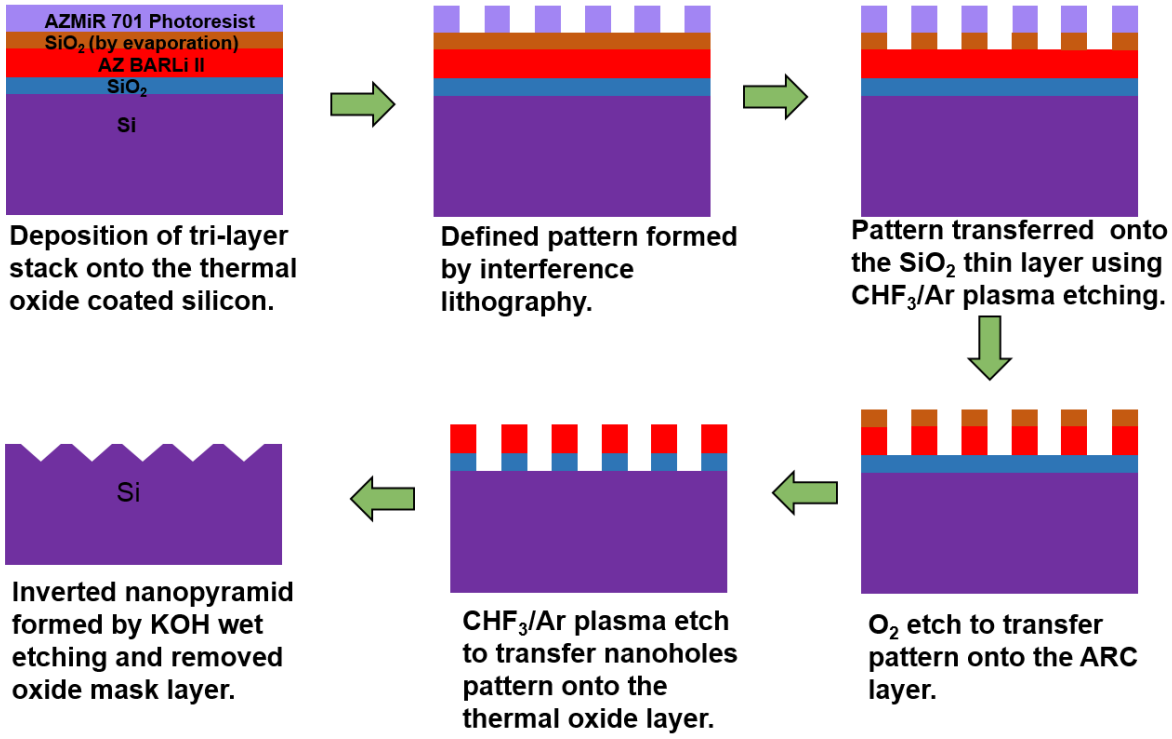

Figure 3.8: Schematic illustration of the fabrication process of inverted nanopyramid structures on a Si substrate.

3.5.1 Dry plasma etching

In this work, an Oxford PlasmaLab80 reactive ion etching system was utilized for all the dry plasma etching steps. The RIE etching process parameters such as flow rate of the processing gases, pressure, substrate temperature, RF power and etching time were carefully optimized for the pattern transfer.

3.5.1.1 Pattern transfer into silicon oxide layer

The resist pattern produced by LIL served as the etching mask for the RIE pattern transfer step into the thermally evaporated silicon oxide layer. Usually, the photoresist layer is etched faster than the ARC layer. Therefore the resist pattern of holes generated by LIL cannot be directly transferred into the substrate. In order to obtain a high etching selectivity between the ARC and the photoresist, thin SiO_2 was deposited between the two layers. Before the SiO_2 etching process, a short O_2 plasma etch was performed to remove any residual photoresist at the bottom of the holes. The CHF_3/Ar plasma etching was performed to transfer the pattern of holes into thin SiO_2 interlayer. The RIE process parameters for O_2 plasma for descumming the residual resist and transferring the pattern into a SiO_2 layer using CHF_3/Ar plasma are illustrated in Table 3.2.

Table 3.2: RIE recipes for removal of residual resist layer and transferring the pattern into SiO_2 layer.

RIE Parameters	Removal of residual resist layer	Pattern transfer into SiO_2 layer
Gas	O_2	CHF_3/Ar
Flow rate	10 sccm	25/30 sccm
RF Power	100 W	150 W
Pressure	100 mTorr	100 mTorr
Temperature	295 K	300 K
Time	10 sec	1 min 30 sec
Masking material	-	Photoresist

The SEM image of the developed resist pattern of holes with a period of 650 nm square array is shown in Figure 3.9(a). In order to achieve the period of 650 nm, the angle of incidence was adjusted to 14°28'. Figure 3.9(b) shows a SEM image of the pattern of holes transferred into a SiO_2 masking layer. It can be seen that the pattern uniformity remains very high.

(a)

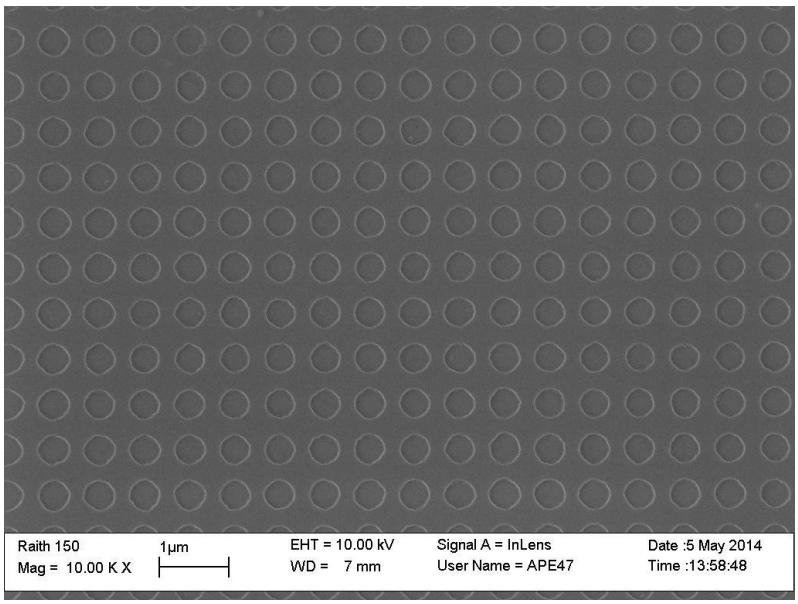

(b)

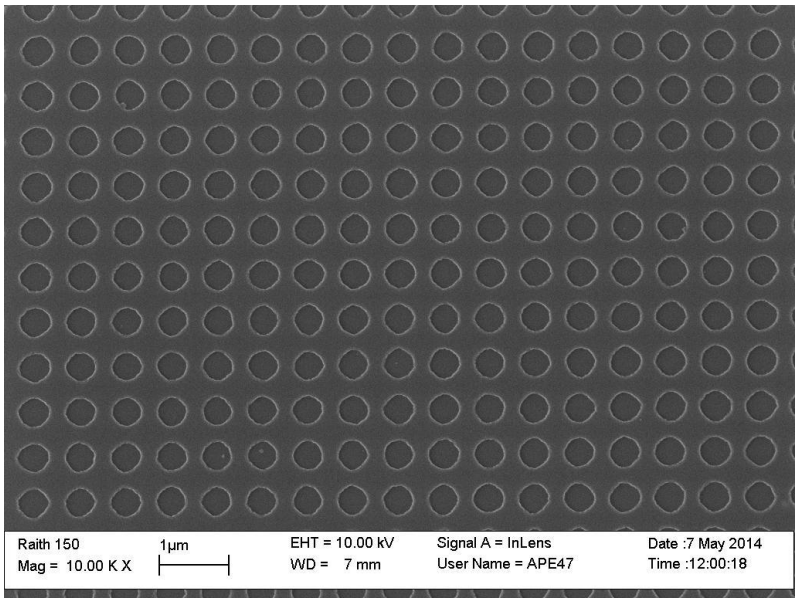

Figure 3.9: SEM images showing (a) The developed patterns on resist with a period of 650 nm and (b) patterns transferred into SiO_2 masking layer after CHF_3/Ar plasma etching.

3.5.1.2 Pattern transfer into ARC layer

The patterned SiO_2 interlayer acted as a mask layer to transfer the pattern of holes into the ARC layer. The O_2 plasma etching was performed to transfer the pattern into ARC layer. Table 3.3 outlines the optimized RIE parameters of O_2 plasma etching for transferring the patterns into ARC layer. Figure 3.10 shows the SEM image of patterned ARC layer after the O_2 plasma etching.

Table 3.3: The optimized O_2 plasma RIE parameters for pattern transfer into ARC layer.

RIE Parameters	Transferring the pattern into ARC layer
Gas	O_2
Flow rate	10 sccm
RF Power	100 W
Pressure	100 mTorr
Temperature	300 K
Time	13 min 30 sec
Masking material	SiO_2 layer

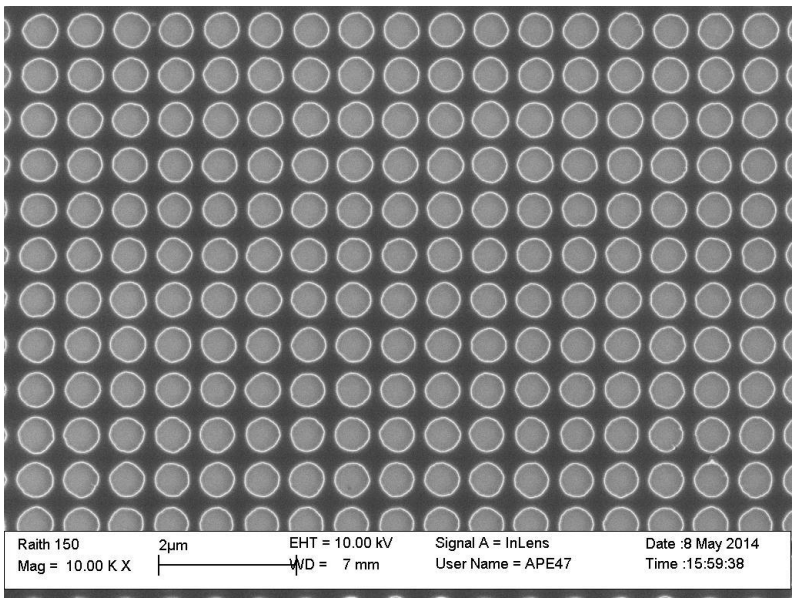

Figure 3.10: SEM images of patterns transferred into ARC layer after O_2 plasma etching.

3.5.1.3 Pattern transfer into thermal oxide layer

The patterned ARC layer served as a mask layer to transfer the pattern of holes into a thermal SiO_2 bottom layer. The *CHF_3/Ar* plasma etching was performed to transfer the pattern into ARC layer. Table 3.4 shows the optimized RIE parameters for *CHF_3/Ar* plasma etching for transferring the patterns into a SiO_2 bottom layer. Figure 3.11 shows the SEM image of patterned SiO_2 bottom layer after the *CHF_3/Ar* plasma etching. It can be observed that the RIE etching process induced a slight enlargement of holes diameter while the uniformity was improved.

Table 3.4: The optimized *CHF_3/Ar* plasma RIE parameters for pattern transfer into thermal SiO_2 bottom layer.

RIE Parameters	Transferring the pattern into SiO_2 bottom layer
Gas	*CHF_3/Ar*
Flow rate	25/30 sccm
RF Power	150 W
Pressure	100 mTorr
Temperature	300 K
Time	3 min 30 sec
Masking material	ARC layer

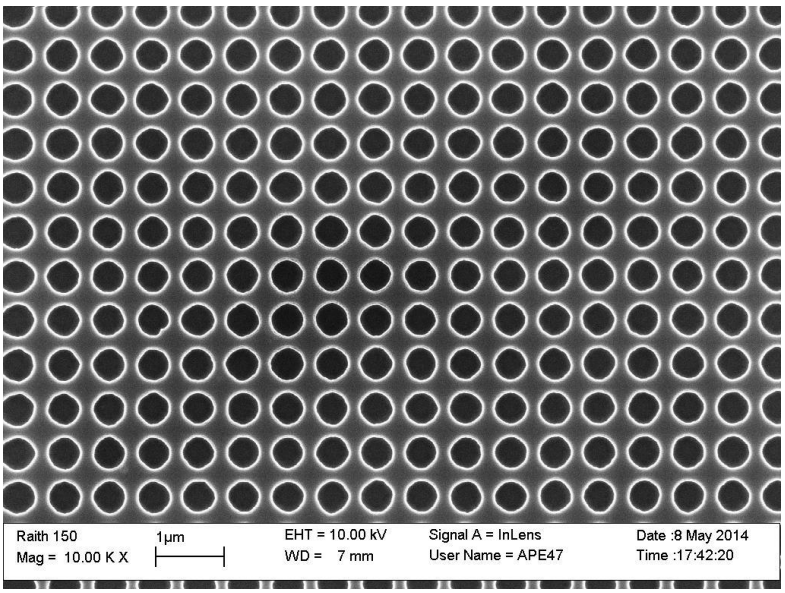

Figure 3.11: SEM images of patterns transferred into SiO_2 layer after *CHF_3/Ar* plasma etching.

3.5.2 Wet chemical anisotropic etching

After the RIE process, the next process step was anisotropic wet chemical etching in order to form inverted pyramid structures into the silicon substrate. The anisotropic chemical etching characteristic of single crystal silicon substrate varies according to the crystallographic orientation of the substrate bulk material. Anisotropic etchants such as potassium hydroxide (KOH), Sodium hydroxide (NaOH), Cesium hydroxide (CsOH), Ammonium hydroxide (NH4OH), tetramethylammonium hydroxide (TMAH) and hydrazine etch certain crystallographic planes at different etch rates. The etch rate of the (111) plane is significantly low compared to the (100) plane etch rate mainly due to a number of dangling bonds in each unit cell [126]. The (111) plane has the lowest dangling bond; more back bonds must be broken and therefore the etch rate is low. The etch rates for anisotropic wet chemical etchants is mainly dependent on the concentration of the solution and temperature. As schematically illustrated in Figure 3.12, the inverted nanopyramid structure could be produced with <100> crystalline orientation of silicon substrate using anisotropic wet etching. Anisotropic etchants make an angle of 54.7° for the <100> oriented Si substrate, which is the angle between (100) and (111) plane.

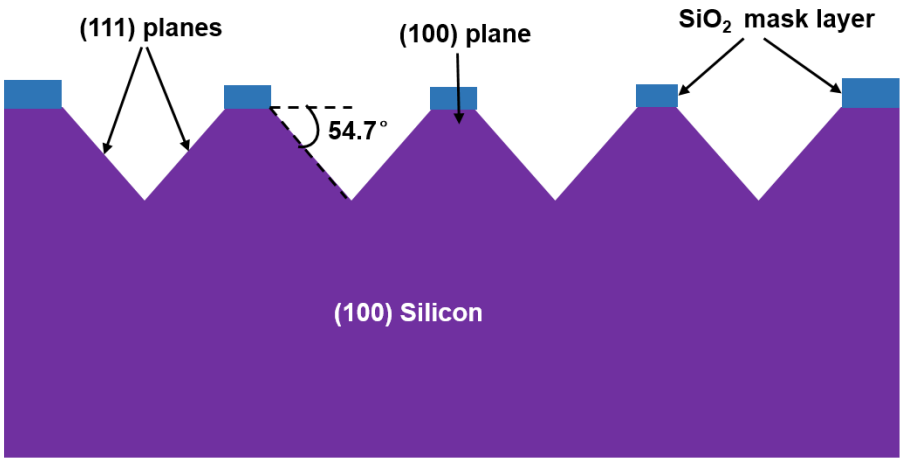

Figure 3.12: An anisotropic wet etch on a (100) silicon substrate creates inverted nanopyramid structure.

The chemical etchant for anisotropic wet etching used in this work is typically a 30 wt. % KOH diluted in deionized water. SiO_2 was chosen as a hard mask layer mainly due to the high etch selectivity of KOH solution between Si and SiO_2. The inverted pyramid structure on a (100) Si substrate was fabricated by wet etching in 30% KOH solution at 80°C for 170 sec. The KOH solution was kept in a temperature controlled bath at 80°C. Figure 3.13 shows the SEM image of the resulting inverted nanopyramid structure having a width of about 600 nm, and separation of about 100 nm, obtained from the same sample as in Figure 3.9.

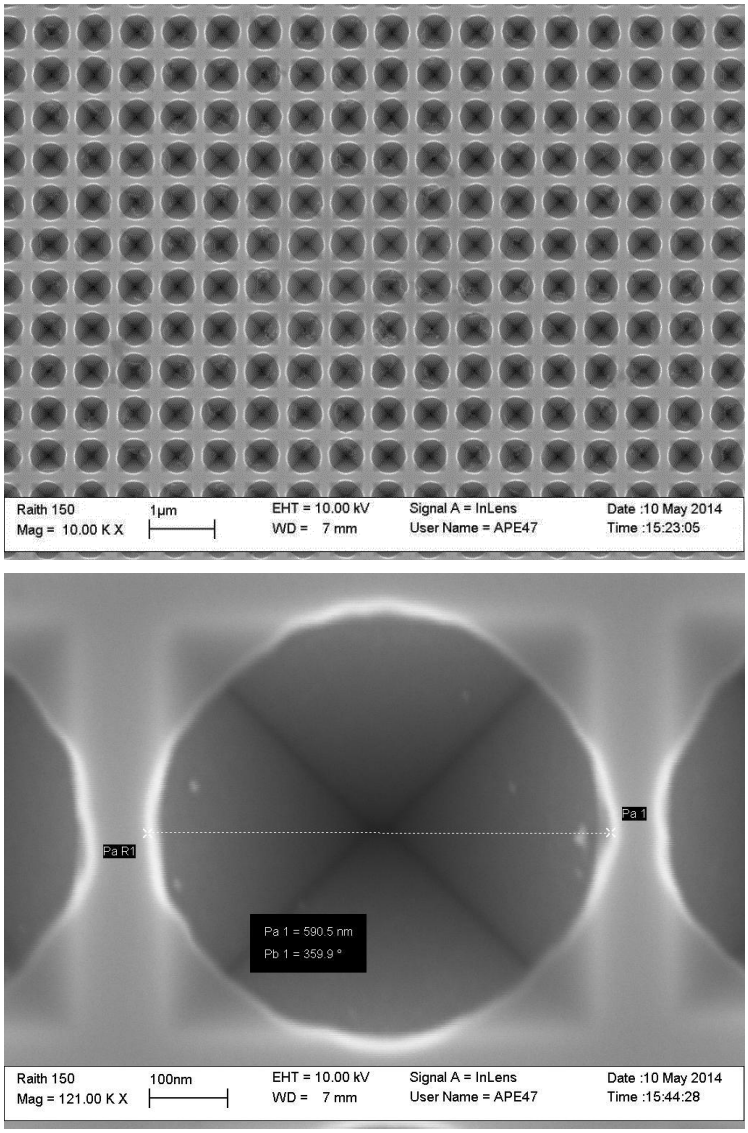

Figure 3.13: SEM images of inverted nanopyramid structures on Si substrate with SiO_2 masking layer after KOH wet etching. (a)Low- magnification image and (b) high-magnification image.

3.5.3 Removal of silicon oxide mask layer

There were at least two techniques available for the removable of the SiO_2 mask layer, dry etching using CHF_3/Ar plasma, or wet etching using HF solution. In this work, the wet etching process was used to avoid any surface damage or increased surface roughness. To remove the SiO_2 mask layer from the patterned samples, the sample was immersed in buffered HF (6:1 volume ratio of NH_4F solution to 49% HF) for 3 min, washed with DI water, and blown dry with N_2.

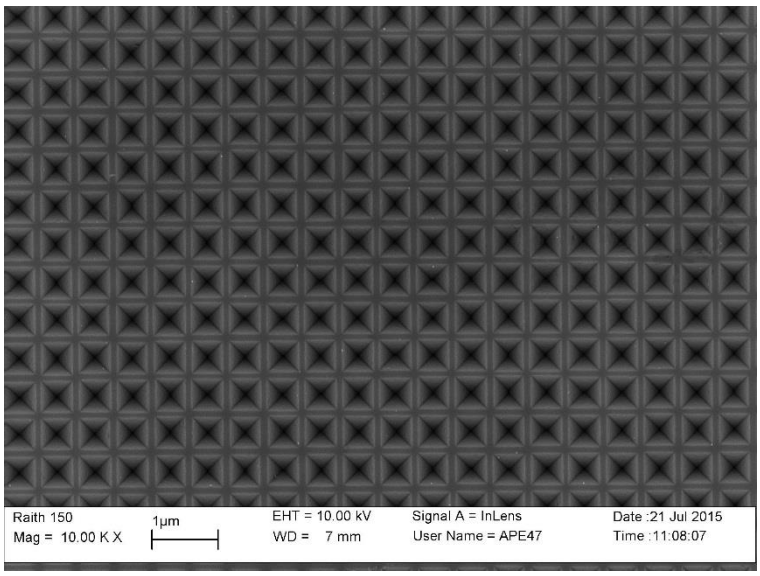

Figure 3.14: SEM images of inverted nanopyramid structures on Si substrate after removal of SiO_2 masking layer.

The SEM image of the formed periodic inverted nanopyramid structures on Si substrate after removal of the SiO_2 masking layer is shown in Figure 3.14. It can be clearly seen that all the inverted pyramid structures were completely formed and centered without showing any overlapping between neighbors. It can also be observed that the size of the inverted pyramid increased slightly compared with a diameter of the nanoholes as in the Figure 3.13(a) due to undercutting during KOH wet etching. The cross-sectional view of the SEM image shown in Figure 3.15 clearly illustrates that the inverted pyramid structures were completely formed and the angle between the (100) and (111) was fixed

at 54.7° as described in the previous section. The fabricated inverted nanopyramid structures on Si Substrate were used as a master mold in the replication process for UV-NIL. The replication process of the inverted nanopyramid structures will be introduced in Chapter 4.

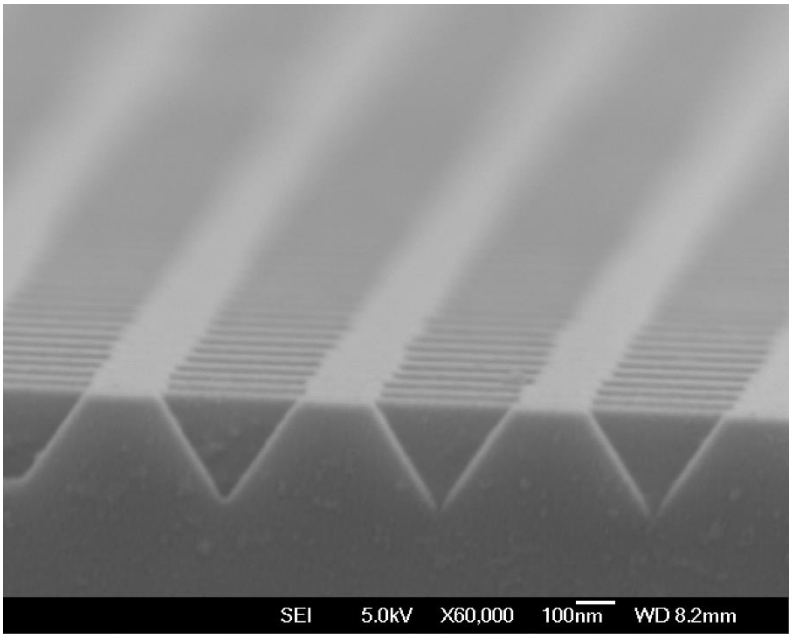

Figure 3.15: Cross sectional view SEM image of inverted nanopyramid structures on Si substrate.

3.6 Summary

In this chapter, the fabrication of inverted nanopyramid structures was presented. Maskless LIL was employed as a high-throughput, high resolution and low cost technique for the fabrication of large scale periodic nanostructures. The inverted nanopyramid structures were fabricated on 10×10 mm Si substrates by LIL and subsequent pattern transfer by combined reactive ion etching and KOH wet etching. The pattern of nanoholes was recorded on AZMiR 701 i-line positive photoresist using LIL by double exposure. The CHF_3/Ar plasma etching was performed to transfer the nanoholes pattern into thin SiO_2 interlayer. Then, the O_2 plasma etching was performed to transfer the pattern into

ARC layer with thin SiO_2 as mask. The pattern was transferred into the thermal oxide layer using CHF_3/Ar plasma etching. The inverted pyramid structures were completely formed on Si substrate by KOH wet etching and the SiO_2 mask layer was removed by buffered HF etching. The multilayer stack was developed to enhance the pattern quality by suppressing substrate reflection and to transfer the recorded pattern into bottom layer. In the following Chapter, the replication process of the fabricated inverted nanopyramid structures will be presented.

Chapter 4 UV Nanoimprint Lithography - Replication of nanopyramid structures

4.1 Introduction

Nanoimprint lithography (NIL) is an emerging method of fabricating micro/nanometer scale patterns with a high throughput, low cost, and high resolution manufacturing technology [127, 128]. Unlike traditional optical lithographic methods, which create pattern definition through the use of photons or electrons to modify the physical and chemical properties of the imaging resist layer, NIL depends on direct mechanical deformation of the resist materials and can therefore achieve resolutions beyond the limitations set by beam scattering or light diffraction that are encountered in conventional lithographic techniques [80].The resolution of the NIL is mainly determined by the resist molecule size and the minimum feature size of the template that can be fabricated. Compare with optical lithography, the key benefit of NIL is its capability to produce feature size down to sub-10 nm over a large area with low cost and high throughput [129]. In addition, nano-sized patterns can easily be formed on different substrates such as silicon wafers, flexible polymer films, glass substrates, and even non-planar surfaces.

Nanoimprint lithography was first proposed and demonstrated by Stephen Chou et al. in 1995 as a low cost and high throughput alternative to e-beam lithography and photolithography [130]. In general, NIL can be classified into two fundamental types; Hot Embossing Lithography (HEL) also known as Thermal Nanoimprint Lithography (TNIL), and UV-based Nanoimprint Lithography (UV-NIL). Currently, many different variations of lithographic techniques have been developed based on NIL, typical examples include roll to roll imprint lithography [131], step and flash imprint lithography

(SFIL) [84], laser assisted NIL [85], microcontact printing [86], reverse imprint lithography [87], and step and stamp imprint lithography (SSIL) [132].

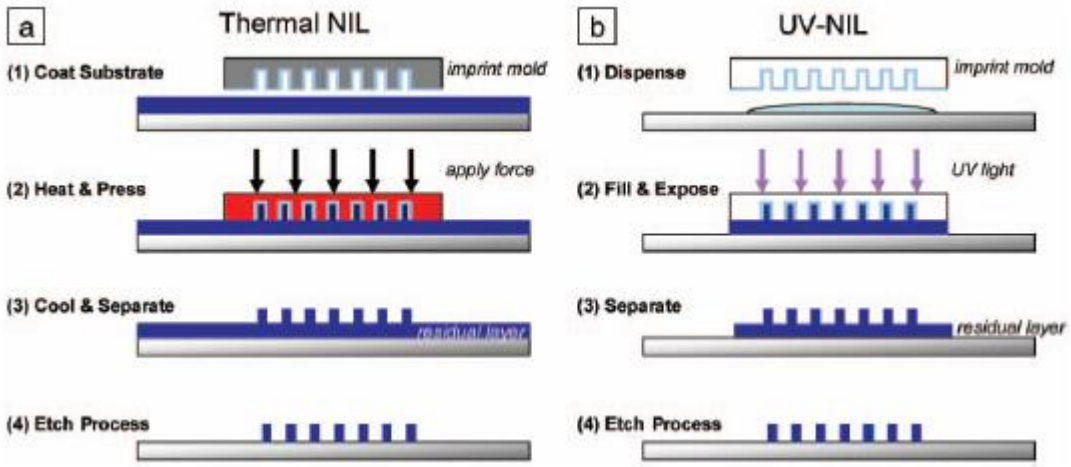

Figure 4.1: Two fundamental process types for NIL [83].

Figure 4.1 shows the process steps for thermal nanoimprint lithography and ultraviolet-assisted NIL [83]. NIL is based on the mechanical deformation of the resist using a mold (template and stamp) consisting of micro/nanopattern in a thermo-mechanical process or UV curing process. In a standard TNIL, a thermoplastic polymer layer is spun coated onto a substrate. The mold containing predefined micro/nanopattern is brought into contact with a thin polymer film on a substrate, and they are pressed together under certain pressure (From 600 to 1900 psi for PMMA). When heated up above the glass transition temperature of the polymer (105°C for PMMA), the feature pattern on the mold is imprinted into the melt polymer film. The thin polymer film is solidified by cooling it below the glass transition temperature of the polymer film before the mold is released. Alternatively, UV-NIL technique is based on the use of UV curable liquid photoresist instead of a thermoplastic polymer as a resist, which can easily be deformed at room temperature. After the mold and UV curable resist coated substrate are pressed

together, the resist is cured by UV light exposure and becomes solid. After the mold is released, the pattern in the thin polymer film can be further transferred into the underneath substrate by a subsequent pattern transfer process, for instance, reactive ion etching.

The UV-NIL technique has several prominent advantages over the thermal NIL, which include the capability of UV-NIL to be performed at room temperature, which helps eliminate the issues resulting from thermal expansion mismatch between the substrate, resist and mold [133]. In addition, the UV-NIL imprinting process involves a lower viscosity of the photoresist, which allows the imprinting process to be performed at a lower pressure compared to thermal NIL [134, 135]. The cycle time of the UV-NIL process is shorter than the thermal NIL due to the elimination of temperature cycle, which improves the process throughput [136]. However, UV-NIL process requires either a transparent substrate or a transparent mold.

NIL's ability to provide low-cost, high resolution, high throughput and highly repeatable patterning of nanoscale structures offers potential benefits to numerous electrical, optical, photonic, magnetic, and biological applications. These include hybrid plastic electronics [137], nanoelectronics devices in Si [138], organic laser [139], organic light emitting diode (OLED) pixels [140], solar cells [12, 81, 141], broadband polarizers [142], high density quantized magnetic disks [143], nanoscale protein patterning [144] and manipulating DNA in nanofluidic channels [145]. In this study, UV-NIL process was mainly used to replicate nanopyramid structures for solar cell applications.

In this chapter, the development of the ultraviolet nanoimprint lithography (UV-NIL) and imprint processes for the replication of upright nanopyramid and inverted nanopyramid structures are presented. First, the sample preparation processes for UV-NIL are introduced in section 4.2. Then, imprint processes for the replication of upright

nanopyramid and inverted nanopyramid structures and patterns analysis are described in section 4.3. Finally, the chapter summary is discussed in section 4.4.

4.2 Preparation for imprint process

The materials required for UV-NIL are a mold consisting of predefined surface relief nanostructures and a suitable UV curable resist material that can be deformed and hardened to replicate the shape of the impression. In this section, the anti-sticking layer preparation on the master mold and UV curable resist material preparation on a glass substrate for imprint process are presented.

4.2.1 Master mold fabrication

The mold is one of the most vital elements for the NIL process as it contains the pattern information and details. The mold used in NIL can essentially be any type of solid materials that has a high hardness and durability properties. A variety of materials such as Silicon, Silicon dioxide, silicon nitride, quartz, glass, nickel, etc., have been used to make molds for NIL.

In this study, the periodic inverted nanopyramid structure on silicon substrate was used as a master mold substrate for the imprint process. The periodic inverted nanopyramid structures were fabricated on Si substrate by LIL and subsequent pattern transfer by combined reactive ion etching and KOH wet etching. The details of the fabrication process of inverted nanopyramid structures can be found in Chapter 3.

4.2.2 Anti-sticking layer treatment on mold

A master mold for NIL has a high density of nanoscale protrusion features on the mold surface, which effectively enhances the total surface area. The increased surface area of the mold contacts with the imprinted resist leading to strong adhesion of the imprinted resist to the mold. This effect can be easily observed by the sticking of the resist to the mold without special surface treatment. The surface treatment for NIL molds not only avoid the adhesion between the mold materials and imprint resists which can improve the imprint qualities, but it also increases the mold lifetime significantly by preventing surface damage and contamination. Hence, it is necessary to deposit a low surface energy release layer or anti-sticking layer directly onto the master mold prior to the imprint process. In order to achieve this, self-assembled monolayers (SAM) with low surface energies such as Teflon [146, 147], and silane materials [148-150] have been reported as an anti-sticking layer to enhance the demolding capabilities and to increase the mold lifetime. The most widely used anti-sticking layer approach is a SAM of a fluorosilane release agent either by a vapor phase or solution phase deposition.

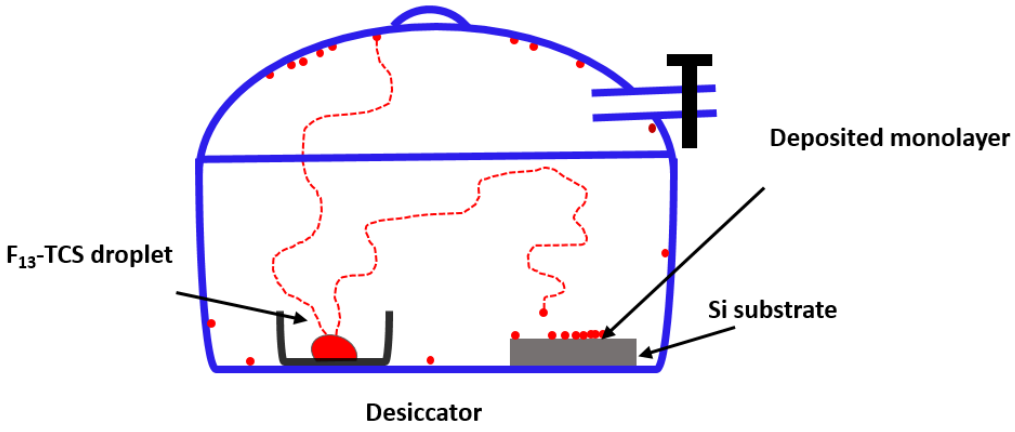

Figure 4.2: Schematic representation of the self-assembled monolayer (SAM) coating using a natural evaporation method of F_{13}-TCS in a vacuum desiccator.

In this work, A 1H, 1H, 2H, 2H-Perfluorooctyl-trichlorosilane also known as F_{13}-TCS solution from Sigma-Aldrich was used as an anti-sticking layer on molds for NIL. A SAM coating was formed on the mold surface with F_{13}-TCS agent via a vapor deposition method inside the desiccator at room temperature. In this method, the sample was baked in the oven at 90°C for 30 minutes to fully dry the surface from water moisture and then cooled down to room temperature. A small droplet of the anti-sticking solution (F_{13}-OTCS) was dispensed at the center of a small petri dish which was loaded with mold into a vacuum desiccator as shown in Figure 4.2. The substrate was left to react for 2 hours at room temperature, then removed from the desiccator and baked in the oven at 90°C for one hour.

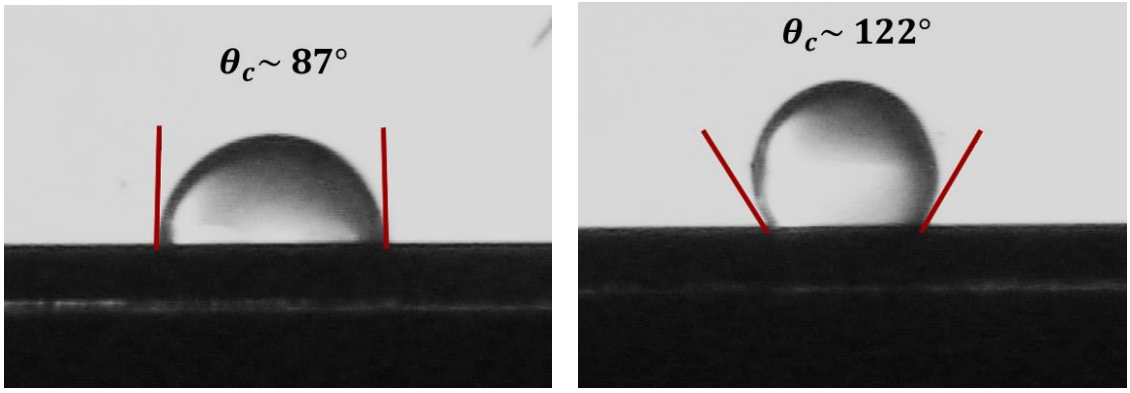

(a) Inverted nanopyramid structured Si substrate.

(b) Inverted nanopyramid structured Si substrate with SAM.

Figure 4.3: The contact angles on the surface of inverted nanopyramid structured Si substrate at normal conditions and after being coated with an anti-adhesive monolayer.

Prior to the imprint process, the contact angle measurements were performed on the inverted nanopyramid textured Si surfaces before and after the surface treatments to quantify the changes of the surface energies. Figure 4.3 shows the contact angle of inverted nanopyramid textured Si surfaces before and after the surface treatments. The

contact angle of the inverted nanopyramid textured Si surface was increased from 87 to 122° after coated with an anti-sticking layer of F_{13}-TCS which is highly hydrophobic. It can be clearly seen that F_{13}-TCS SAM coating was enhanced the anti-adhesive properties on the inverted nanopyramid textured Si surface which is essential for the imprinting process.

4.2.3 Substrate preparation

The low iron glass with a thickness of 0.5 mm was used as a substrate for UV curable resist. The UV curable resist plays an important role in the successful applications of UV-NIL where adhesion between the substrate and resist should be high, whereas, between the mold and resist should be as low as possible [136]. The resist that was used in this work was OrmoStamp from Micro Resist Technology, which is UV curable inorganic-organic hybrid polymer with high transparency for UV and visible light designed for UV imprinting or molding. It is suitable for the fabrication of nanopatterns in many applications such as optical devices, photonic crystals, solar cells, and micro/nanofluidics.

The UV curable resist must have a strong interfacial bonding to the substrate on the one hand, but not stick to the mold surface in the imprint process [151]. In order to achieve a strong adhesion between the resist and glass substrate, an extra cleaning process combined with oxygen plasma treatment were performed and also adhesion promoter was added on the glass substrate prior to the resist spin coating. The OrmoPrime08 from micro resist technology was used as an adhesion promoter solution based on organofunctional silanes. It has been designed to promote the adhesion of OrmoStamp, OrmoComp, OrmoClear, OrmoCore, and OrmoClad to various substrates, like silicon, glass and quartz.

The glass substrate was cleaned with acetone, methanol, and isopropyl alcohol (IPA) solvents in an ultrasonic bath and then rinsed with deionized water and finally dried with Nitrogen gas. Next, the substrate surface was treated using short oxygen plasma to enhance optimum adhesion at the interface between the glass and the OrmoPrime08. After that, the substrate was baked using an oven at 200°C for 30 minutes and cooled down to room temperature immediately before coating. OrmoPrime08 was deposited onto the glass substrate by spin coating at a spin speed of 4000 rpm for 60 sec. The spin-coated film was then baked on a hot plate at 150°C for 5 minutes and cooled down to room temperature. Finally, OrmoStamp resist was spun coated onto the OrmoPrime08 layer coated substrate at a spinning speed of 6000 rpm for 60 sec. After spin coating, the substrate coated with resist was thermally prebaked on a hot plate at 80°C for 2 minutes to enhance the homogeneity of the resist thickness and to increase the adhesion between the resist and substrate.

4.3 Nanoimprint process

To perform the imprint experiment, a vacuum operated manual imprint tool was used in this work. The two manual imprint tools were designed and employed to perform the imprint processes on 20 × 20 mm^2 and 10 × 10 mm^2 samples, respectively. The vacuum operated imprint tool was fabricated in the department's mechanical workshop using aluminium. It creates a vacuum environment in order to reduce the air bubbles trapped in between the resist and mold during the imprint process.

Figure 4.4 (a) and (b) shows the schematic cross-sectional view and the optical image of the imprint tool used in this work, respectively. It was attached to the Karl Suss Mask Aligner (MA-6) exposure system to perform as a UV-NIL tool. The Mask Aligner system uses i-line 365 nm wavelength UV source for exposure. The vacuum line of the Mask

Aligner system is connected to the imprint tool that used to hold the mask onto the mask holder. In this work vacuum pressure of 4mbar and 365 nm wavelength UV illumination were employed to perform the imprint process.

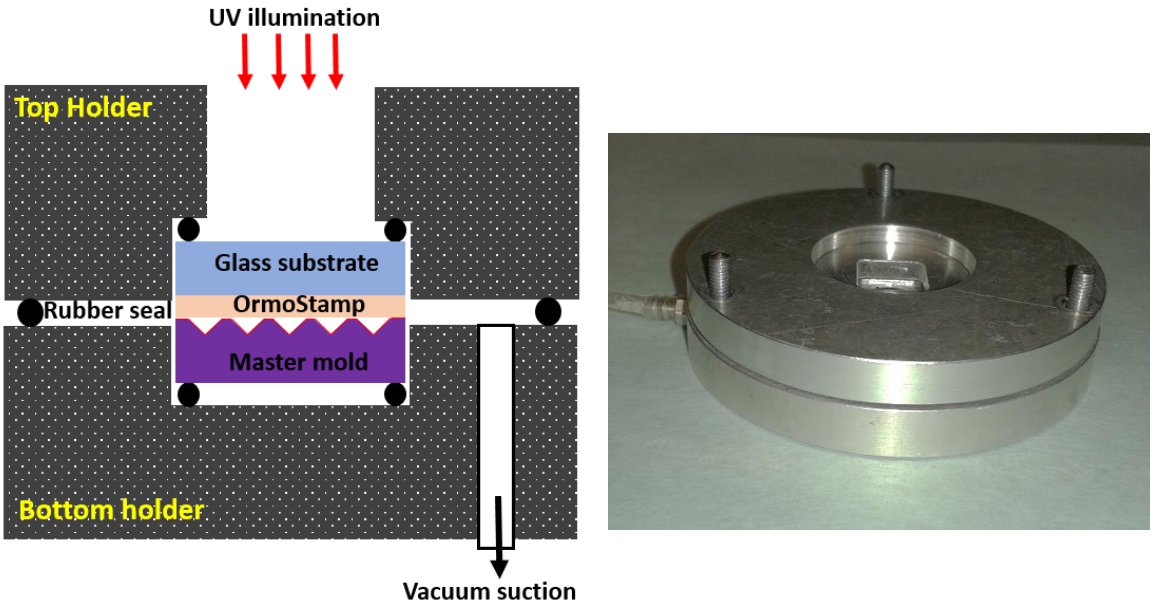

(a) The schematic cross sectional view (b) The optical image angle view

Figure 4.4: The vacuum operated manual imprint tool used for UV-NIL in this work.

In order to replicate the original master mold, two subsequent imprint processes need to be applied. In this work, periodic inverted nanopyramid textured Si substrate was used as a master mold. In the first step of the imprint process, the negative of the pattern on the master mold was replicated from Si master mold to resist coated glass substrate, i.e. inverted nanopyramid structures on Si master mold become upright nanopyramid structures on resist coated glass substrate. In the second step of imprint process, the inverted nanopyramid structures were replicated on resist using upright nanopyramid patterned glass substrate as a master stamp.

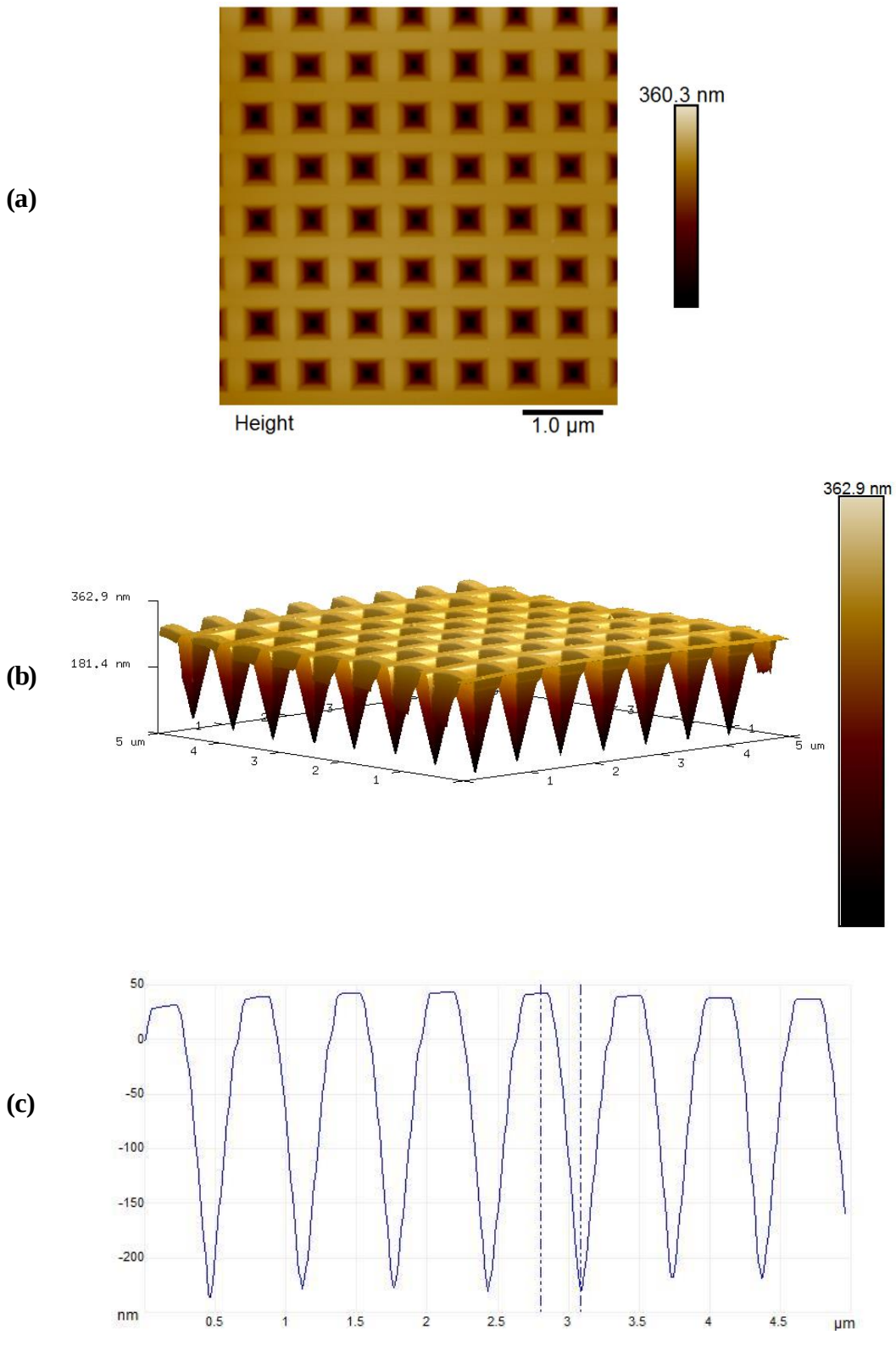

Figure 4.5: AFM images of inverted nanopyramid structured master mold (a) 2-D view, (b) 3-D view and (c) cross sectional traces.

Figure 4.5 shows the AFM images and cross-sectional traces of periodic inverted nanopyramid structures on Si The periodic inverted nanopyramid structure have features with a width of about 450 nm, a height of about 300 nm and separation of about 150 nm.

4.3.1 Imprint - Upright nanopyramid structures replication

Figure 4.6 illustrates the schematic diagram of the first imprint process steps to create the upright nanopyramid structures into UV curable resist coated glass substrate from inverted nanopyramid structured Si master mold. The F13-TCS SAM coated Si master mold coated with F13-TCS SAM /UV curable resist coated glass substrate was loaded into the imprint tool. The SAM coated Si master mold and UV curable coated glass substrate were prepared as described in section 4.2. A vacuum pressure was set to 4 mbar and the Mask Aligner (MA-6) system was then activated. The resist was cured under a UV exposure for 4 min using 4.4 mW/cm^2 illumination intensity with 365 nm UV source at room temperature. A manual de-molding process was utilized by applying gradual force using a scalpel at one corner of the mold in order to delaminate between the two material surfaces. Subsequently, the replicated substrate was thermally baked in an oven at 150°C for 2 hours to improve the film thermal and environmental stability.

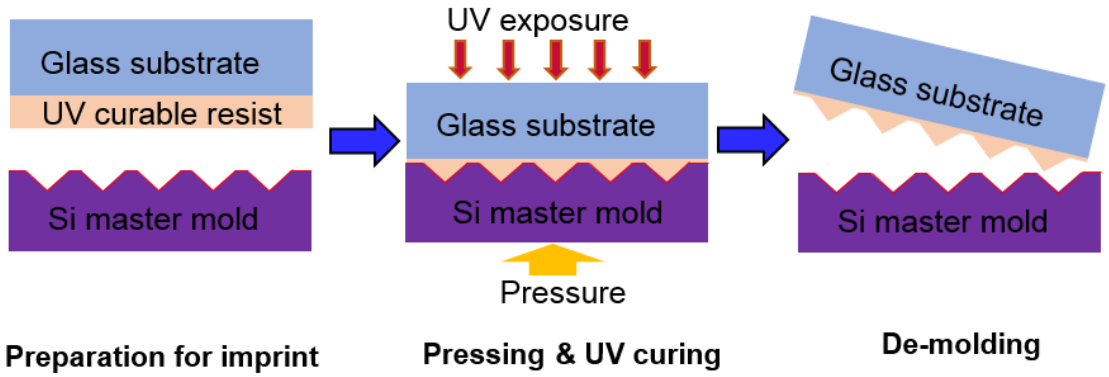

Figure 4.6: The schematic diagram of the first imprint process steps to replicate the upright nanopyramid structures.

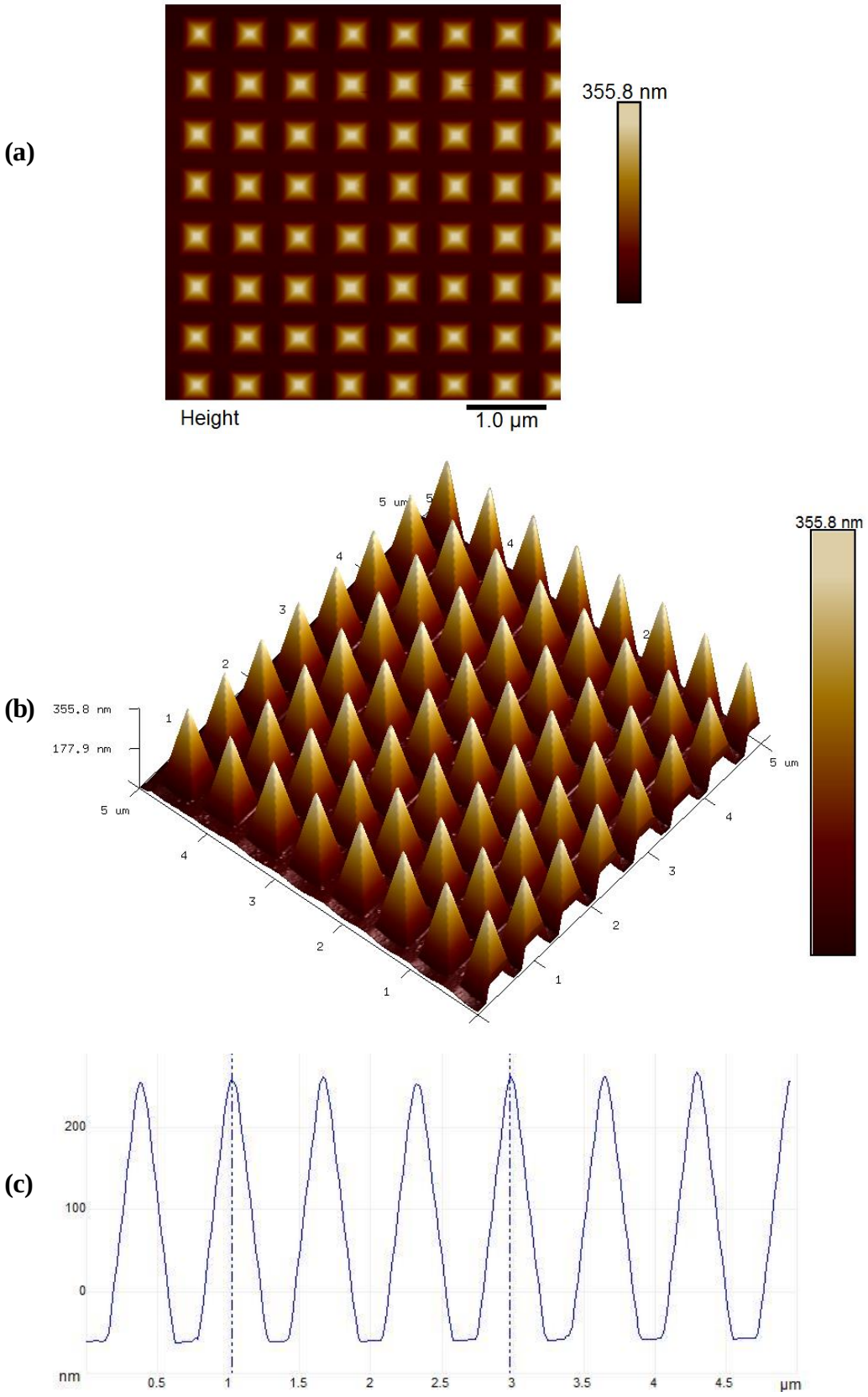

Figure 4.7: AFM images of inverted shapes of the master mold replica formed on UV transparent OrmoStamp resist coated glass substrate after the first imprint (a) 2-D view, (b) 3-D view and (c) cross sectional traces.

Figure 4.7 (a) and (b) show the 2-D and 3-D AFM images of the periodic upright nanopyramid formed onto the OrmoStamp resist coated glass substrate as the result of first imprint process. It can be seen that the upright nanopyramid structures with periodic features in the order of 500nm and smooth surfaces have been precisely replicated onto the OrmoStamp resist coated glass substrate. The AFM images for the master mold and imprinted sample were compared and dimensions measured from randomly selected areas but with the same scanned area of 5 μm × 5 μm.

Figures 4.5(c) and 4.7(c) reveal that no significant differences can be found between the master mold and inverted shape of master mold replica. These results further confirm that excellent fidelity periodic upright nanopyramid structures can be achieved by UV-NIL imprinting. This high fidelity replication offers high flexibility in designing new light trapping schemes for solar cells applications. The UV curable resist can be incorporated into a range of solar cells configuration because of its low optical absorption [93, 152, 153]. Therefore, the replicated periodic upright nanopyramid structures on the OrmoStamp resist coated glass substrate can be utilized as light trapping and self-cleaning functions in different types of solar cells. In this thesis, the effect of upright nanopyramid structured cover glass with light harvesting and self-cleaning functions on the device performance of monocrystalline Si and polycrystalline Si solar cells are presented in Chapter 5.

This imprinting process can be continued, and the inverted nanopyramid structures can be created from the upright nanopyramid structured glass as a mold for direct 3D imprint process. It should be noted that there is no direct technique for forming periodic and ordered upright pyramid structures on crystalline silicon because of the limitation imposed by the crystal orientation.

4.3.2 Imprint – Inverted nanopyramid structures replication

Figure 4.8 shows the schematic diagram of the second imprint process steps to create the inverted nanopyramid structures into UV curable resist coated glass substrate. In this imprinting process, the replicated upright nanopyramid structure on UV curable resist coated glass substrate was used as a mold in order to form the inverted nanopyramid structures on UV curable resist coated glass substrate. A very thin F_{13}-TCS SAM was used as an anti-adhesive layer on the upright nanopyramid structured glass substrate. It was deposited on a mold surface in a vacuum desiccator at room temperature as described in section 4.2.2.

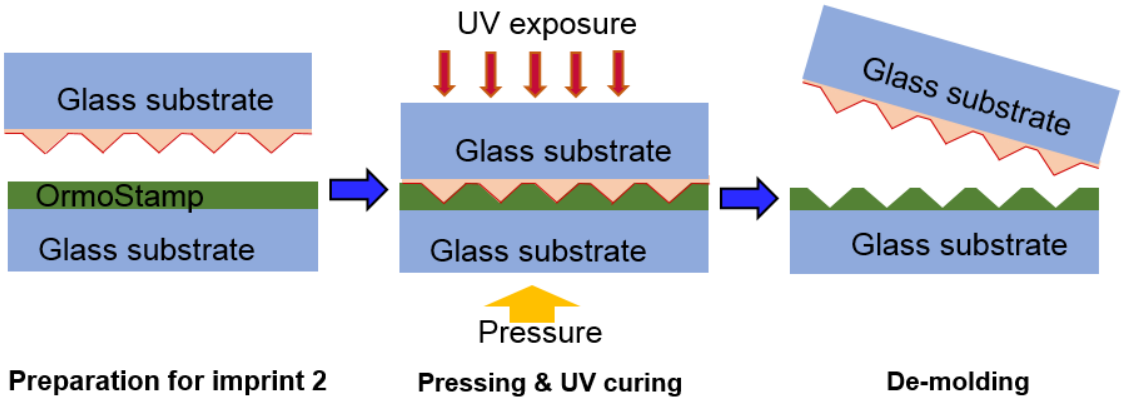

Figure 4.8: The schematic diagram of the second imprint process steps to replicate the inverted nanopyramid structures.

The OrmoStamp coated substrate was prepared as explained in section 4.2.3 and was placed up at the bottom of the imprint tool. The upright nanopyramid structured glass substrate coated with F_{13}-TCS SAM was placed face down and manually aligned on the top of the OrmoStamp coated substrate. The inverted nanopyramid structures were replicated on the OrmoStamp coated substrate by the same UV imprinting method as described in the first imprinting process using upright nanopyramid patterned glass substrate as a master mold.

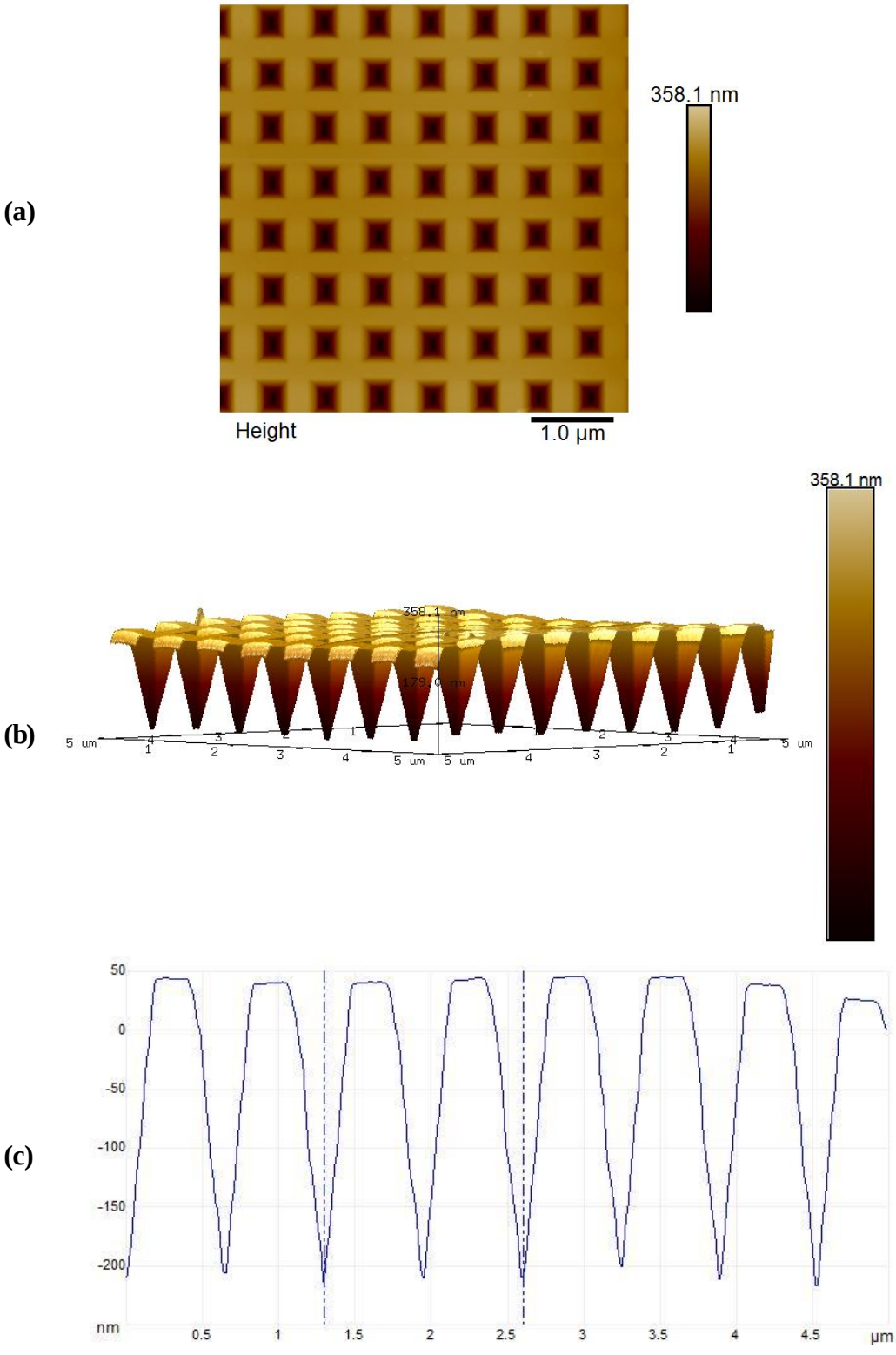

Figure 4.9: AFM images of inverted nanopyramid structures formed on UV transparent OrmoStamp resist coated glass substrate after the second imprint (a) 2-D view, (b) 3-D view and (c) cross sectional traces.

In order to determine the accuracy of the replication by the nanoimprint process, AFM images of the master mold and replicated substrates were taken. Figure 4.9 (a) and (b) show the 2-D and 3-D AFM images of the periodic inverted nanopyramid structures formed onto the OrmoStamp resist coated glass substrate as the result of second imprint process with a scanned area of 5 μm × 5 μm. It can be seen that the inverted nanopyramid structures with periodic features and smooth surfaces have been precisely reproduced onto the OrmoStamp resist coated glass substrate with high fidelity. Figure 4.9(c) illustrates the AFM image cross-sectional traces of the replicated inverted nanopyramid structures on resist coated substrate. It shows that the replication from the upright nanopyramid on resist coated substrate is very similar and high accuracy compared to original Si master mold as illustrated in Figure 4.5(c).

The inverted nanopyramid structures, which is utilized for light trapping in solar cells, was transferred to the resist coated substrate by the nanoimprint process without any structural losses. The inverted nanopyramid structures by nanoimprint process can be used in different approaches to enhance the solar cell performances. In this thesis, the inverted nanopyramid structures were fabricated on the front side of the monocrystalline Si and polycrystalline Si solar cells by nanoimprint process, respectively. The effect of the inverted nanopyramid structures for improving the performances of monocrystalline Si solar cells and polycrystalline Si solar cells are discussed in Chapter 6.

4.4 Summary

In this chapter, the development of the ultraviolet nanoimprint lithography (UV-NIL) and nanoimprint processes for the replication of upright nanopyramid and inverted nanopyramid structures were presented. The periodic inverted nanopyramid structure on a silicon substrate was used as a master mold substrate for the imprint process. The periodic inverted nanopyramid structures were fabricated on a Si substrate by LIL and subsequent pattern transfer by combined reactive ion etching and KOH wet etching. The anti-sticking layer for the mold and substrate preparation for imprint process were discussed.

In the first nanoimprint process, the upright nanopyramid structures were fabricated on the OrmoStamp coated glass substrate using Si master mold with high fidelity. The upright nanopyramid structured glass substrate was used as cover glass for solar cells application and as a mold for the second imprint process. The effect of the upright nanopyramid structured cover glass for solar cell applications is discussed in Chapter 5.

In the second nanoimprint process, the inverted nanopyramid structures were fabricated on the OrmoStamp coated substrate using the upright nanopyramid structured glass substrate as a mold. The replicated inverted nanopyramid structure on resist coated substrate was faithfully resolved with the high accuracy compared to original Si master mold. The inverted nanopyramid structures replicated at the front of the solar cells can enhance the solar cells efficiencies by acting as a light harvesting and anti-reflective coating, which is demonstrated in Chapter 6.

There are some issues which came up during the development of the UV-NIL process. The adhesion between the resist and substrate were critical when no adhesion promoter was added to the substrate before to the resist spin coating. In order to resolve

the adhesion problem between the resist and substrate, the OrmoPrime08 from micro resist technology was used to increasing the adhesion of the OrmoStamp resist to substrate. It was observed that the F_{13}-TCS SAM coated master mold was used several times in the imprint process, whereas imprint process was not successful without F_{13}-TCS SAM coating due to the sticking and particles contamination. SAM coating improves the imprint qualities and also increases the mold lifetime significantly by preventing surface damage and contamination. It was also observed that the adhesion between the mold and replica was larger when higher exposure dose was used during the imprint process. This effect may be correlated to higher shrinkage of the resist when exposed to higher UV exposure dose. In this case, it was preferred to maintain constant UV exposure dose (1000 $mJcm^{-2}$) prior to the demolding and additional UV exposure and hard baking were done after demolding.

Chapter 5 Upright nanopyramid structured cover glass with light harvesting and self-cleaning effects for solar cells

The effect of upright nanopyramid (UNP) structured cover glass with light harvesting and self-cleaning functions on the device performance of monocrystalline Si solar cells and commercially made polycrystalline Si solar cells are presented in this chapter. The UNP structures were fabricated on the surface of the glass substrate by simple, high throughput and low-cost UV nanoimprint lithography using Si master mold with inverted nanopyramid (INP) structures. The diffuse transmittance and haze ratio value were significantly increased for UNP patterned glass, especially, in the wavelength range 300-600 nm compared to the bare glass, which implies that antireflection effect and strong light scattering due to the UNP structures. By replacing a bare cover glass with UNP patterned glass, the power conversion efficiency of the monocrystalline Si solar cell and commercially made polycrystalline Si solar cell were substantially enhanced by 10.888% and 8.216%, respectively. That was mainly due to the increased oblique scattering and prolonged the optical path length by the upright nanopyramid structures. In addition, the fluorinated UNP structured cover glass exhibited a hydrophobic surface with a water contact angle (θ_{CA}) of ~132° and excellent self-cleaning function when tested with dust particles by rolling down water droplets. The self-cleaning properties is superior as compared to the bare cover glass, which has a typical contact angle of θ_{CA} ~ 36°.

5.1 Introduction

Solar cell modules are installed in an outdoor environment for the vast majority of applications. Therefore, whatever the type of solar cell, glass is commonly incorporated as an encapsulation for preventing damage from dust, moisture and external shock [154, 155]. However, some of the incident light onto a solar cell might be lost through optical reflection due to the refractive index mismatch between the air and cover glass and through scattering or absorption by contaminants [17, 156]. The amount of the incident light reaching the solar cell could be enhanced by incorporating antireflective and light scattering nanostructures at the cover glass surface. Moreover, it is also demonstrated that the nanostructured cover glass has self-cleaning property so as to efficiently maintain the performances of solar cells in harsh environments.

In order to enhance the efficiency of the solar cells, the cover glass that combining antireflective and scattering effects with self-cleaning have been studied by several research groups [6, 14, 157-159]. The oblique light scattering effect improves the light harvesting of the solar cells as a result of prolonged optical path length within the solar cells and thus, increasing the conversion efficiency [12, 160]. There are several methods for obtaining nanoscale structures including electron beam lithography [46], focused ion beam lithography (FIB) [104], laser interference lithography (LIL) [26, 105], nanoimprint lithography (NIL)[92, 93, 152, 161, 162], nanosphere lithography (NSL) [108] and Block copolymer lithography (BCPL) [109]. Among them, the UV nanoimprint lithography (UV- NIL) is emerging as powerful technique for fabricating nanoscale structures on large surfaces with simple, high throughput, low cost and high resolution manufacturing capability [80].

In this chapter, we demonstrate the use of UNP structured cover glass with efficient light harvesting and self-cleaning effects. The UNP was applied for encapsulating a

monocrystalline and a polycrystalline Si solar cells to improve the power conversion efficiency and also to act as a hydrophobic surface. The properties of the UNP surfaces were compared to the encapsulated monocrystalline and polycrystalline Si solar cells with the bare glass. The UNP structured glass was fabricated by UV nanoimprint lithography using Si master mold with INP structures as discussed in Chapter 4. For the UNP structured cover glass, the surface wetting behavior and optical properties were investigated. The effects of UNP structured cover glass on the device characteristics of monocrystalline and polycrystalline Si solar cells were also characterized.

5.2 Experimental details

5.2.1 Fabrication of upright nanopyramid structures on glass substrate

The UV nanoimprint lithography process was used for the fabrication of UNP structures on a glass substrate. The process flow of the imprint process is shown in Figure 5.1.

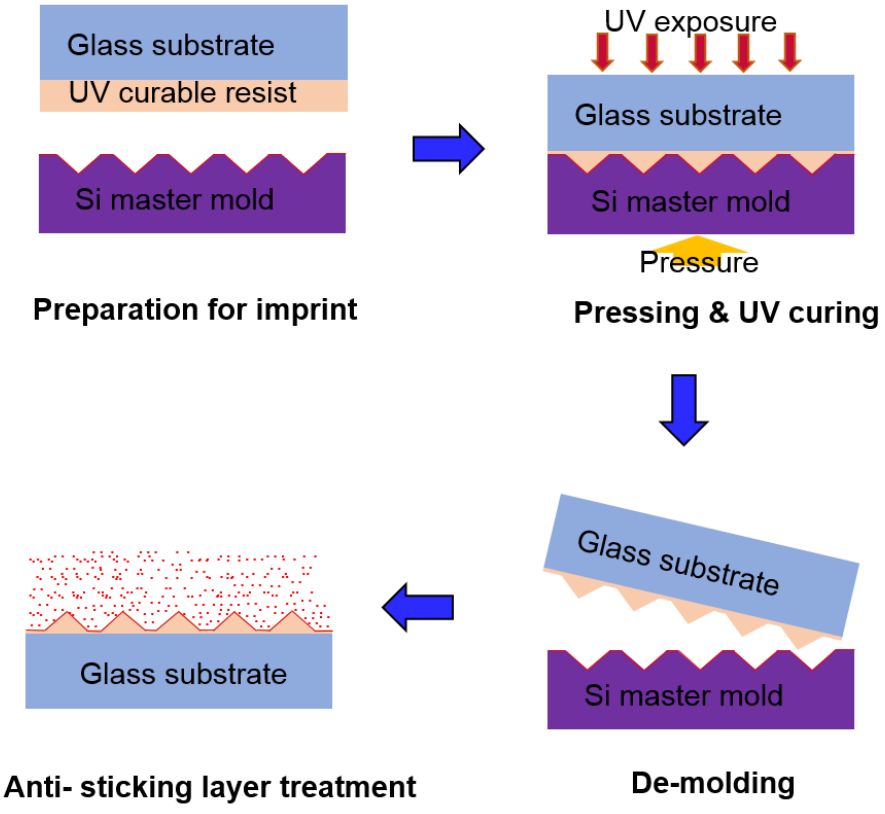

Figure 5.1: The schematic diagram of overall imprint process.

The periodic INP structure master Si mold was fabricated by laser interference lithography and subsequent pattern transfer by combined reactive ion etching and KOH wet etching. Additional details on the fabrication process of master mold can be found in Chapter 3. A UV curable resist (OrmoStamp) was spun onto a glass substrate and then the substrate was placed over the Si mold inside the imprint tool. An imprint pressure of up to 4 mbar was applied to transfer the patterns with a UV light illumination of wavelength 365 nm.The UNP pattern was successfully replicated from the Si mold to the glass plate with high fidelity. After the UV nanoimprint process, F_{13}-TCS based SAM was coated onto the upright nanopyramid patterned glass plate in order to increase the hydrophobicity of the surface. More details of the UV nanoimprint process parameters and the tools which were used can be found in Chapter 4.

5.2.2 Solar cell fabrication

In order to measure the effect of the UNP structures, the UNP patterned glass, and the bare glass substrates were used as a cover glass on a monocrystalline Si solar cell and commercially made polycrystalline Si solar cell provided by Hanregy of China. In this study, monocrystalline Si solar cells were fabricated by the process shown in the schematic Figure 5.2.

A single-side-polished, Czochralski (CZ) grown, 350μm thick, Boron doped p-type silicon wafer with <100> crystal orientation and resistivity of 0.5-1.0 Ωcm was used as the substrate. After standard RCA cleaning and 1:10 dilute HF dipping, a 200 nm thermal oxide was grown onto the wafer using quartz tube furnace and dry/wet oxidation was done at 1000°C. The 10mm × 10mm individual cells were defined by photolithography followed by buffered HF etching to remove the oxide and isolate the individual cells by opening windows in the oxide. The backside of the substrate was doped with boron dopant

(B202 form Filmtronics) to produce back surface field effect. The emitter junction was formed by spin-on phosphorus doping processes using P509 Dopant from Filmtronics. The diffusion was performed in a quartz tube furnace at 950 °C for 30 min in a 20% O_2 and 80% N_2 environment. Diluted 10% HF solution was used to remove the phosphosilicate glass (PSG) on the wafer surface. The 300 nm thick aluminum front contact grid and back contact were formed by DC sputtering and metal lift-off. In creating of the top contact, top contact patterns were defined by photolithography before the metal deposition

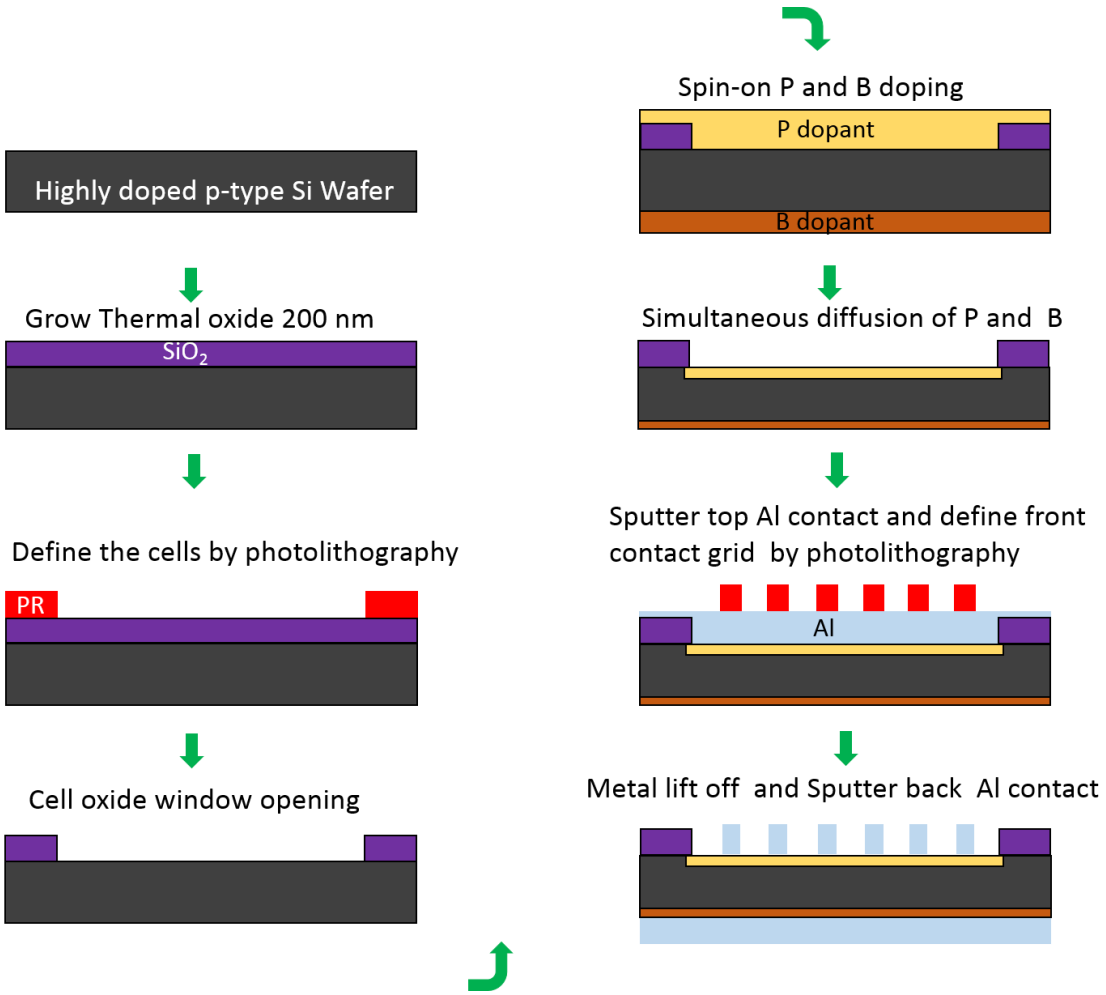

Figure 5.2: Schematic representation of monocrystalline Si solar cell fabrication process.

5.2.3 Characterization

The surface morphologies of the fabricated samples were observed by using scanning electron microscope (SEM) (JEOL 7000F FE-SEM) and atomic force microscope (AFM, DI3000). The total and diffuse transmittance of UNP patterned glass and the bare glass were measured using a UV-visible spectrophotometer at room temperature, with an integrating sphere over the wavelength range of 300-1200 nm. The contact angle of water droplets on the UNP patterned glass, and the bare glass was measured using a contact angle goniometer with Edmund Scientific Camera. The setup used for the measurements are shown in Figure 5.3. The current density-voltage characteristics were measured using a Keithley 2400 source measure unit and a solar simulator (ABET Sun3000) with AM 1.5G filter under illumination of 1 sun. The external quantum efficiency was also performed using tungsten –halogen lamp in combination with a monochromator (CS130 1/8m).

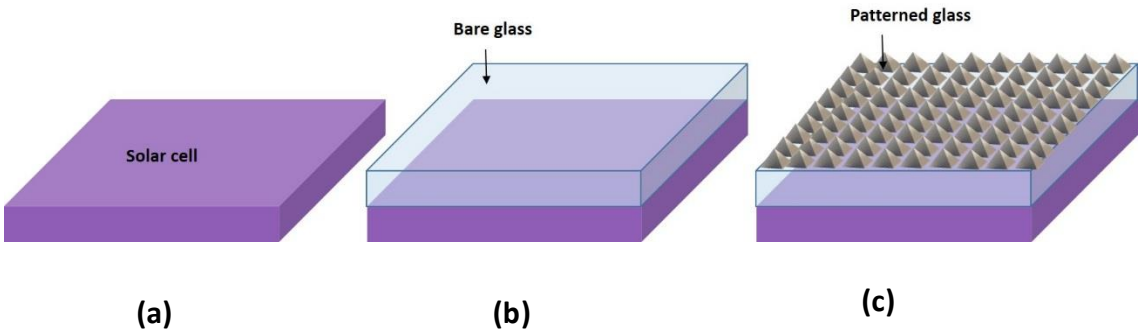

Figure 5.3: The setup used for comparison measurements (a) Si solar cells without cover glass (b) with a bare cover glass and (c) with a UNP patterned glass.

5.3 Results and discussion

5.3.1 Morphology analysis and optical properties

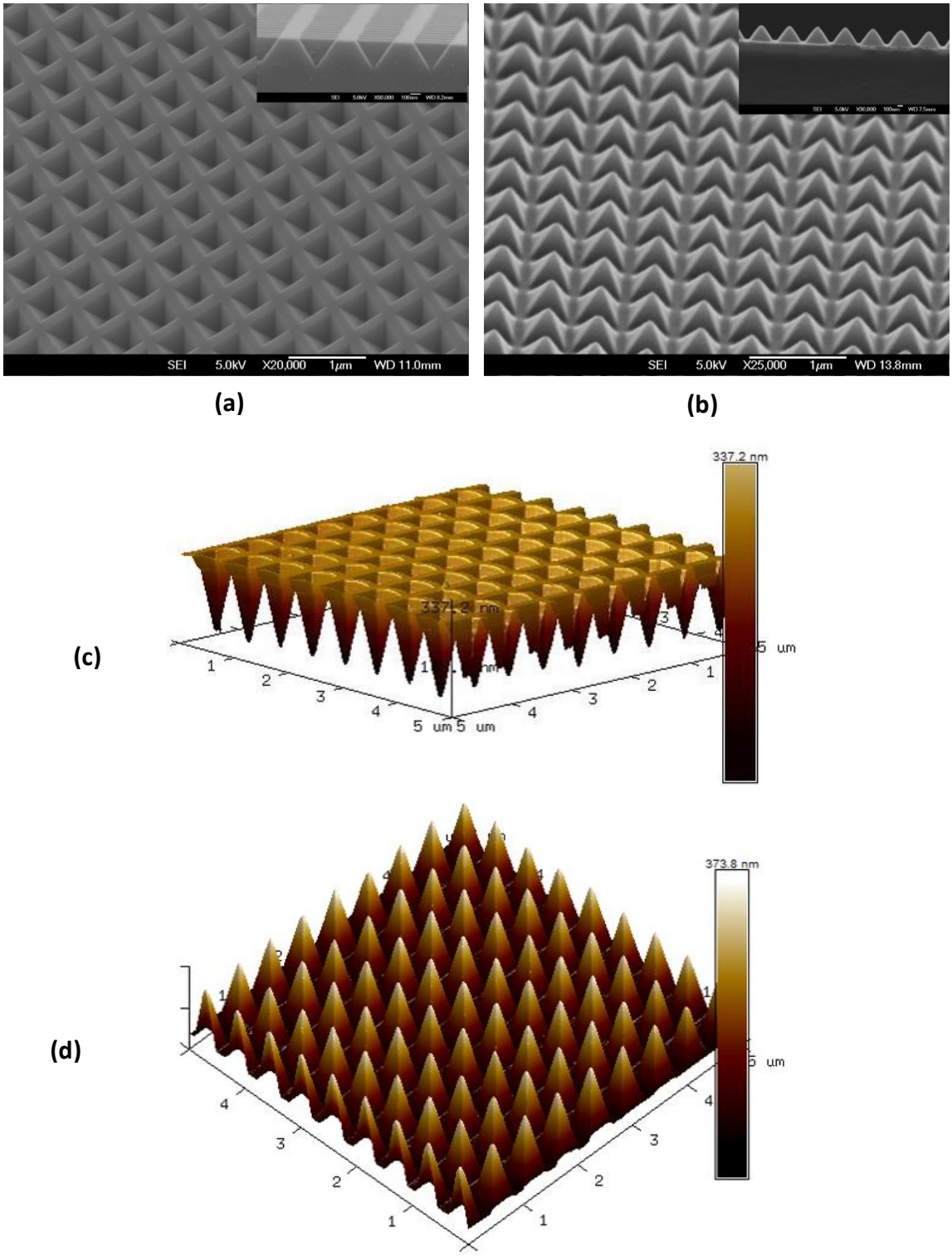

Figure 5.4: 30°-tilted view SEM images of (a) INP Si master mold and (b) UNP structured on glass and the inset images are the cross-sectional view of SEM images. 3D AFM images of (c) INP Si master mold and (d) UNP structured on glass.

Figure 5.4(a) and (c) present the SEM images and AFM image of the Si master mold with INP structures, respectively. Figure 5.4(b) and (d) show the SEM images and AFM image of the UNP structured glass from the master mold, respectively. As shown in Figure 5.4(a), the INP structures were well formed on the surface of the Si master mold by using laser interference lithography and subsequent pattern transfer by combined reactive ion etching and KOH wet etching. By using UV nanoimprint lithography, the INP patterns on the Si master mold were transferred onto the UV curable resist coated glass substrate without any distortion and deformation, as shown in Figure 5.4(b). This was also be confirmed in the AFM image of Figure 5.4(d). From Figure 5.4, the 450 nm wide and 310 nm high UNP structures with 125 nm separation were replicated uniformly over the large area of 10x10 mm after the imprint process.

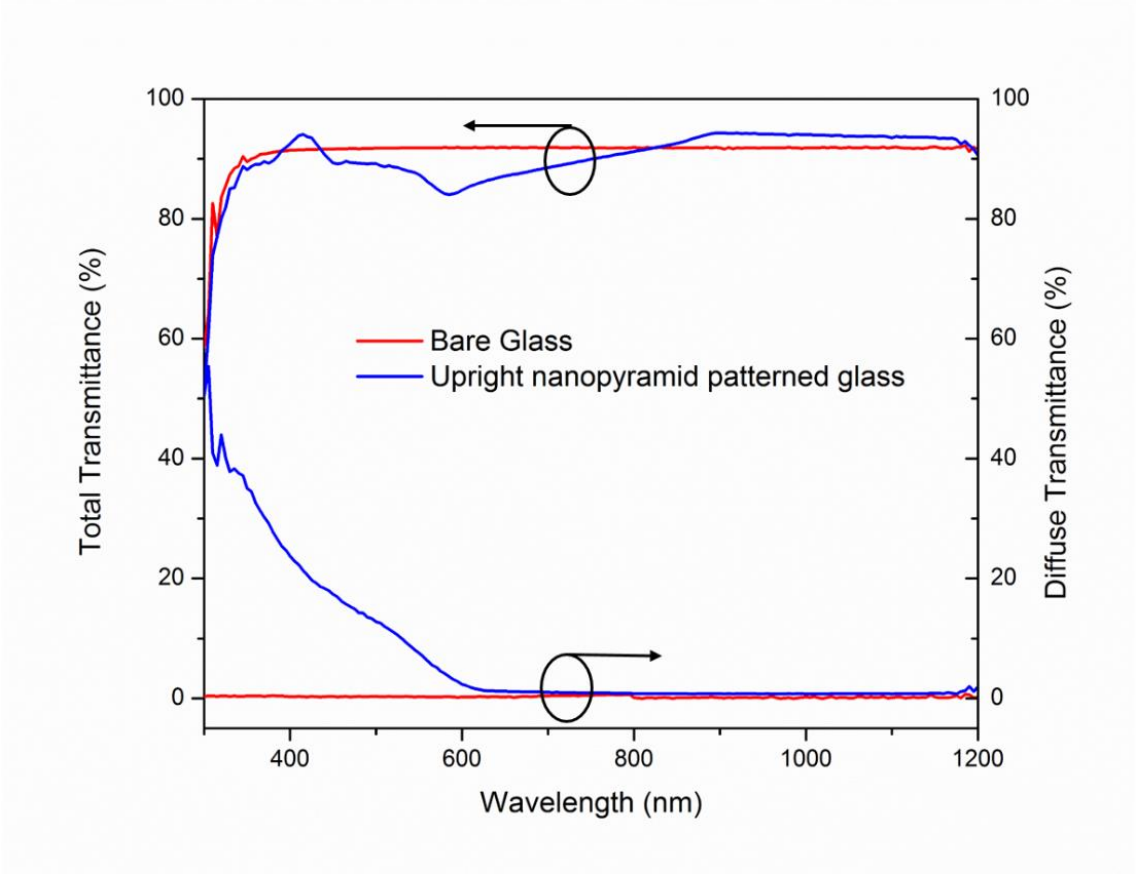

Figure 5.5: Measured total and diffuse transmittance spectra of the bare glass and the UNP patterned glass as a function of wavelength.

Figure 5.5 illustrates the comparison between the total and diffuse transmittance of the glass substrates with and without UNP patterns, which were measured using an integrating sphere with the incoming light entered from the patterned glass substrate. As can be seen in Figure 5.5, the total transmittance of the UNP patterned glass was slightly lower than that of the bare glass in the wavelength range of 450-800 nm, which may be caused by the diffraction losses due to the higher order diffracted waves [163-165]. However, the diffuse transmittance of the UNP patterned glass was increased up to 24% in the visible wavelength region due to higher orders of diffracted waves in the transmission, while the bare glass substrate shows almost no diffuse transmittance over a wide wavelength range as shown in Figure 5.5.

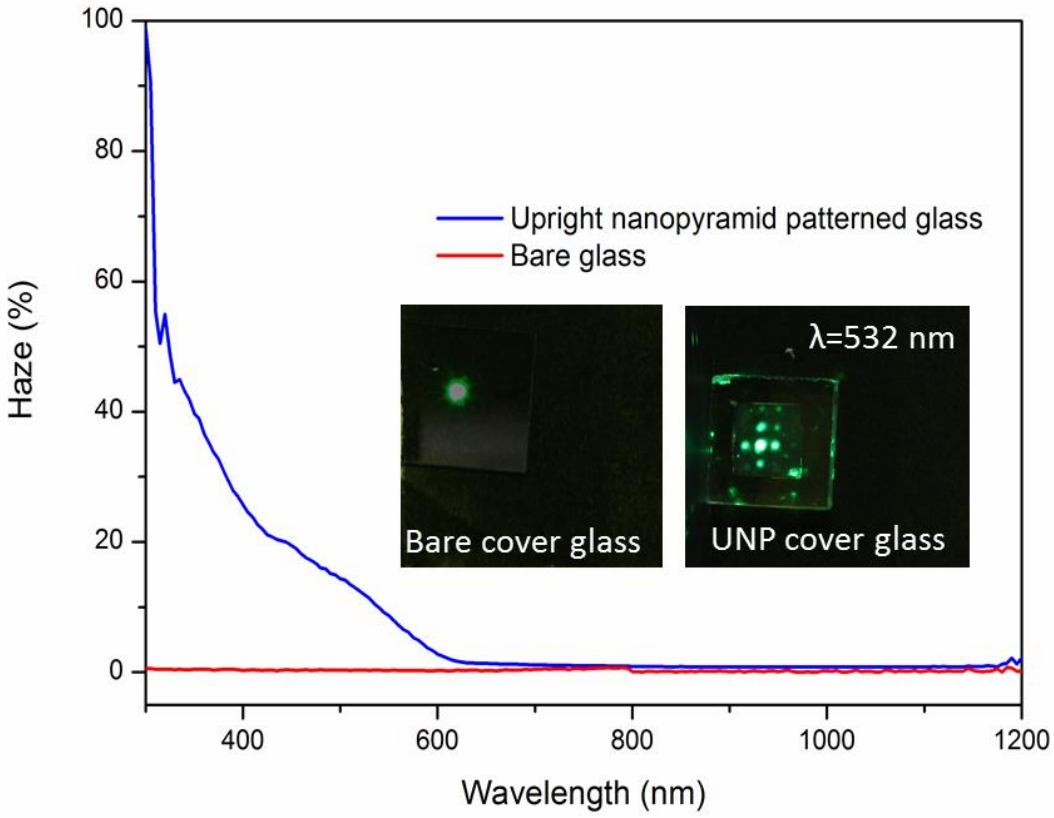

Figure 5.6: The optical haze spectra of the bare glass and the UNP patterned glass as a function of wavelength. Photographs of diffracted light patterns of the corresponding samples obtained from the green diode laser with λ=532 nm are also shown in the inset.

The haze value (H), which is defined by the ratio of the diffuse transmittance (T_d) to the total transmittance (T_t), *i.e.*, $H = T_d / T_t$, which indicates the light scattering properties of the samples. When the incident light passed through the bare cover glass, the H value was close to zero as shown in Figure 5.6. In contrast, the H value was significantly increased for patterned glass, especially, in the wavelength range 300-600 nm, which implies that strong light scattering by UNP structured glass. This light scattering behavior can also be confirmed in the insets of Figure 5.6. For the bare cover glass, there is almost no light diffraction, whereas the UNP patterned glass shows high order diffraction patterns using a green diode laser at a wavelength of 532 nm. This scattering effect will result in changes in the propagation direction of light from normal to the oblique incidence in the solar cell. As a result, the optical path length of the incident light was elongated and hence the light absorption in the active layer was also improved by the patterned glass. Indeed, the high haze optical property due to the light scattering effect would positively enhance the power conversion efficiency of the solar cells with the UNP patterned glass compared to the bare cover glass [166-168].

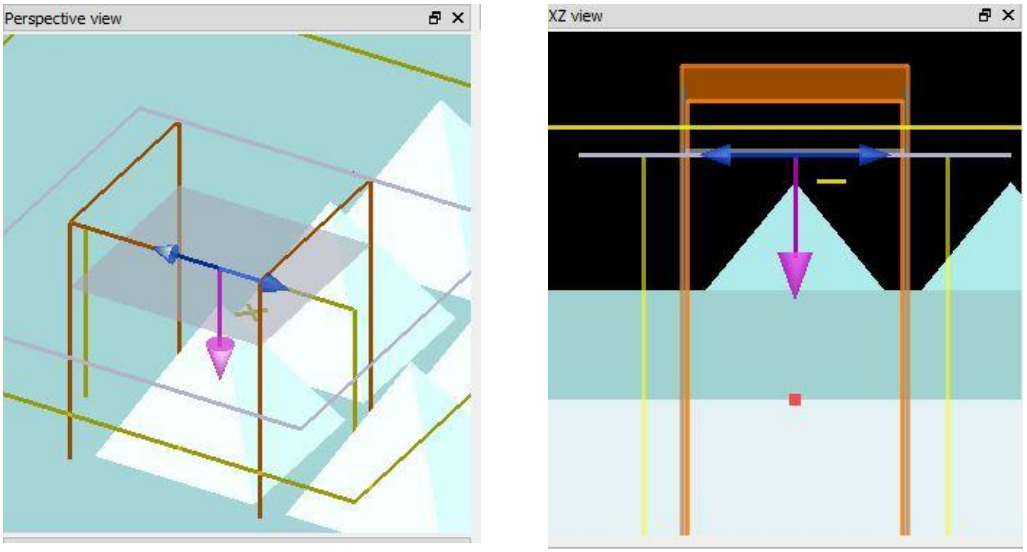

(a) **(b)**

Figure 5.7: FDTD simulation model layout of the UNP structured glass substrate (a) Perspective view and (b) XZ view.

Numerical simulations by using the finite –difference-time –domain (FDTD) method by Lumerical solutions Inc. were performed to explain how the incoming light couples with and without UNP structure. Figure 5.7 shows the FDTD simulation model layout of the UNP structured glass substrate perspective view and XZ view. Perfectly matched layers (PML) and periodic boundary conditions were used in the perpendicular and horizontal directions.

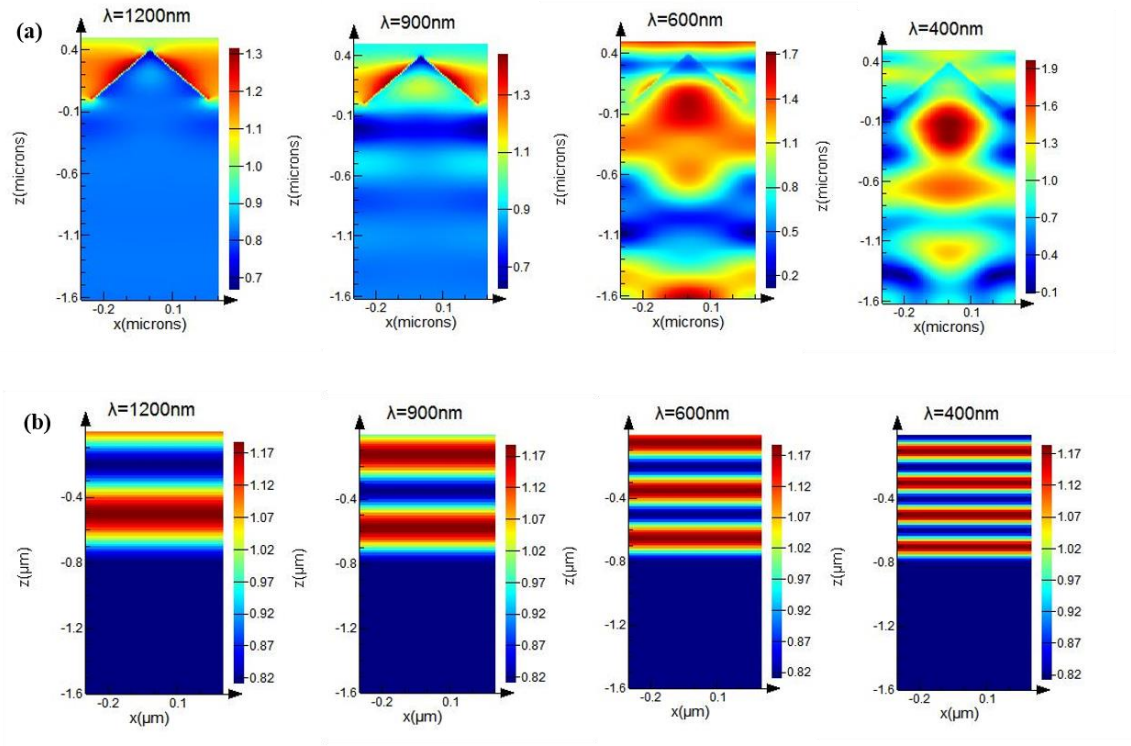

Figure 5.8: The cross-sectional electric field distribution profiles at different wavelength by FDTD analysis (a) UNP structured glass with period of 600nm, size of 500nm and height of 400nm and (b) bare glass.

The cross-sectional electric field distributions at different wavelength were obtained for the incident light propagating from air to the glass substrate with and without UNP structure as illustrated in Figure 5.8. As shown in Figure 5.8, UNP structures exhibit strong light interference patterns with wide angular range, especially in the wavelength below 600 nm and allow the light propagation interface between the air and the glass

while there are no scattering light for bare cover glass. From these results, it is demonstrated that UNP structured glass enables to enhance the diffuse transmittance of the cover glass and thus it can lead to the PCE enhancement of encapsulated solar cells due to the enhanced light harvesting in the absorption layer of the solar cells caused by strong light scattering and antireflection effects[168, 169].

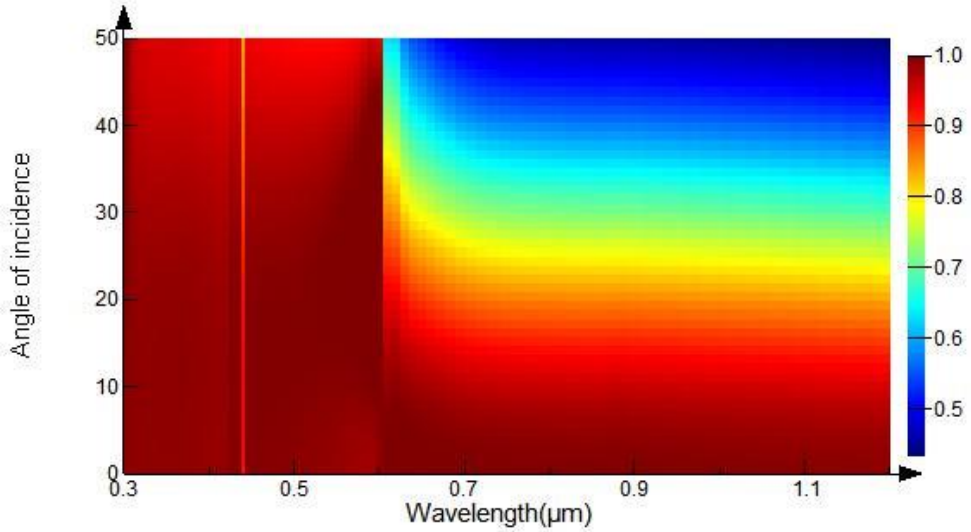

Figure 5.9: Contour plot of simulated transmittance spectra of the UNP structured glass as a function of angle of incidence (0-50°) over the broad wavelength range.

Figure 5.9 shows the contour plot of simulated transmittance spectra of the UNP structured glass as a function of angle of incidence (0-50°) over the broad wavelength range. It shows that for the incident angle no bigger than the 15°, the average transmittance is still as high as the case at normal incidence. However, when the angle is up to 50°, the transmittance is rapidly decreased, especially in the long wavelength range 600 nm – 1200 nm. This is because the gradient refractive index profile from air to glass substrate changes considerably from the case at normal incidence.

5.3.2 Device performance

In order to verify the effect of the periodic UNP patterns, the patterned glass and the bare glass substrate were used as a cover glass on a monocrystalline Si solar cell and commercially made polycrystalline Si solar cell. Figure 5.10shows the current density – voltage characteristics of encapsulated monocrystalline Si solar cell (Figure 5.10(a)) and polycrystalline Si solar cell (Figure 5.10(b)) with and without UNP patterned cover glass. The measured monocrystalline Si solar cell and polycrystalline Si solar cell performances are summarized in Table 5.1 and 5.2, respectively.

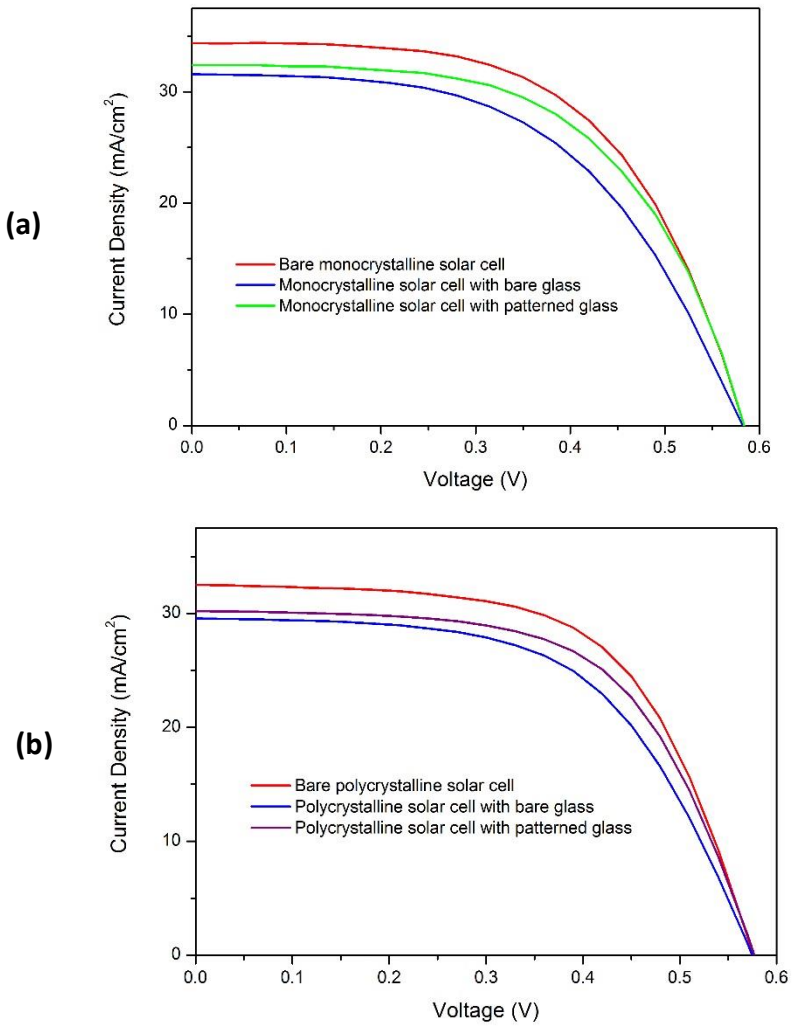

Figure 5.10: Current density–voltage characteristics of encapsulated (a) monocrystalline Si solar cell and (b) polycrystalline Si solar cell with and without the UNP patterned cover glass and bare cover glass.

There was no significant change in the open circuit voltage (V_{OC}), but a significant enhancement in the short-circuit current density (J_{SC}) was observed as expected. The fill factor (FF) of monocrystalline and polycrystalline Si solar cells were slightly enhanced from 55.226% to 59.756% and 57.781% to 61.195 % with UNP patterned cover glass, respectively. Such improvement in FF could be attributed to enhanced density of free carriers [170], induced by the increased number of photons entering the active layer of the solar cell and reducing the effective series resistance.

Table 5.1 Device characteristics of encapsulated monocrystalline Si solar cells with and without the UNP patterned cover glass and the bare cover glass.

Monocrystalline Si solar cells	*V_{OC} (V)*	*J_{SC} ($mAcm^{-2}$)*	*FF (%)*	*PCE (%)*
Without cover glass	0.580	34.376	59.815	11.926
Bare cover glass	0.580	31.598	55.226	10.121
UNP patterned cover glass	0.580	32.390	59.756	11.223

Table 5.2 Device characteristics of encapsulated polycrystalline Si solar cells with and without the UNP patterned cover glass and the bare cover glass.

Polycrystalline Si solar cells	*V_{OC} (V)*	*J_{SC} ($mAcm^{-2}$)*	*FF (%)*	*PCE (%)*
Without cover glass	0.575	32.512	61.273	11.455
Bare cover glass	0.575	29.563	57.781	9.822
UNP patterned cover glass	0.575	30.207	61.195	10.629

The J_{SC} values of the monocrystalline and polycrystalline Si solar cells without cover glass were 34.376 $mAcm^{-2}$ and 32.512 $mAcm^{-2}$, which were decreased to 31.598 $mAcm^{-}$

^{2} and 29.563 mAcm^{-2} with a bare cover glass, respectively. This reduction in J_{SC} indicates that the cover glass reduces the number of photon entering the active layer of the solar cell through reflection and absorption processes. However, by replacing the bare glass with UNP patterned cover glass, J_{SC} values were increased to 32.390 mAcm^{-2} and 30.207 mAcm^{-2} for encapsulated monocrystalline Si solar cell and polycrystalline Si solar cell, respectively. As a result, the use of the UNP patterned glass as a cover glass, the power conversion efficiency (PCE) of encapsulated monocrystalline Si solar cell and polycrystalline Si solar cell were significantly enhanced by 10.888% and 8.216% compared to the encapsulated monocrystalline Si solar cell and polycrystalline solar cell with bare cover glass, respectively. This enhancement is mainly due to the strong light scattering effect via the UNP structures.

As shown in Figure 5.11, the solar cells with UNP patterned cover glass exhibited improved EQE values compared to the solar cells with the bare cover glass, particularly in the wavelength region 400-600 nm, due to the increased photogenerated carriers caused by its higher diffuse transmittance and haze properties. This result was precisely matched with the optical haze value result shown in Figure 5.6. From these results, the periodic UNP patterned glass offers a better-graded index medium to the incident light, compare to the bare glass, which can reduce the Fresnel reflectance and scatter more incident light into the solar cells and prolong the optical path length, therefore improving the light trapping and increasing the overall conversion efficiency.

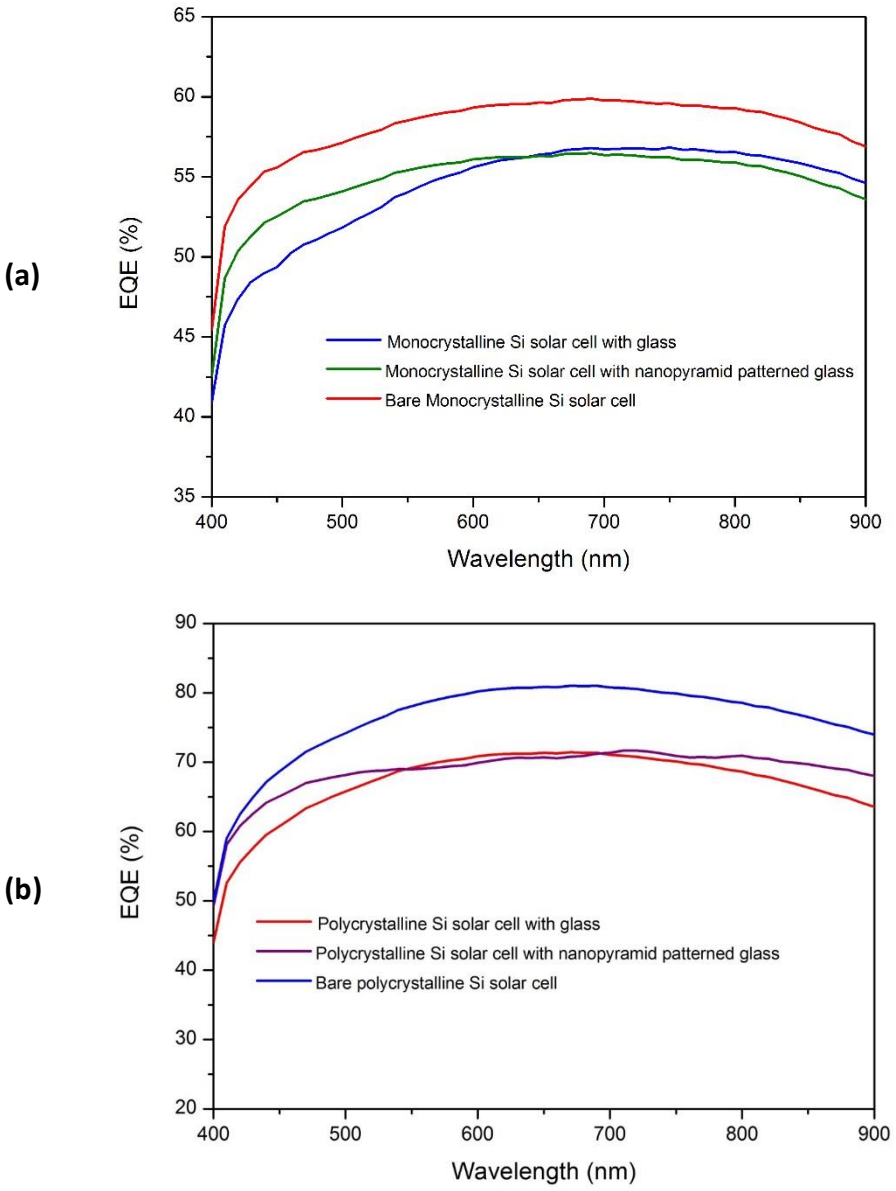

Figure 5.11: EQE spectra of of encapsulated (a) monocrystalline Si solar cell and (b) polycrystalline Si solar cell with and without the UNP patterned cover glass and bare cover glass.

5.3.3 Surface wettability and self-cleaning behaviors

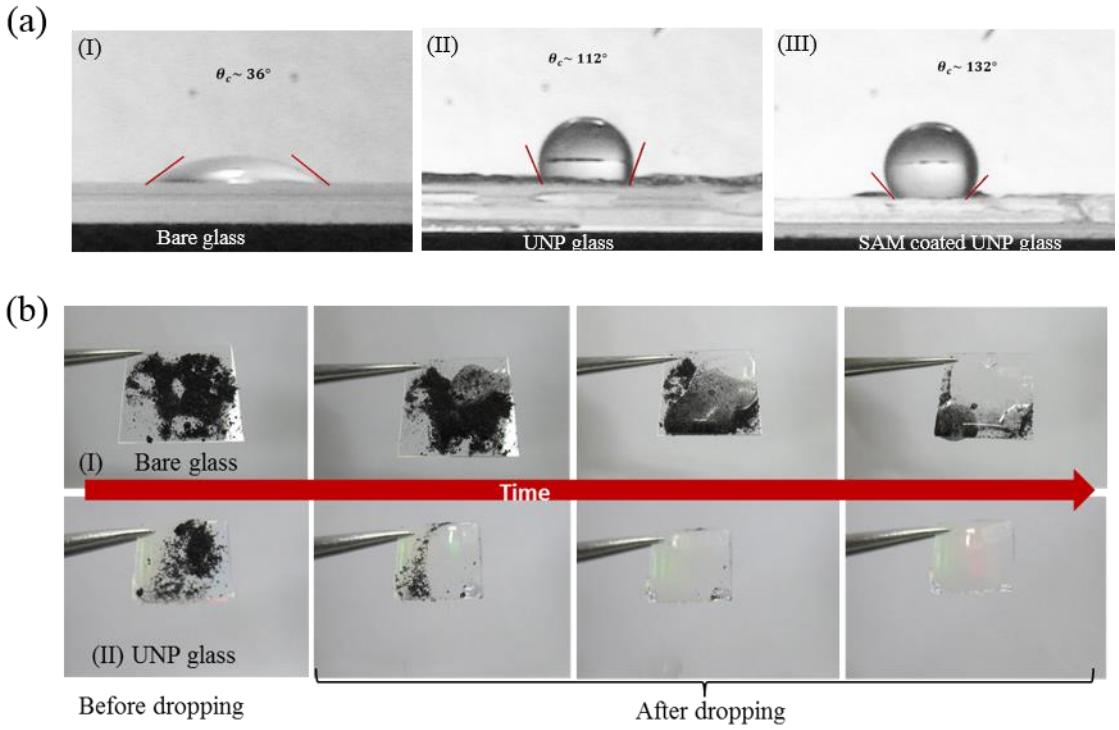

Figure 5.12: Photographs of (a) a water droplets on (I) bare glass, (II) UNP glass and (II) SAM-coated UNP glass and (b) sequential photographs of self-cleaning process for (I) the bare glass and (II) UNP glass. The θ_{CA} is the water contact angle.

In real outdoor environments, the cover glass layer of the solar cell can be easily contaminated by dust particles, which interfere with the incident light into the cell absorption layer and thus reducing the solar cells performance. Therefore, the antireflection layer with a self-cleaning function at the top surface of the cover glass layer is necessary to maintain the solar cell performance[96, 171]. The water wetting behaviors of the samples with different morphologies were investigated. Fig. 5.12 shows (a) the photographs of a water droplet on (I) the bare glass, (II) UNP structured glass and (III)

SAM-coated UNP structured glass and (b) sequential photographs of water droplet self-cleaning process for (I) the bare cover glass and (II) UNP structured glass.

As shown in Figure 5.12(a), the bare glass exhibited a hydrophilic surface with a water contact angle (θ_{CA}) of ~ 36° while UNP patterned glass showed a hydrophobic behavior with a θ_{CA} value of ~ 112°. This hydrophobic behavior is attributed to the increased surface roughness of the UNP patterned glass, which can be explained by the Cassie–Baxter equation [172]. Moreover, F_{13}-TCS based SAM was coated onto the UNP patterned glass in order to enhance its hydrophobic surfaces. In this case, the contact angle of the SAM-coated UNP glass was increased to 132° as shown in Figure 5.12(a). These contact angle (θ_{CA}) values are comparatively lower than those reported with superhydrophobicity (i.e., $\theta_{CA} > 150°$) in previous studies [173-176]. However, it can be seen that the black dust particles on the surface of UNP patterned glass were clearly removed by the rolling down water droplets without any remaining dust particles or water droplets at the surface, as shown in Figure 5.12(b). In contrast, the black dust particles on the bare glass were moved downwards with the rolling down water droplets and thus the dust particles partially remained with water droplets at the edge of the glass. As a result, this UNP patterned cover glass with light harvesting and self-cleaning properties would enhance the practical feasibility of solar cells in real outdoor environments.

5.4 Summary

The UNP structures with antireflective and hydrophobic properties were fabricated on the glass substrate by simple, high throughput and low cost UV nanoimprint lithography using Si master mold with INP structures. INP structures on Si was fabricated by interference lithography and subsequent pattern transfer by combined reactive ion etching and KOH wet etching.

The diffuse transmittance and haze ratio value were significantly increased for UNP patterned glass, especially, in the wavelength range 300-600 nm compared to the bare glass, which indicates that an antireflection function and strong light scattering due to the UNP structures. The use of UNP patterned cover glass as a cover glass, the power conversion efficiency of the encapsulated monocrystalline Si solar cell and polycrystalline Si solar cell were substantially enhanced by 10.888% and 8.216%, respectively. This increase is mainly due to the scattering and prolong the optical path length of the incident photons by the upright nanopyramid structures compared to the reference cells with bare glass. In addition, the fluorinated UNP structured cover glass exhibited larger θ_{CA} ~132° and excellent self-cleaning of dust particles by rolling down water droplets. These results suggest that the UNP structured glass with light harvesting and self-cleaning properties has a considerable potential for various types solar cells and optical display systems in outdoor environments.

Chapter 6 Enhancing the performance of solar cells with inverted nanopyramid structures fabricated by UV nanoimprint lithography

In this chapter, we demonstrate that periodic inverted nanopyramid structures can enhance the power conversion efficiency of monocrystalline Si solar cell and commercially made polycrystalline Si solar cell by minimizing reflections, improving light trapping process in addition to its self-cleaning functionality. The periodic inverted nanopyramid structures were fabricated on monocrystalline Si solar cell and polycrystalline Si solar cell surfaces using a UV nanoimprint lithography. By introducing inverted nanopyramid structures on the front side of the monocrystalline Si and polycrystalline Si solar cells, the power conversion efficiencies were improved by 11.733% and 6.869% compared to identical solar cells without the texturing, respectively. The inverted nanopyramid coating decreased the reflectance and increased the external quantum efficiency over a broad wavelength range. Moreover, the surface of the solar cells exhibited hydrophobic properties due to increased contact angle caused by the nanostructure patterns and the self-assembled monolayer coating. The enhanced hydrophobicity provided the solar cells with an added self-cleaning functionality. These results suggest that the periodic inverted nanopyramid structures has high potential in improving the performance of silicon solar cells and may be applied to different types of solar cells.

6.1 Introduction

Reducing optical losses in the solar cells has always been a key challenge in enhancing the conversion efficiency. In general, efficient light management has been achieved by textured surfaces that enhance the light collection and increasing the effective optical path length of the light within the absorber layer of a solar cell [23]. Various texturing studies have been carried out, such as texturing at the back side [152] or at the front side of a solar cell [177] or pre-texturing the solar cell substrates [178, 179] and a wide variety of light management schemes have been investigated to enhance the power conversion efficiency of a solar cell. The use of nanostructures for improving the light absorption and trapping in solar cells is a more promising method compared with the traditional micro-sized surface texturing [24, 61].

Nanostructures can be fabricated by various techniques including electron beam lithography (EBL) [46], laser interference lithography (LIL) [26], nanoimprint lithography (NIL) [99, 180], nanosphere lithography (NSL) [108] and Block copolymer lithography (BCPL) [109]. Various nanostructures such as nanowires [181-183], nanorods [51], nanocones [47], nanopyramids [105], nanopillars [54] and metal nanostructures such as nanogrooves [39] and nanoparticles arrays [184-186] have been extensively studied. Despite their excellent light trapping properties, texturing the active solar cell layer or introducing metal nanostructures within the cell results in poor charge carrier collection due to increased surface recombination. Fang Jiao et al. [100] demonstrated that the imprinting of moth-eye-like structures on the front side of monocrystalline Si solar cell surface enhanced the conversion efficiency by 19% compared to the reference solar cell. This is achieved through coupling the incident light into the absorber layer. This approach of surface texturing differs from other approaches such as texturing the active material or using metal nanostructures. This approach

enhances solar cell performance without introducing additional surface recombination and also provides excellent solar cell self-cleaning functionality.

However, the use of printing periodic inverted nanopyramid structures have not been demonstrated on solar cells by means of UV nanoimprint lithography. The objective of this work was to determine the enhancement of monocrystalline Si solar cell performance employing periodic inverted nanopyramid structures using low cost and scalable approach.

In this work, the periodic inverted nanopyramid structures were fabricated on the front side of monocrystalline Si solar cell and commercially made polycrystalline Si solar cell surfaces by means of UV nanoimprint lithography. The reflectance, external quantum efficiency, current-voltage measurements and wettability of the monocrystalline Si solar cells and polycrystalline Si solar cells with and without the inverted nanopyramid structures were investigated. By applying the inverted nanopyramid structure coating on the monocrystalline Si solar cells and polycrystalline Si solar cells, enhancement of light trapping and power conversion efficiency in addition to high hydrophobic surfaces suitable for self-cleaning purposes were observed.

6.2 Experimental details

6.2.1 Fabrication of inverted nanopyramid patterns on solar cells

Figure 6.1 illustrates the schematic diagram of overall imprint process steps for the fabrication of inverted nanopyramid structures on a solar cell front surface. The periodic inverted pyramid structure master Si mold was fabricated by laser interference lithography and subsequent pattern transfer by combined reactive ion etching and KOH wet etching. Additional details on the fabrication process of master mold can be found in Chapter 3.

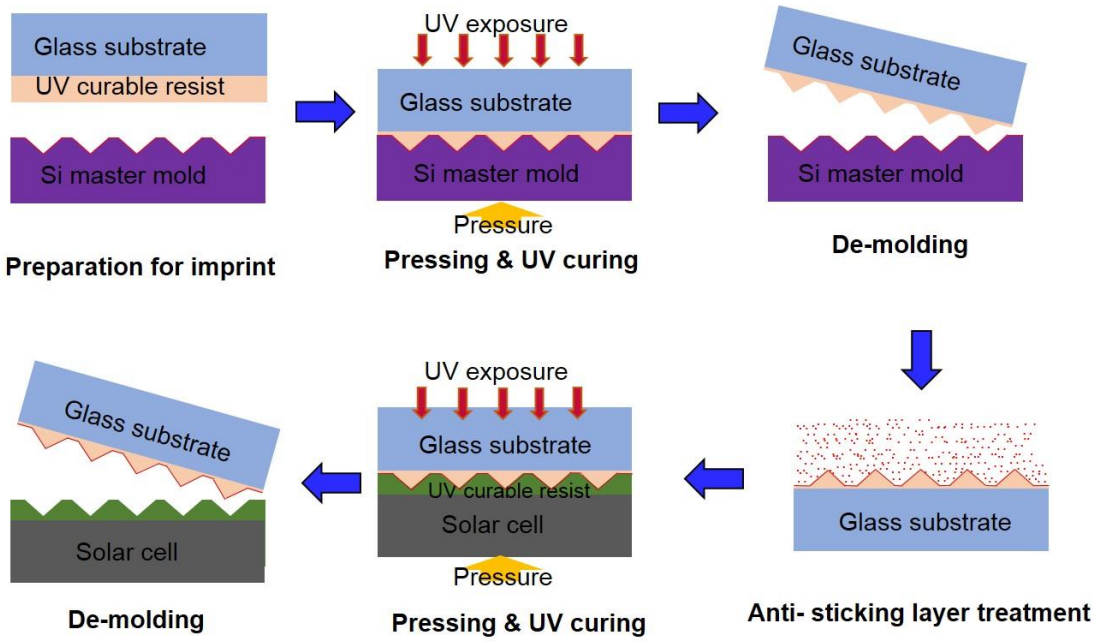

Figure 6.1: The schematic diagram of the overall fabrication process of inverted nanopyramid structures on a solar cell front surface.

The upright nanopyramid pattern was successfully replicated by UV nanoimprint process from the Si mold onto the glass substrate with high fidelity as described in Chapter 5. This is used as a stamp in the second imprint process to produce the inverted nanopyramid patterns. After the UV nanoimprint process, F_{13}-TCS based SAM was coated onto the upright nanopyramid patterned glass substrate as anti-sticking layer. More details of the UV nanoimprint process parameters and the tools which were used can be found in Chapter 4.

In order to determine and measure the role of the inverted nanopyramid structure for improving the photo-current conversion efficiency, the inverted nanopyramid structures were placed onto a monocrystalline Si and commercially manufactured polycrystalline Si solar cells, For meaningful comparison, the same UV imprinting process method used for upright nanopyramid patterned glass substrate was applied here. The monocrystalline Si

solar cells were fabricated in our laboratory under same conditions. Details of the monocrystalline Si solar cells fabrication processes are discussed in Section 5.2.2.

6.2.2 Characterization

The nanostructures of the samples were examined by scanning electron microscope (SEM) (JEOL 7000F FE-SEM) and atomic force microscope (AFM) to determine the pattern of the master stamp was replicated uniformly and faithfully on the top of the solar cells surface. The reflectance of the monocrystalline Si cell and polycrystalline Si solar cell with and without the inverted nanopyramid structures were obtained using UV-visible spectrophotometer at room temperature, with an integrating sphere over the wavelength range of 300-1200 nm. The current density-voltage characteristics were measured for the solar cells using a Keithley 2400 source meter and a solar simulator (ABET Sun3000) with AM 1.5G filter under illumination of 1 sun. The external quantum efficiency (EQE) was also performed using tungsten –halogen lamp in combination with a monochromator (CS130 1/8m). In addition, for hydrophobicity evaluation, the contact angle of water droplets on Si surface with and without the inverted nanopyramid patterns were measured using a contact angle goniometer with Edmund Scientific Camera.

6.3 Results and discussion

6.3.1 Surface patterned profiles

Figure 6.2(a) shows the top view SEM images of the periodic inverted nanopyramid Si master stamp. The upright nanopyramids replica stamp (Figure 6.2(b)) was imprinted from the master Si stamp (Figure 6.2(a)). The periodic inverted nanopyramid imprinted onto the surface of the solar cells (Figure 6.2 (c)) was obtained from the upright

nanopyramid replica stamp. It can be clearly seen that the inverted nanopyramid structures were transferred to the surface of the solar cell with high fidelity.

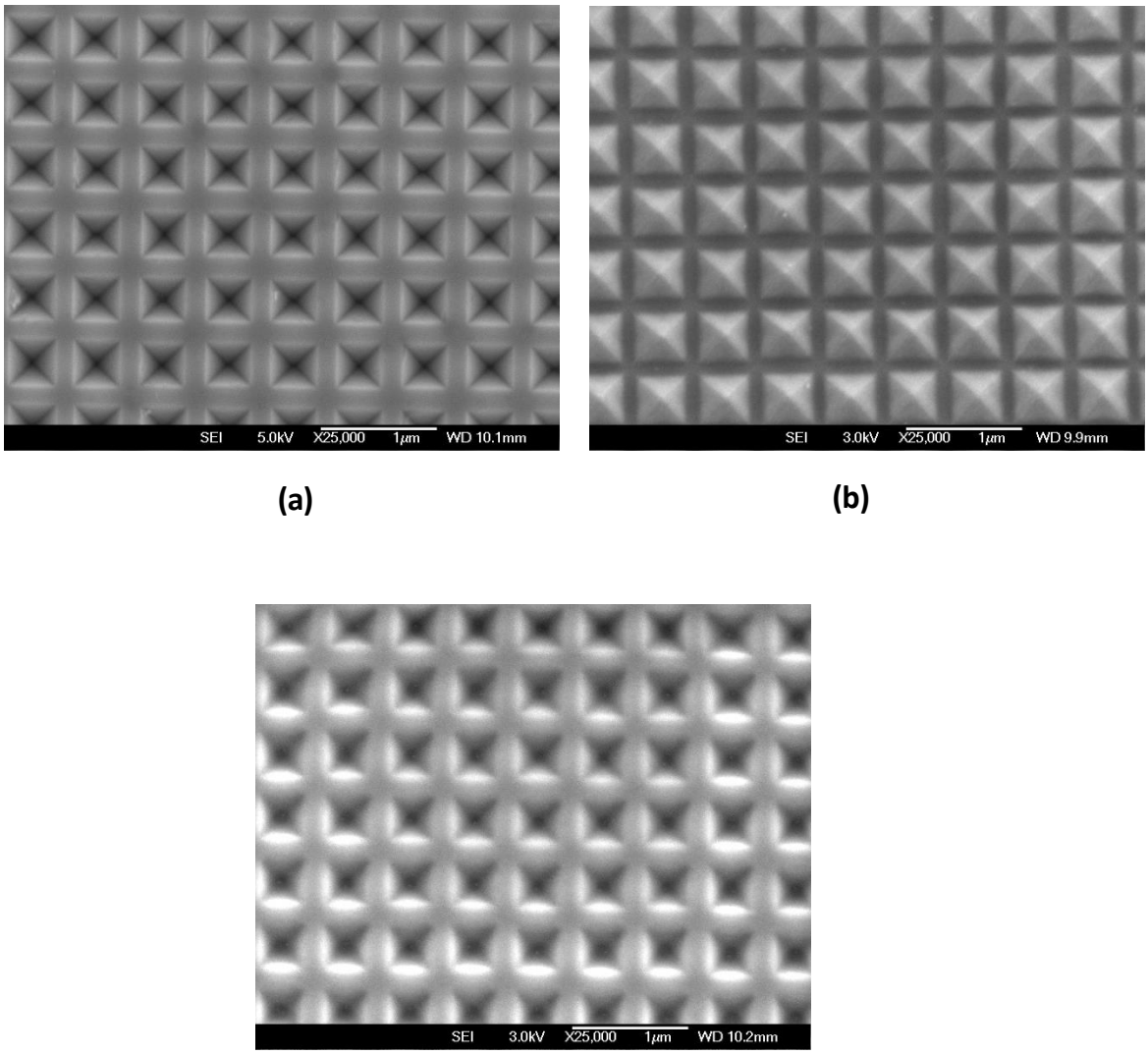

(a) **(b)**

(c)

Figure 6.2: Top view of SEM image of (a) the inverted nanopyramid Si master mold, (b) the upright nanopyramid replica stamp (c) the periodic inverted nanopyramid imprinted onto the surface of the solar cells.

Figure 6.3 (a), (b) and (c) show the 3D view AFM images of the periodic inverted nanopyramid Si master stamp, the negative replica on the glass and positive replica on solar cells, respectively. The periodic inverted nanopyramid structure had features with a width of about 450 nm, a height of about 310 nm and separation of about 125 nm and was transferred uniformly over the large area of 10x10 mm after two imprint processes.

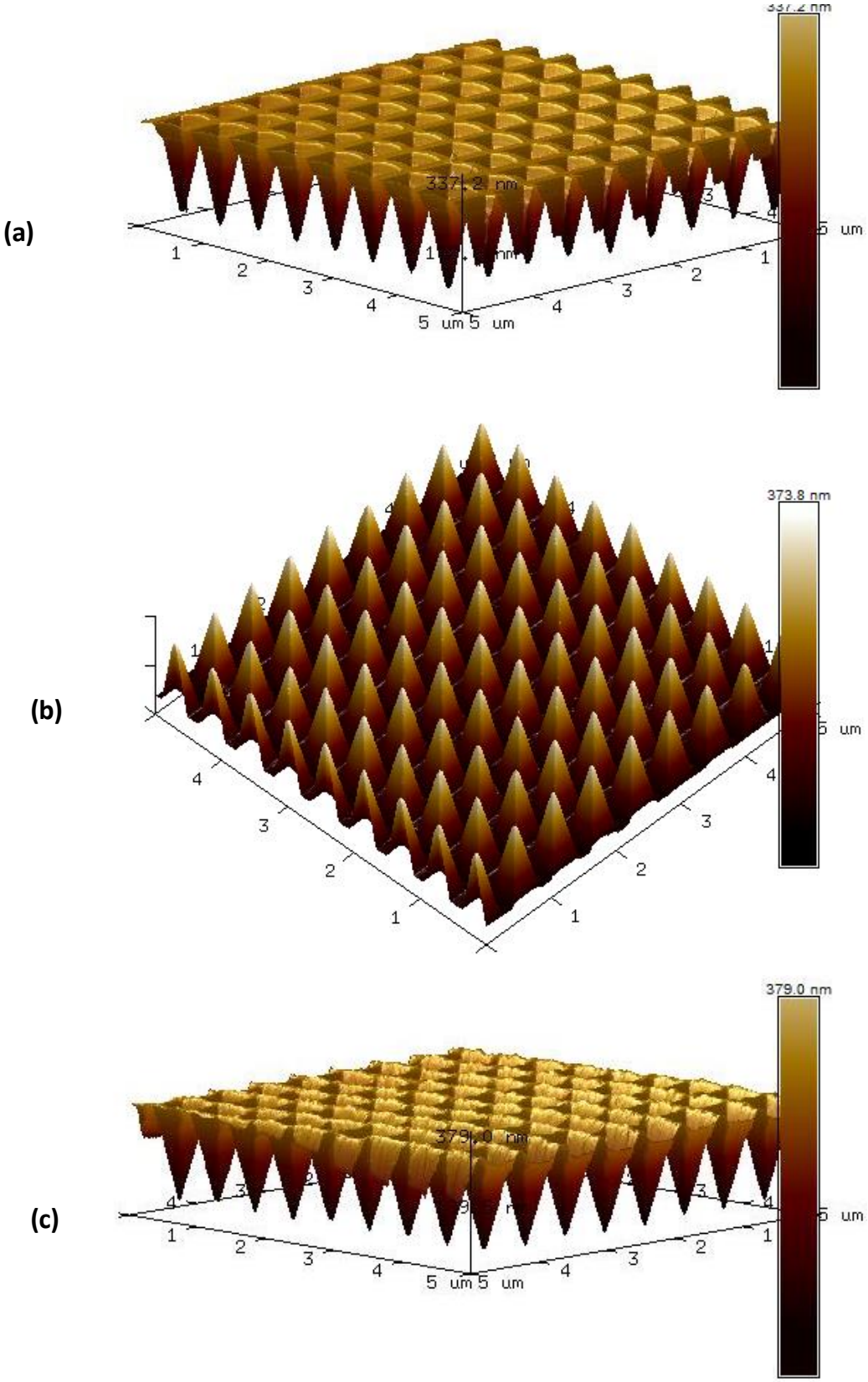

Figure 6.3: 3D view of AFM image of (a) the inverted nanopyramid Si master mold, (b) the upright nanopyramid replica stamp (c) the periodic inverted nanopyramid imprinted onto the surface of the solar cells.

6.3.2 Optical properties and device performance

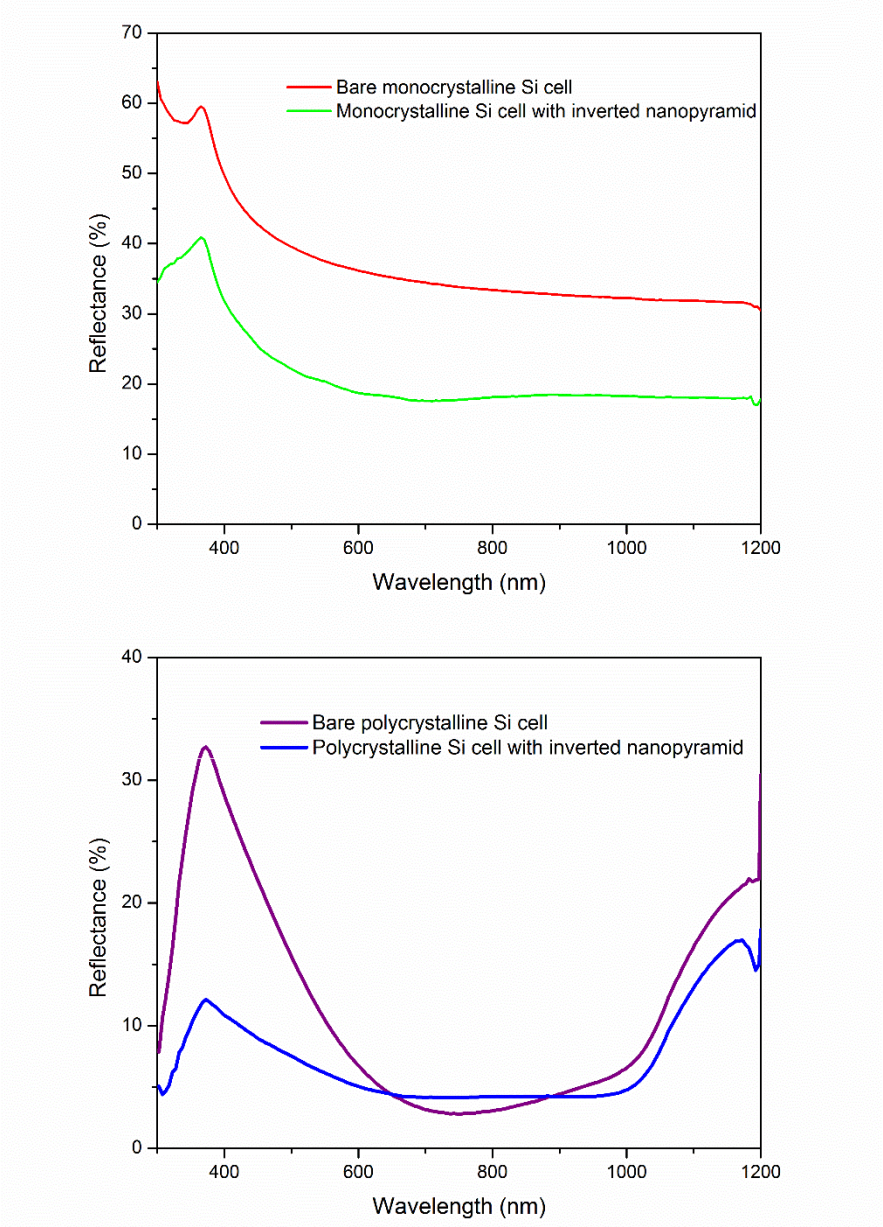

Figure 6.4: Reflectance of (a) a monocrystalline Si cell and (b) a polycrystalline Si cell with and without the inverted nanopyramid structure measured as a function of wavelength.

Figure 6.4 (a) and (b) show the reflectance of the monocrystalline Si surface and polycrystalline Si surface with and without coating of inverted nanopyramid structures measured as a function of wavelength, respectively. From Figure 6.4, it can be observed that the surface reflectance of the monocrystalline Si with the inverted nanopyramid layer

was significantly decreased over the broad wavelength range from 300nm to 1200nm compared to the planar solar cells due to the gradual change in the refractive index between the air and Si surfaces obtained by the inverted nanopyramid layer.

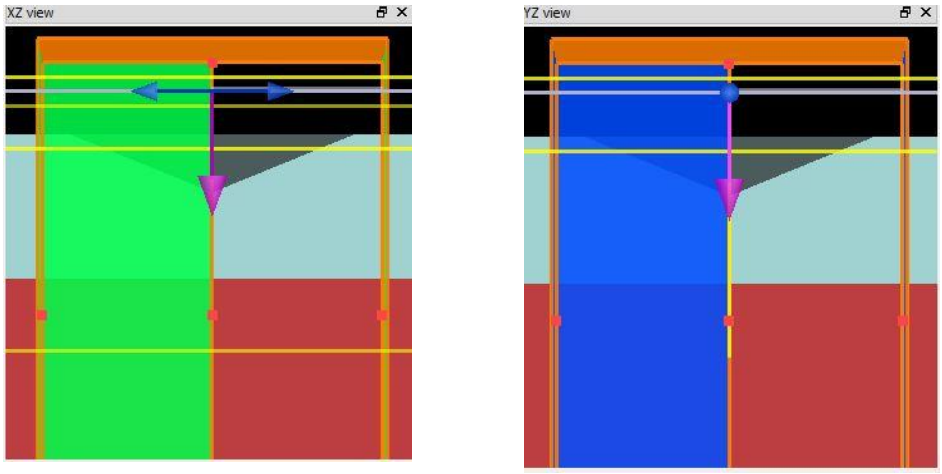

Figure 6.5: FDTD simulation model layout of the INP coated Si substrate.

Figure 6.5 shows the FDTD simulation model layout of the INP coated Si substrate. Perfectly matched layers (PML) and periodic boundary conditions were used in the perpendicular and horizontal directions. In order to verify the reflectance spectra obtained from the experiments, FDTD simulations were performed with and without INP structure, resulting simulated reflectance spectra as illustrated in Figure 6.6. It is apparent that the theoretical reflection spectra for bare Si substrate is close to the experimental results. The overall trend of simulated reflectance spectra is quite consistent with that of the experiment data, with apparent reduction of reflectance for INP structures. Meanwhile, oscillations of the reflectance spectra can be attributed to the limitation of the modeling where the OrmoStamp layer is assumed to have a uniform refractive index over broad wavelength range.

.

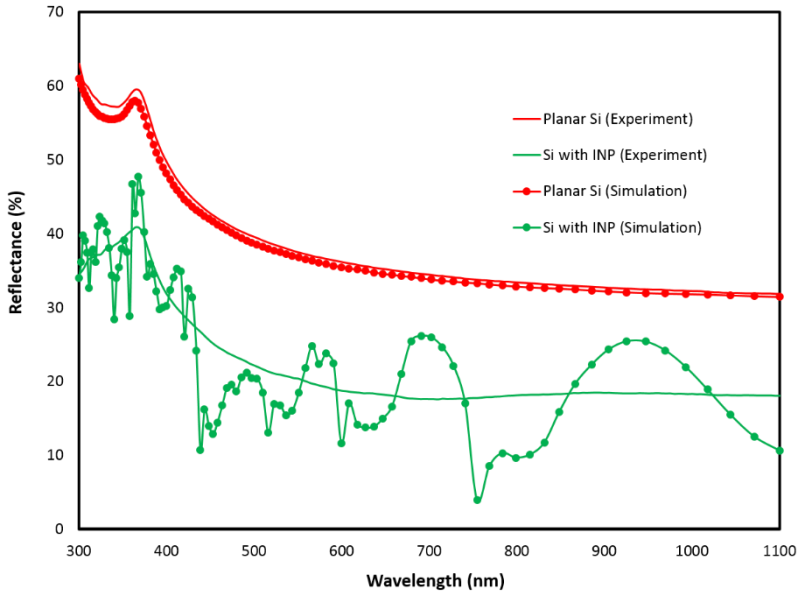

Figure 6.6: Experimental and FDTD- simulated optical reflectance spectra of Si surface with and without INP structure as a function of wavelength.

Moreover, to shed light on how the light is coupled into INP structure, the cross-sectional electric field intensity distributions at different wavelength were obtained for the incident light propagating from air to the Si substrate with and without INP structure as illustrated in Figure 6.7.

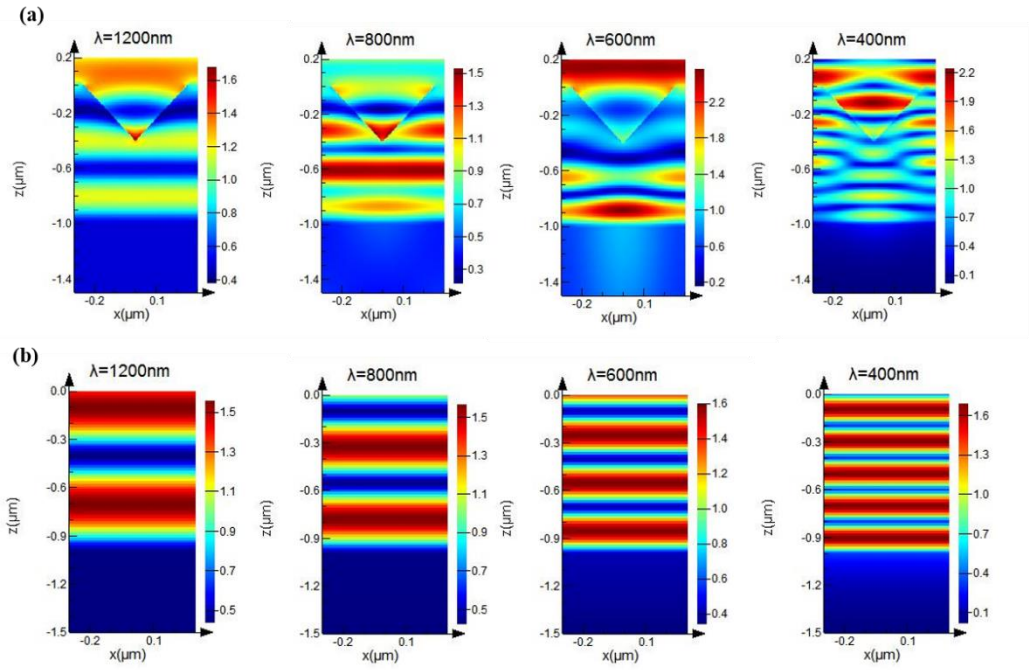

Figure 6.7: The cross-sectional electric field distribution profiles at different wavelength by FDTD analysis (a) INP coated Si with period of 600nm, size of 500nm and depth of 400nm and (b) bare Si.

As shown in Fig. 6.7, it can be seen that the existence of INP structure results in weaker interference and weaker intensity of the reflected wave. In addition, it can clearly be seen from the strong electric field distribution inside the INP structure that the EM wave energy can be efficiently coupled into the INP structures. This is because more incident photons are coupled into the device the due to the formation of a gradual refractive index gradient profile of INP structure.

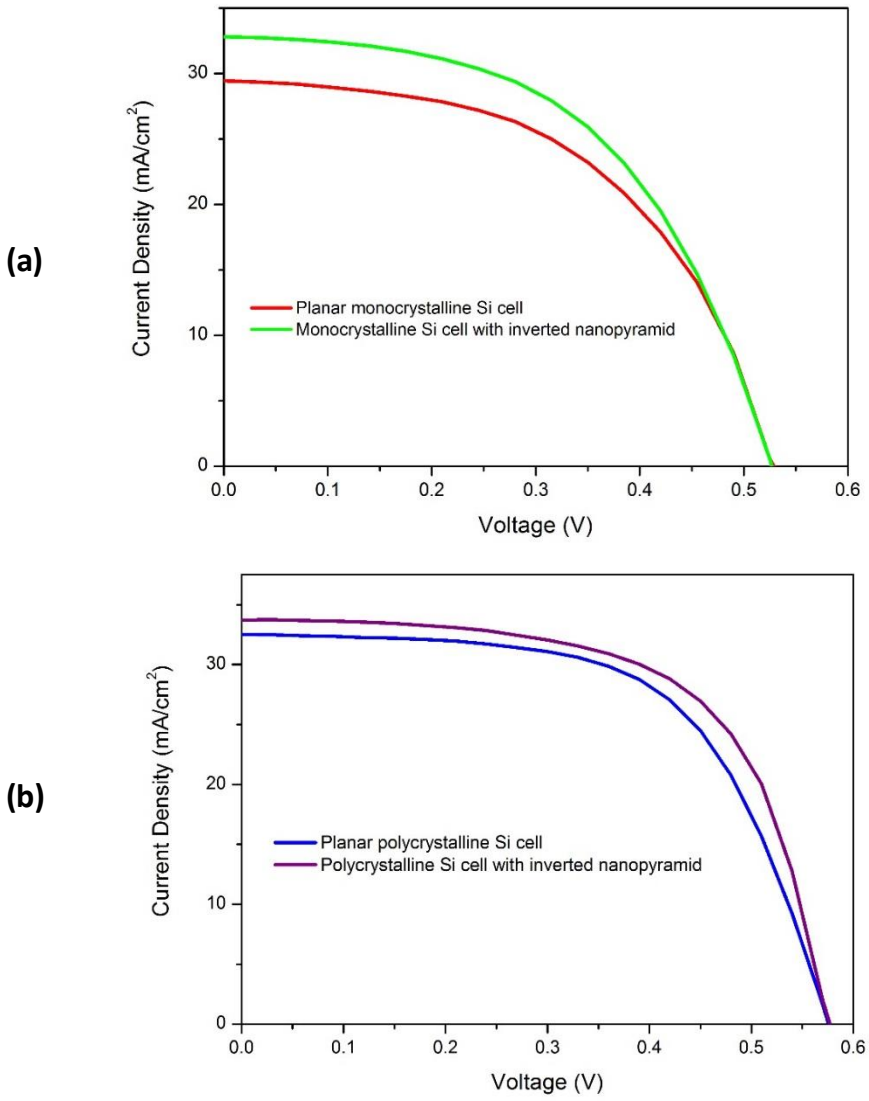

Figure 6.8: Current density – voltage (J-V) characteristics of (a) a monocrystalline Si solar cell and (b) polycrystalline Si solar cell with and without the inverted nanopyramid structures under AM 1.5 illumination.

Figure 6.8 (a) and (b) show the J-V characteristics of the monocrystalline Si solar cell and polycrystalline Si solar cell with and without the inverted nanopyramid structures under AM 1.5 illumination, respectively. The photovoltaic parameters of the monocrystalline Si solar cell and polycrystalline Si solar cell with and without nanopyramid structures extracted from these J-V curves are summarized in Table 6.1 and Table 6.2.

Table 6.1 Device characteristics of monocrystalline Si solar cells with and without inverted nanopyramid structures.

Monocrystalline Si solar cells	*V_{OC} (V)*	*J_{SC} ($mAcm^{-2}$)*	*FF (%)*	*PCE (%)*
Planar cell	0.525	29.442	52.550	8.122
INP patterned cell	0.525	32.793	52.711	9.075

Table 6.2 Device characteristics of polycrystalline Si solar cells with and without inverted nanopyramid structures.

Polycrystalline Si solar cells	*V_{OC} (V)*	*J_{SC} ($mAcm^{-2}$)*	*FF (%)*	*PCE (%)*
Planar cell	0.570	32.512	61.273	11.355
INP patterned cell	0.570	33.725	63.127	12.135

With the use of inverted nanopyramid structures, the J-V characteristics show that there was no significant change in the open circuit voltage (V_{OC}). However, the short-circuit current density (J_{SC}) of planar monocrystalline Si solar cell and polycrystalline Si solar cell increased from 29.422 $mAcm^{-2}$ to 32.793 $mAcm^{-2}$ and from 32.512 $mAcm^{-2}$

to 33.725 $mAcm^{-2}$, respectively. This J_{SC} increment was mainly due to the reduced reflectance resulting from the inverted nanopyramid structure over a broad wavelength range as shown in Figure 6.4. As a result, the conversion efficiency of the monocrystalline Si solar cell and polycrystalline Si solar cell with inverted nanopyramid were increased significantly from 8.122% to 9.075% and from 11.355% to 12.135%, respectively. These efficiencies were 11.733% and 6.869% higher than the result obtained for the planar monocrystalline Si solar cell and polycrystalline Si solar cell, respectively.

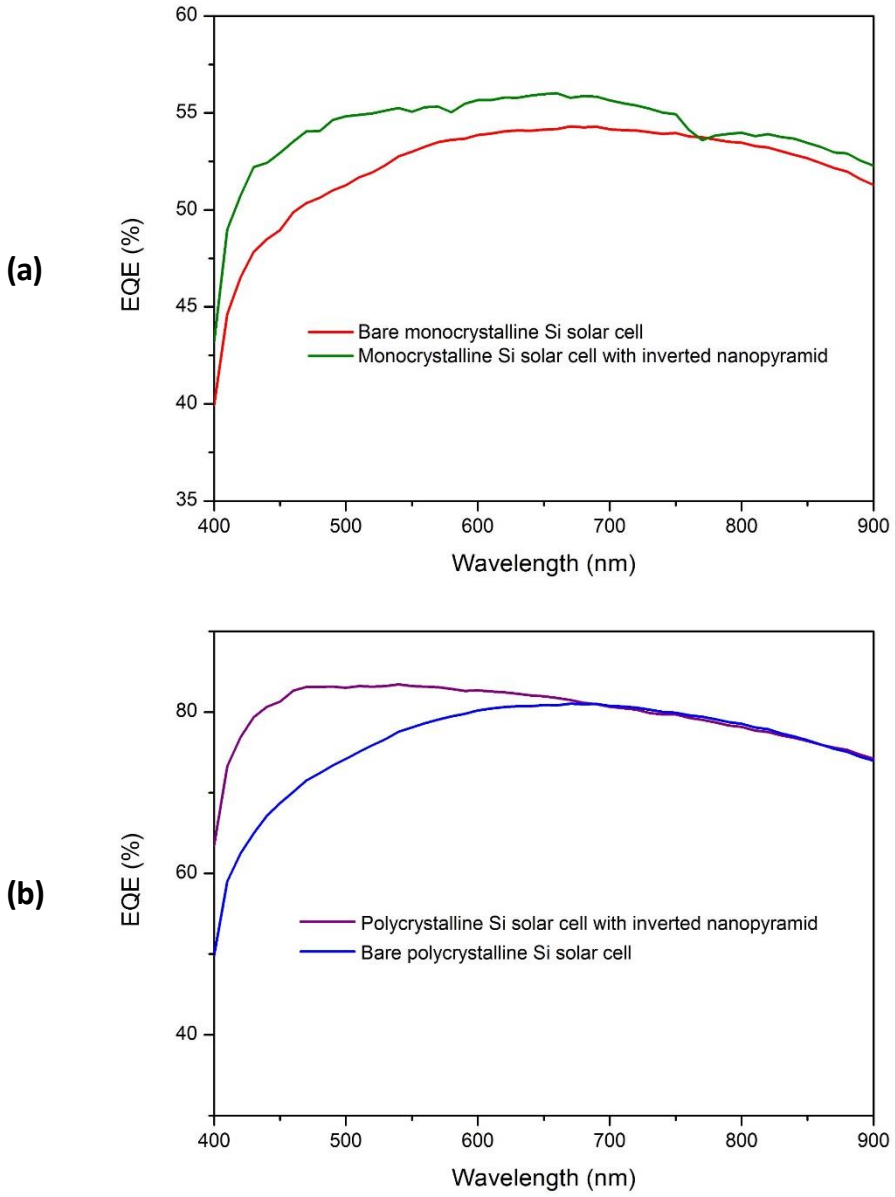

Figure 6.9: The EQE values of (a) a monocrystalline Si solar cell and (b) polycrystalline Si solar cell with and without the inverted nanopyramid structures as a function of wavelength.

The EQE curves for the monocrystalline Si solar cells and the polycrystalline Si solar cells with and without inverted nanopyramid layer are shown in Figure 6.9. This EQE measurement was carried out under a monochromatic illumination with a tungsten-halogen lamp coupled to a monochromator. The EQE values of the monocrystalline Si solar cell and polycrystalline Si solar cell with inverted nanopyramid layer were significantly improved over the entire wavelength range compared to the non-imprinted solar cell. For instance, the EQE value increased by about 8% at 450 nm. This higher EQE values for the solar cells with inverted nanopyramid indicates enhanced light trapping, and reduced the reflections due to the imprinted nanostructures on top of the solar cell surface. This result was precisely matched with the reflectance value results shown in Figure 6.4.

These results demonstrate that the periodic inverted nanopyramid structures reduced reflections, increased short circuit current and improved the efficiency of the monocrystalline silicon solar cells and polycrystalline solar cells under this study. This is due to the formation of a gradual refractive index gradient between air and the solar cell, which can reduce the Fresnel reflectance and direct more incident light inside the solar cell active material. The combined light trapping and antireflection effect have been improved, and the optical path length has been prolonged by the inverted nanopyramid structures, resulting in increasing the overall conversion efficiency of the monocrystalline Si solar cells and polycrystalline Si solar cells. In addition, the nanopyramid coating can be applied after the solar cell fabrication is completed to eliminate any losses due to surface damage by the etching processes [22].

The light trapping technologies such as nanopillars[187], nanowires[188] and nanoholes[58] have been developed with the aim of enhancing the optical absorption within the active layer. However, a major reason for lower PCE in solar cell with

nanopillars, nanowires and nanoholes is the high recombination rates due to the larger surface area, which is usually more than an order of magnitudes larger that the planar cells[189]. Compared to other nanostructures like as nanopillars, nanowires and nanoholes, the nanopyramid structures have smoother surface and lower surface area enhancement ratio[60].

The effect of shape on the anti-reflective performance can be explained by using the effective medium theory[43]. According to the effective medium theory, the periodic structures can make the refractive index of the surface layer change gradually from air to substrate and therefore effectively suppress the surface reflection due to the large refractive index discontinuity at the two interface. For instance, the effective refractive index for the nanopillar structure would be an abrupt change at top of the nanopillar structure and then maintain the constant value from the top of the structure to the bottom. Meanwhile, the effective refractive index for the nanopyramid structures changes gradually from top of the structure to the bottom, which indicated refractive index of the nanopyramid structures shows better continuity than nanopillar and results in lower possible reflection. Therefore, nanopyramid structures could be a good choice for light harvesting due to their gradient refractive index profile that provided the best combination of antireflection and light-trapping properties.

6.3.3 Surface wettability

In outdoor environments, the solar cells can be easily contaminated by dust particles, which interfere with incident light affecting cell light absorption and thus reducing the device performance. Therefore, a self-cleaning ability at the top surface of the solar cell would maintain the cell performance when exposed to dusty environments [96, 171].

Figure 6.10 shows the contact angles values of water droplets on the bare solar cell, inverted nanopyramid patterned solar cell, and SAM-coated inverted nanopyramid patterned solar cell. As shown in Figure 6.10, the contact angle of the solar cell was increased from 55 to 96° after the formation of inverted nanopyramid structure, which exhibited a hydrophobic behavior. Moreover, the hydrophobicity was enhanced with SAM-coated inverted nanopyramid structures. In this case, the contact angle of the SAM-coated patterned solar cell was increased to 125°. As a result, solar cells with inverted nanopyramids can utilize the self-cleaning functionality induced by the high hydrophobic surface properties in addition to their antireflection properties.

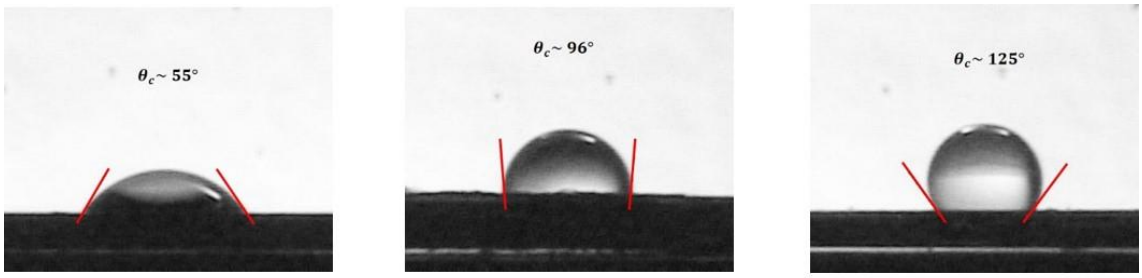

Figure 6.10: Photographs of a water droplet on (a) bare solar cell, (b) patterned solar cell and (c) SAM-coated patterned solar cell. θ_c is a water contact angle.

6.4 Summary

The periodic inverted nanopyramid structures were utilized as front surface coatings for the monocrystalline solar cells and commercially made polycrystalline Si solar cells using a UV nanoimprint lithography. The pyramid coating can be applied after cell fabrication to eliminate any losses due to surface damage by the etching processes. The periodic inverted nanopyramid structures have successfully reduced the Fresnel reflection and led to directing and trapping more incident light into the monocrystalline and polycrystalline Si solar cells, thereby improving the short circuit current density and enhancing the power conversion efficiency. The power conversion efficiency of the monocrystalline Si solar cell and the polycrystalline Si solar cell with inverted nanopyramid structure were improved by 11.733% and 6.869% compared to the identical solar cells without the surface treatment. In addition, the high hydrophobicity of the solar cells with inverted nanopyramid structures provided a self-cleaning functionality. These results suggest that the periodic inverted nanopyramid structures with antireflection properties and self-cleaning properties could be useful for different types of solar cells including thin films, flexible substrates and transparent cells.

Chapter 7 Effects of film thickness and sputtering power on the properties of ITO thin films deposited by RF magnetron sputtering

In this chapter, the effects of film thickness and sputtering RF power on the surface morphological, optical and electrical properties of Indium tin oxide (ITO) thin films and the deposition of ITO films onto the upright nanopyramid structured glass substrate are presented. The ITO thin films were grown on a glass substrate without introducing oxygen into the growth environment using RF magnetron sputtering technique. The dependence of surface morphological, optical and electrical properties at different film thicknesses and sputtering RF power were investigated. Results showed that these properties were strongly influenced by the film thickness and sputtering RF power. It was found that the resistivity, sheet resistance and optical transmittance of ITO thin films deposited on glass substrate decreased as film thickness increased from 75 nm to 225 nm while the surface roughness and optical bandgap increased. The optimum properties were obtained for ITO films 225 nm thick grown at 250 W RF power. This has revealed an excellent figure of merit of ($38.4 \times 10^{-4}\ \Omega^{-1}$) with average transmittance (83.3 %), resistivity ($9.4 \times 10^{-4}\ \Omega.cm$), and carrier concentration ($6.1 \times 10^{20}\ cm^{-3}$). Finally, the ITO films were conformally deposited onto upright nanopyramid structured glass substrate using optimized parameters. These nanostructured ITO substrates are suitable for use as transparent contacts for solar cell applications to improve their performance and efficiency.

7.1 Introduction

Indium tin oxide (ITO) thin films have been widely utilized in transparent and flexible optoelectronics device fabrication technologies such as liquid crystal displays, plasma display panels, gas sensors, flat panel displays, solar cells and organic light-emitting diodes [190-193]. This is due to their low electrical resistivity and high optical transmission in the visible range. Various coating techniques have been utilized to deposit ITO thin films such as DC/RF magnetron sputtering [194], reactive thermal evaporation [195], ion beam sputtering [196], pulsed laser deposition [197], chemical vapour deposition [198] and spray pyrolysis [199]. Among these techniques, RF magnetron sputtering is one of the most extensively used deposition technique in many industries, due to its inherent advantages such as good reproducibility, low temperature process and large area film deposition capability [200]. However, the properties of ITO film are critically dependent on various deposition parameters, such as working gas pressure, RF power, chamber environment, film thickness, target to substrate distance, substrate temperature, target specification and post deposition treatment [201, 202]. In the majority of reports, oxygen was used as a reactive gas during deposition and/or post-deposition annealing to decrease the resistivity of the films [203-205]. However, oxygen usage during either deposition or post-deposition annealing complicates the process and puts an extra unnecessary strain on the vacuum chambers.

In this study, ITO thin films were grown by RF magnetron sputtering at room temperature without introducing oxygen into the growth environment. The main objective of this study is to evaluate the effects of film thickness and sputtering RF power on the surface morphological, optical and electrical properties of ITO thin films without introducing oxygen into deposition atmosphere. In addition, optimization of film

thickness and sputtering RF power without added oxygen to produce high performance ITO suitable for solar cells applications has been demonstrated.

7.2 Experimental details

7.2.1 Preparation of ITO thin films

In this work, ITO thin films were deposited on 0.5mm thick soda-lime glass substrates (20 mm × 20mm) by RF magnetron sputtering system (Edwards Auto500) using a solid ITO target (90:10 wt% In_2O_3:SnO_2) with a purity of 99.99% , a diameter of 75 mm and 5mm thick. The substrates cleaning procedure were normally carried out by dipping for few minutes in acetone, methanol, and isopropyl alcohol (IPA) solvents in an ultrasonic bath and rinsed with deionized water and then blown dry with Nitrogen gas. The surface was further treated using oxygen plasma for 20 minutes before being loaded into the sputtering system.

The sputterer chamber was pumped down using a turbomolecular pump before introducing the sputtering Ar gas, which had high purity (99.999%) and free of oxygen. The base pressure of the chamber was in the range of about 3×10^{-6} mbar. The deposition process was carried out in an Ar flow rate of 10 sccm at room temperature (295K) with a processing pressure of 3.2×10^{-3} mbar. No oxygen was added during the deposition. The substrate holder was continuously rotated during the sputtering to enhance the film's uniformity. The ITO films were grown at different thicknesses ranging from 75 nm to 225 nm with a 50 nm increment at an RF power of 100 W. The films were also deposited at different RF powers from 100 W to 250 W in a 50 W steps to produce a fixed thickness of 225 nm. After deposition, the deposited films were diced into $5mm^2$ samples using a Tempress 602 dice saw system for the structural, optical and electrical analyses. After the optimization of sputtering parameters for solar cells applications, the ITO films were

deposited on upright nanopyramids structured glass substrate at the optimized conditions. The fabrication process of upright nanopyramid structured glass substrates are described in Chapter 4.

7.2.2 Film characterization

The thickness of the films was measured using a Surface Profilometer DEKTAK 150. The surface morphology of the deposited films was observed by atomic force microscopy (AFM) under ambient air conditions. The optical transmittance spectra of films were carried out by a Cary Spectrophotometer 619 in the wavelength range from 200 to 800 nm. Hall mobility, carrier concentration, and resistivity were measured using Van der Pauw Hall effect measurement method under a magnetic field of 0.51T. All measurements were conducted at room temperature (295 K). The upright nanopyramid structured ITO films were examined by scanning electron microscope (SEM) (JEOL 7000F FE-SEM).

7.3 Results and discussion

7.3.1 Surface morphological analysis

Figure 7.1(a) – (d) shows the AFM images of the surface morphologies of ITO films with thickness ranging from 75 nm to 225 nm prepared at an RF power of 100W respectively. Root mean square roughness, Rq, was determined from AFM data of 1 µm× 1 µm scan area. The calculation was done by using Equation 7.1, where N is the number of equally spaced points along the trace, and Z_i is the vertical distance from the mean line to the i^{th} data point.

$$R_q = \sqrt{\frac{1}{N}\sum_{i=1}^{N} {Z_i}^2} \qquad (7.1)$$

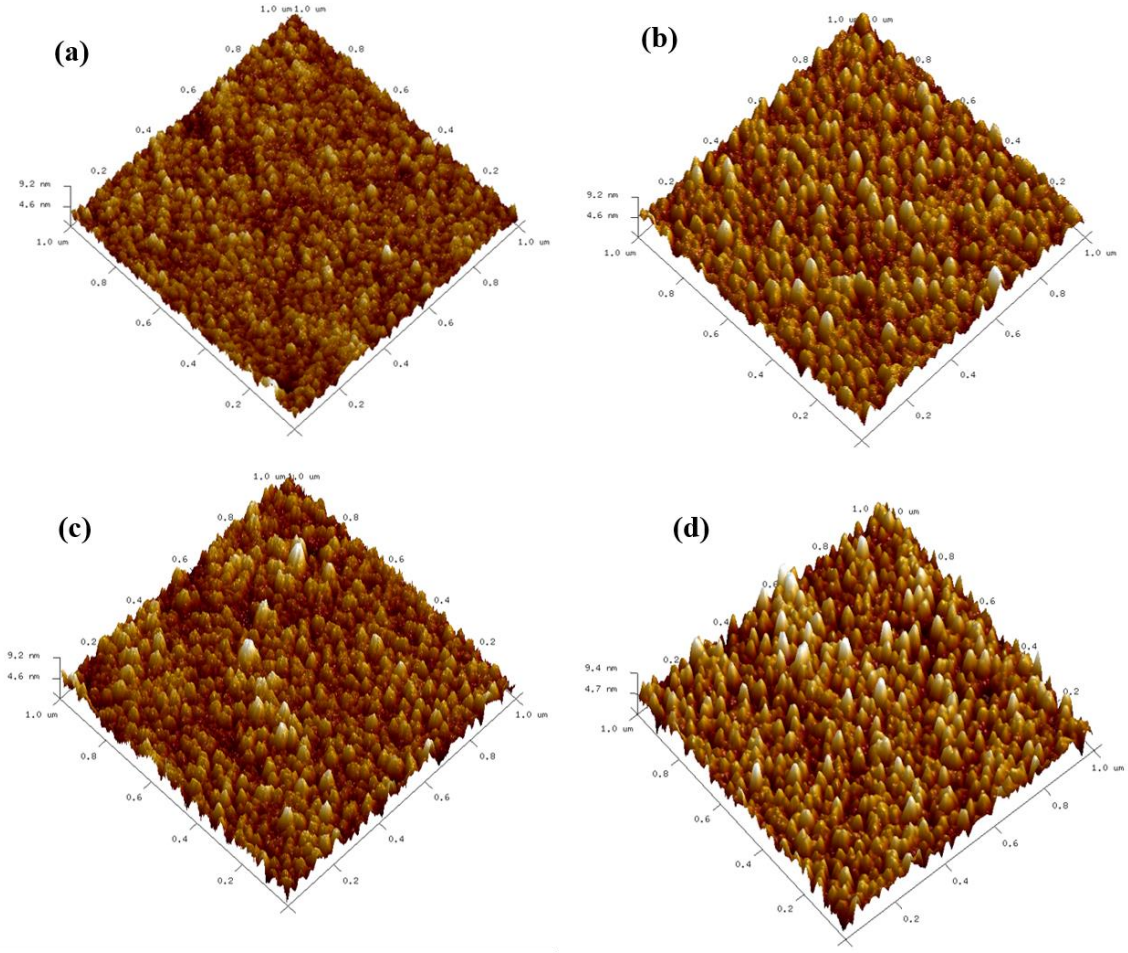

Figure 7.1: AFM images of ITO films at an RF power of 100 W with different thicknesses (a) 75nm, (b) 125nm, (c) 175nm, and (d) 225nm.

The surface roughness increases slowly as the film thickness increases from 75 to 225 nm. It can be clearly seen from Figure 7.2 that, as the thickness reaches 225 nm, the RMS roughness rises up to 12.5 Å. These significant changes in roughness with increasing film thickness is due to the reflecting nucleation, coalescence and continuous film growth processes (Volmer – Weber type) [206]. Figure 7.1 demonstrates that the RMS value of the roughness is strongly influenced by the degree of aggregation and cluster size of the thin films. This is in agreement with the principle that different cluster or grain size affects the surface roughness of the thin films [207].

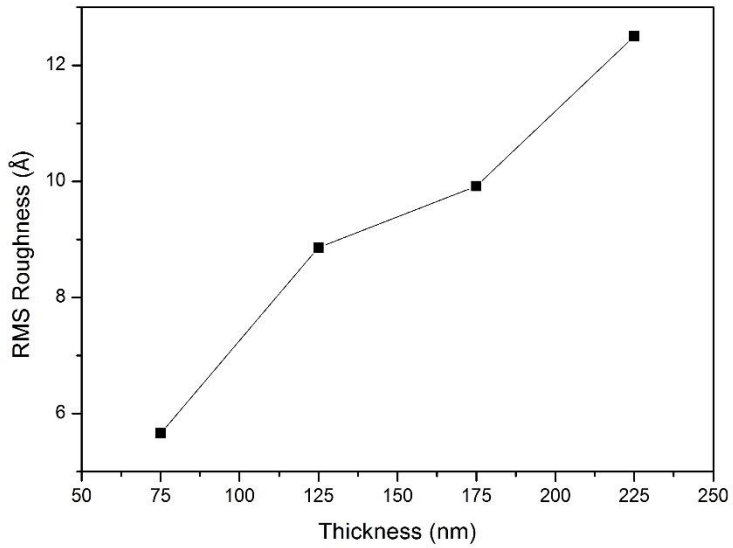

Figure 7.2: RMS roughness R_q of the surface of ITO films deposited at an RF power of 100 W with different thicknesses.

Figure 7.3(a) – (d) shows the AFM images of the surface morphologies of the 225nm thick ITO films prepared with different RF powers in the range from 100 W to 250 W. The values of the RMS roughness for the 225 nm thick ITO films deposited with RF power varying from 100 W to 250 W are shown in Figure 7.4. It is observed that the sputtering RF power also has an influence on the surface structure of ITO films. The ITO films grown at 100 W RF power have the comparatively low kinetic energy of sputtered particles compared to 250 W RF power, which leads to relatively more random orientation and various sizes of grain growth which lead to manifest as a rough surface. The sputtered particles have sufficient energy for uniform distribution of grain growth and thus lead to a smoother surface with increasing in RF sputtering power.

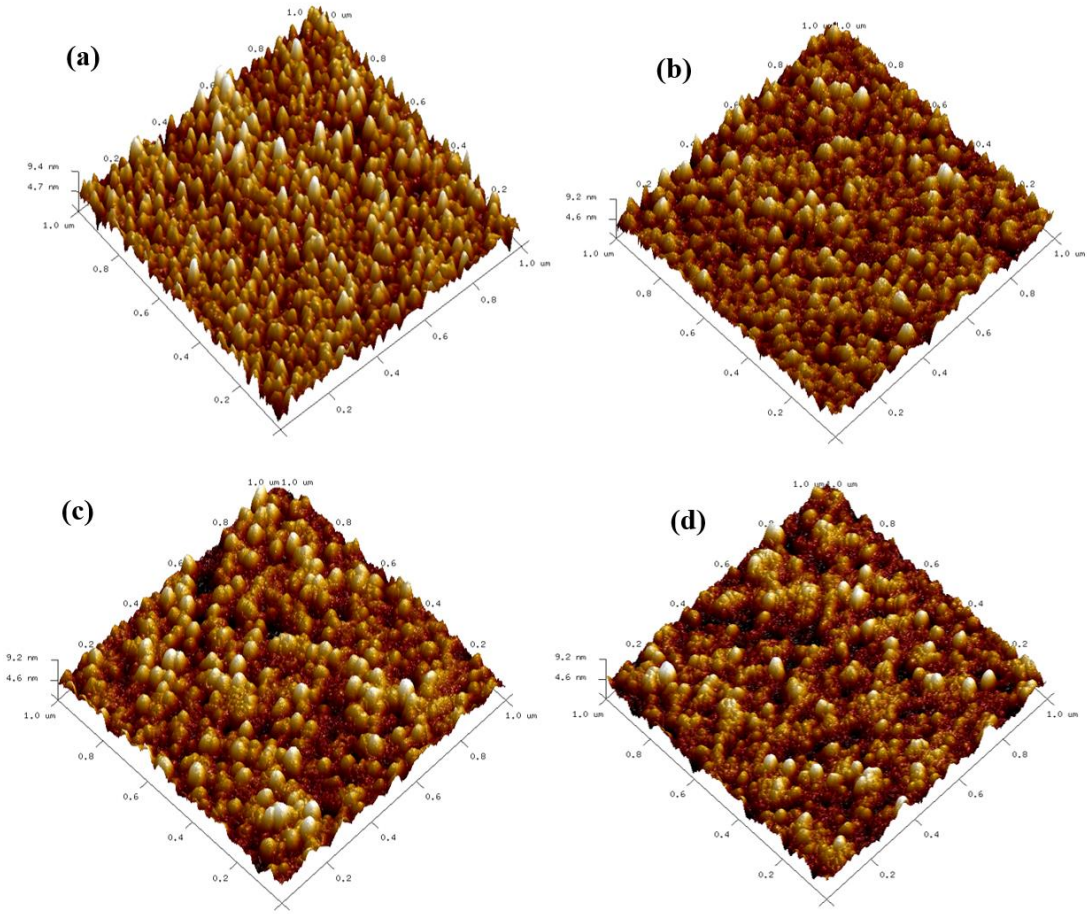

Figure 7.3: AFM images of 225 nm thick ITO films with different RF power (a) 100 W, (b) 150 W, (c) 200 W, and (d) 250 W.

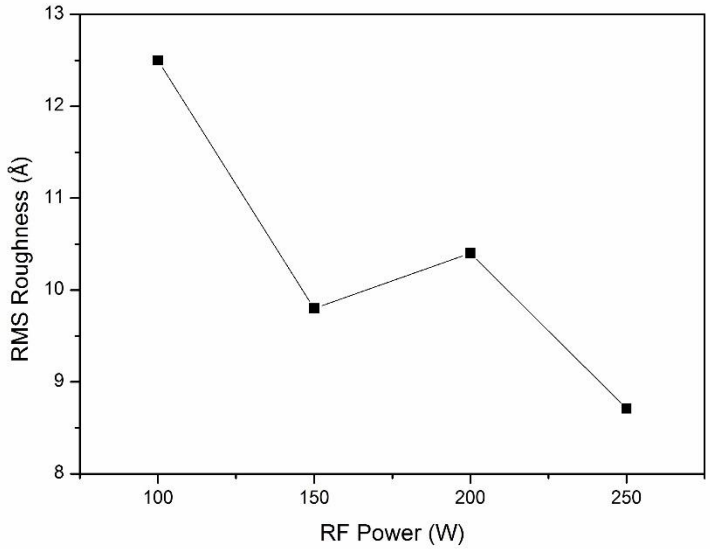

Figure 7.4: RMS roughness R_q of the surface of 225 nm thick ITO films deposited with different RF power.

7.3.2 Electrical properties

Figure 7.5 illustrates the variation of resistivity, carrier concentration, and Hall mobility of the ITO films grown at an RF power of 100W as a function of film thickness. Carrier concentration increases rapidly with the film thickness increasing from 75 nm to 225 nm and reaching a maximum of 1.12×10^{21} cm^{-3}. It is also observed that resistivity decreases with an increase in the film thickness from 75 to 175 nm and remains almost constant afterwards.

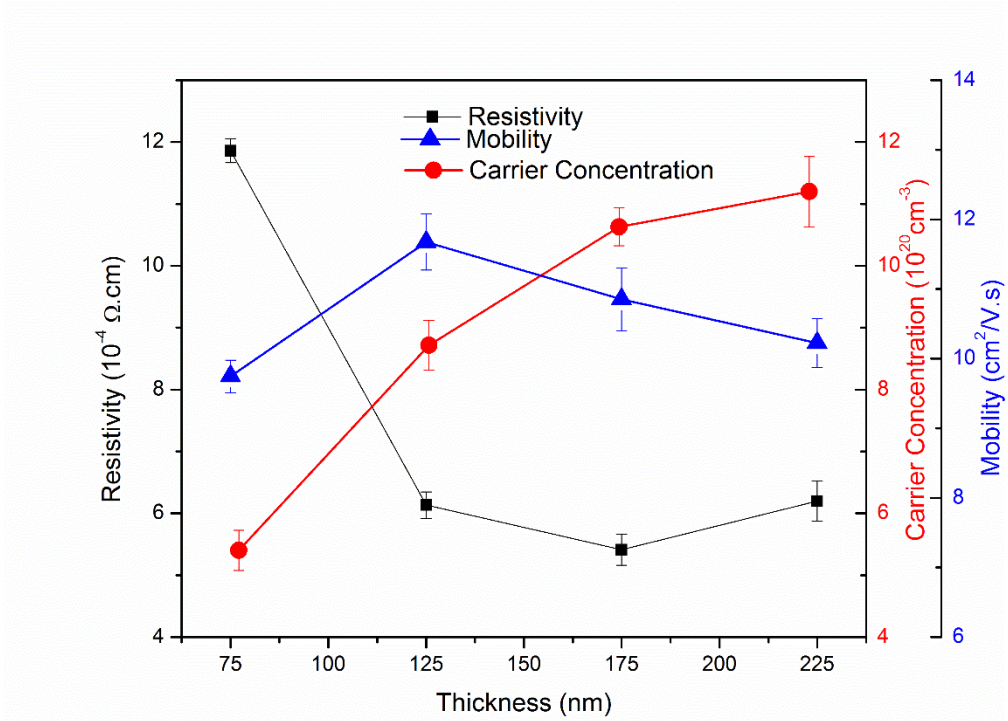

Figure 7.5: Variation of the resistivity, carrier concentration and Hall mobility of ITO films with film thickness.

Figure 7.6 shows the sheet resistance and the resistivity as a function of the film thickness. The sheet resistance of ITO thin films is calculated by the following equation:

$$R_s = {}^{\rho}/_{t} \qquad (7.2)$$

Where ρ – resistivity, t – thickness of ITO film and R_S sheet resistance.

It is found that the sheet resistance decreases rapidly as the ITO film thickness increases from 75 nm to 125 nm. For further increase of the ITO film thickness, the sheet resistance decreases slowly and the minimum sheet resistance obtained is about 27.5 Ω/sq for a film thickness of 225 nm. The decrease in sheet resistance with increasing film thickness is due to an increase in carrier concentration of the films which results from the enlarged grain size. It has been reported by H Kim et al that grain size increased with an increase in ITO film thickness [208] which support our findings. The values of the carrier mobility drop with increased surface roughness, probably, due to the electron scattering at the grain boundaries and increse in density of surface states. It has also been reported that the carrier mobility is limited by the grain boundaries [209]. However, the carrier mobility increases as the film thickness increased from 75 nm to 125 nm then decreases as the film thickness increased from 125 to 225 nm.

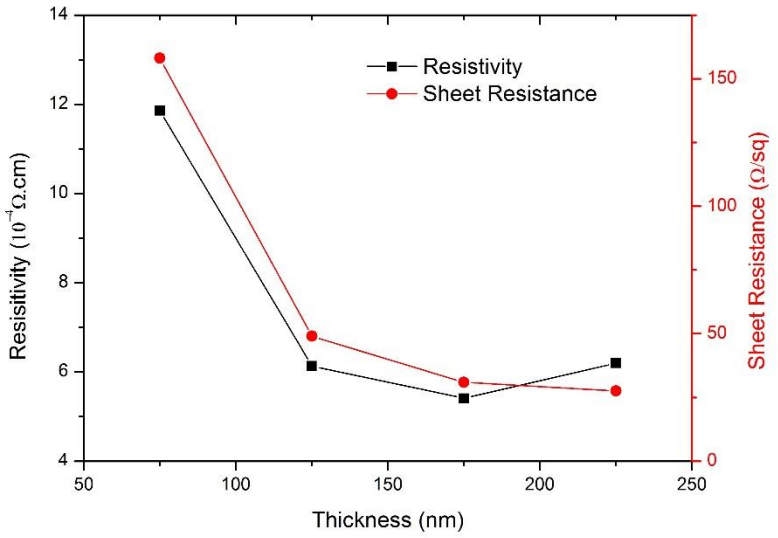

Figure 7.6: Variation of the resistivity and sheet resistance of ITO films with film thickness.

Figure 7.7 shows the electrical resistivity, carrier concentration and Hall mobility of the 225 nm thick ITO films as a function of the RF power. Carrier concentration decreases

from 1.12×10^{21} cm^{-3} to 6.07×10^{20} cm^{-3} when RF power is increased from 100 W to 250 W. This indicates that the increased damage by the negative ion collision influences the carrier concentration. The mechanism of carrier concentration drop by the negative ion damage can be explained by the decrease in oxygen vacancies as donors and the increase in bivalent In or Sn as acceptors [210].

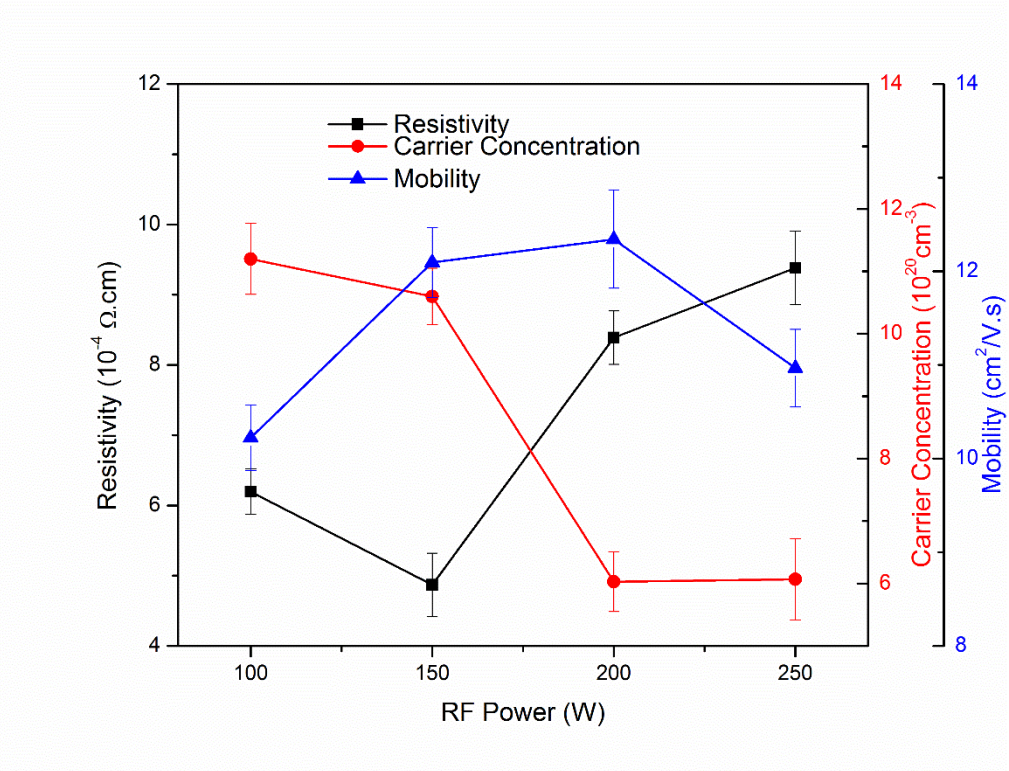

Figure 7.7: Variation of the resistivity, carrier concentration and Hall mobility of 225 nm thick ITO films grown at various RF power.

The carrier mobility increases gradually with RF power in the range from 100 W to 200 W then decreases rapidly when the RF power is increased above 200W. There is a slight fall in the resistivity and sheet resistance for an RF power between 100 W and 150 W as shown in Figure 7.8. However, the values of the resistivity increase gradually when the RF power is in the range from 150 W to 250 W. The decrease in sheet resistance with an increase in RF power from 100 to 150 W is attributed by a lower collision of negative ions [210]. While for an RF power over 150 W, bombardments became stronger which

lead to a low density of Oxygen vacancies. In general, this result indicates that a lower sputtering RF power is preferred for decreasing the resistivity of ITO film.

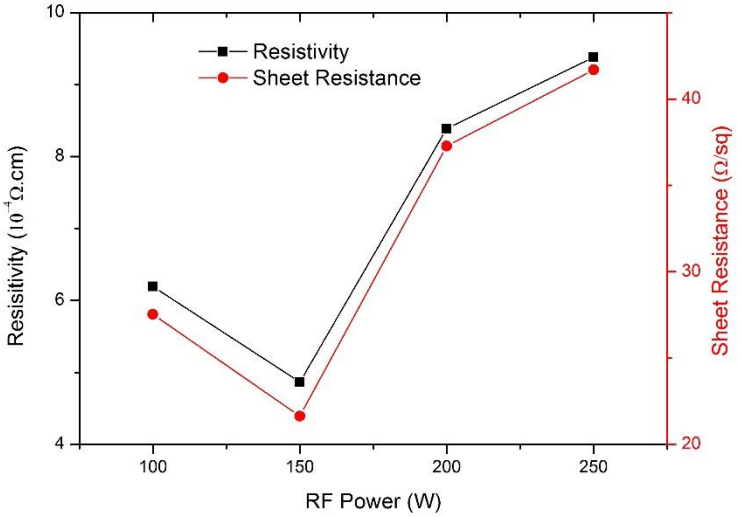

Figure 7.8: Variation of the resistivity and sheet resistance of 225 nm thick ITO films grown at various RF power.

7.3.3 Optical properties

Figure 7.9 shows the optical transmittance spectra of ITO films measured at different thicknesses in the wavelength range of 300-800nm. Samples were prepared at an RF power of 100 W. The average transmittance of all samples in the visible range is over 75% as shown in the inset of Figure 7.9.

With increasing the thickness from 75 to 225 nm, the average transmittance in the wavelength range of 400-800 nm decreased slowly. This decrease in transmission may be due to free carrier absorption that increases as the carrier density increases in the thicker films. Furthermore, all of the ITO films exhibit sharp absorption edge in the ultraviolet region, which may be associated with the direct transition of electrons between the conduction band and valence band. It is seen that the absorption edge shifts gradually to lower photon energy with an increase in the film thickness. It can also be seen that the transmittance in the visible region is influenced by the ITO film structure and surface

morphology. As the surface roughness increases with an increase in film thickness, there is a slight enhancement in surface scattering which results in a gradual drop in optical transmittance in the visible region.

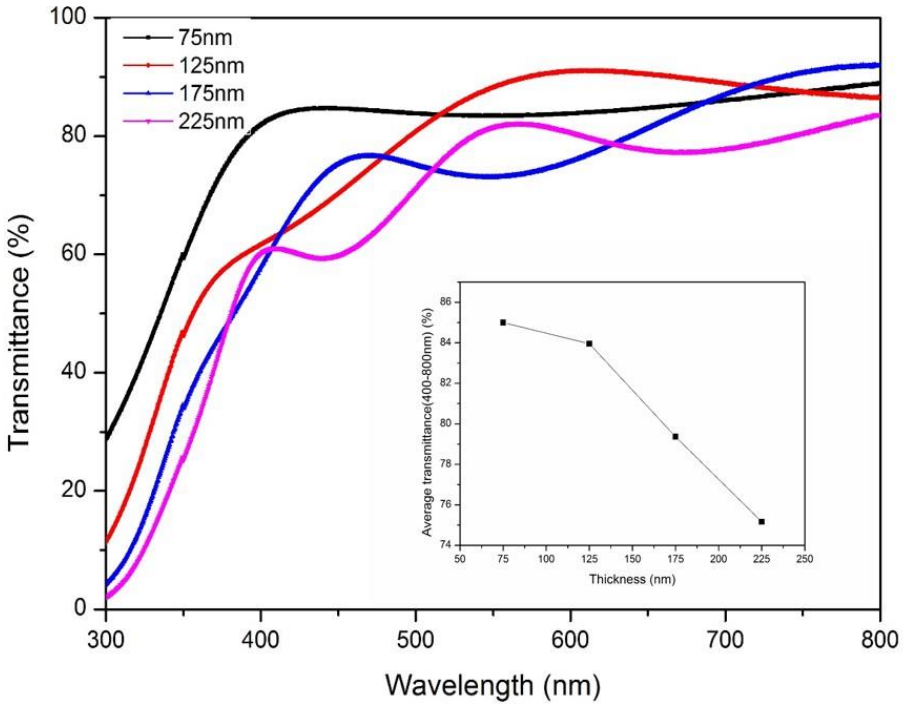

Figure 7.9: Optical transmittance of ITO film as a function of wavelength with different thicknesses at RF power of 100 W. Inset shows the average transmittance of those ITO film in the wavelength ranges from 400-800 nm.

The optical absorption coefficient (α) can be estimated using the following formula.

$$\alpha = \frac{\ln(1/T)}{t} \qquad (7.3)$$

Where T is the transmittance and t is the thickness of the film.

For a direct band semiconductor of allowed band to band transition, the optical energy band gap (E_g) of the thin films can be calculated by using the value of α in the following equation.

$$\alpha(h\upsilon) = A\left(h\upsilon - E_g\right)^{1/2} \qquad (7.4)$$

Where h is Planck's constant, υ is the frequency of the incident photon and A is constant. The optical energy band gap of the film is determined by plotting $(\alpha h\upsilon)^2$ as a function of photon energy ($h\upsilon$), and extrapolating the linear portions of $(\alpha h\upsilon)^2$ against photon energy ($h\upsilon$) where $(\alpha h\upsilon)^2$ is zero, then the photon energy is equal to the optical energy band gap.

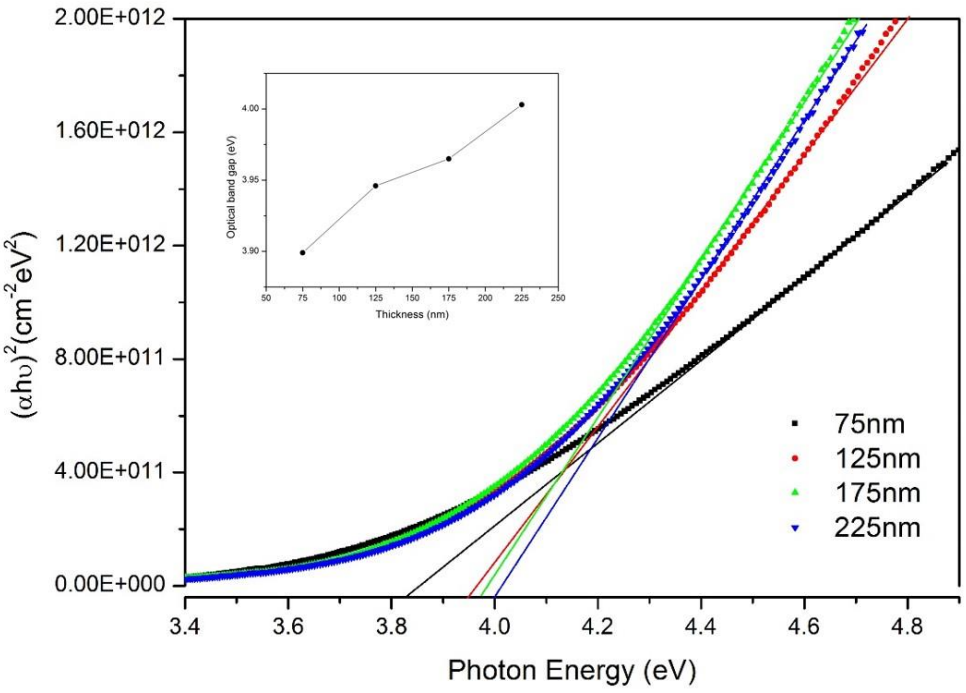

Figure 7.10: $(\alpha h\upsilon)^2$ against photon energy ($h\upsilon$) with different film thicknesses at RF power of 100 W. Inset shows Variation of optical band gap E_g of those ITO films.

Figure 7.10 illustrates the plots of $(\alpha h\upsilon)^2$ against photon energy ($h\upsilon$) with various film thicknesses at an RF power of 100 W. The inset in Figure 7.10 shows the dependence of optical energy band gap, E_g, on film thickness, and the value increases from 3.831 eV for 75 nm sample to 4.003 eV for the 225 nm sample. The fact that the increase in optical band gap is correlated to increase in carrier concentration with respect to increased film thickness could also be seen in Figure 7.5. This shift of the band gap can be explained by Burstein – Moss shift [211, 212]. Increasing the number of carriers with an increase in film thickness leads to shift in the Fermi level above the bottom of the conduction band, thereby causing an enlargement in the optical band gap of the ITO films.

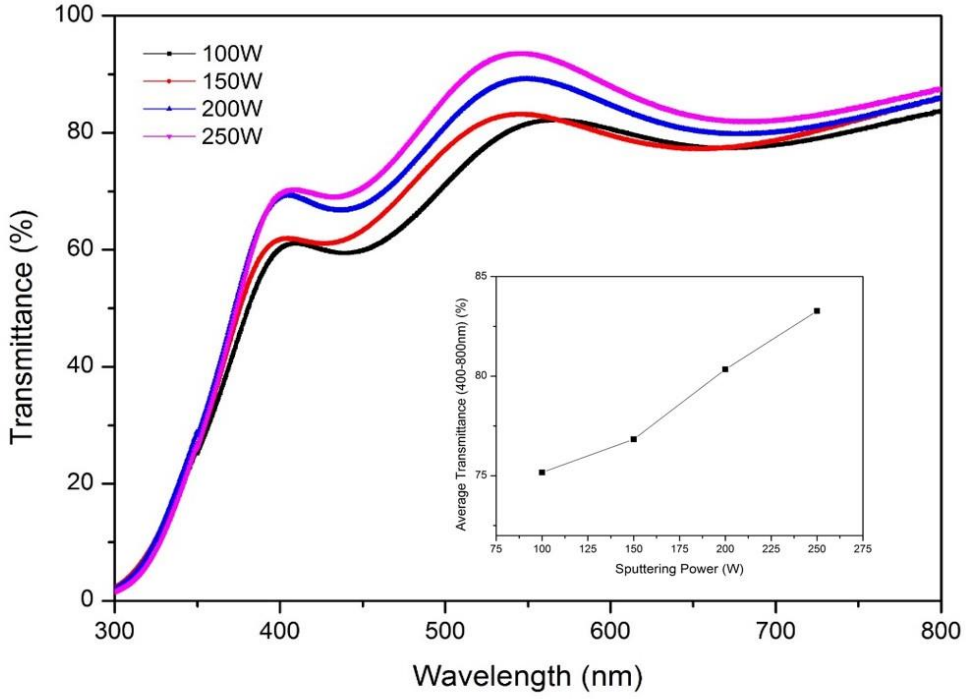

Figure 7.11: Optical transmittance of 225 nm thick ITO film as a function of wavelength with various RF power. The inset shows the average transmittance of those ITO film in the wavelength ranges from 400-800 nm.

The optical transmittance spectra of the 225 nm ITO film prepared with different RF power are shown in Figure 7.11 in the wavelength range of 300-800 nm. The average transmittance of all samples during the visible range is over 75%. With increasing RF power, the average transmittance in the wavelength range of 400-800 nm increases gradually from 75.2 % for 100 W sample to 83.3 % for 250 W sample.

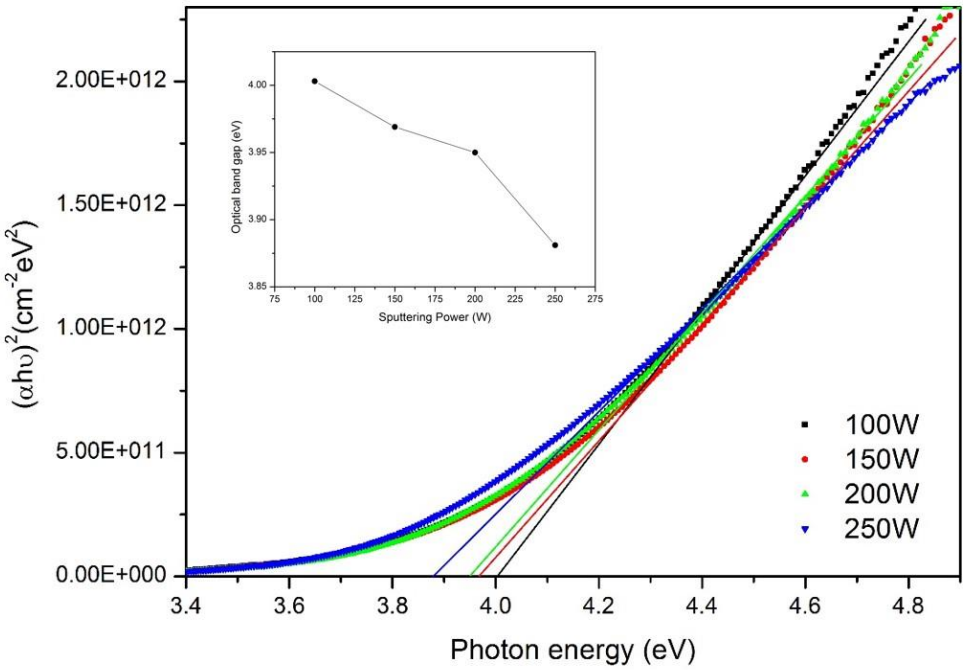

Figure 7.12: $(\alpha h\upsilon)^2$ against photon energy ($h\upsilon$) of 225 nm thick ITO film with various RF power. Inset shows variation of optical band gap E_g of those ITO films.

Figure 7.12 illustrates the plots of $(\alpha h\upsilon)^2$ against photon energy ($h\upsilon$) for the 225 nm thick ITO film with various RF powers. The inset in Figure 7.12 shows the variations of the optical energy band gap E_g as a function of RF power. The absorption edge shifts towards the higher energy as shown in Figure 7.11 and the energy gap drops from 4.003 eV to 3.881 eV upon increasing the RF power from 100 W to 250 W. These optical energy band gap values have a strong correlation with carrier concentration and shift in Fermi level, which influences the optical band gap.

For the photovoltaic applications, ITO thin films must have low resistivity and high optical transmittance. To obtain the best performance of transparent conducting films, the figure of merit ϕ_{TC}, proposed by Haacke [213], is given by

$$\phi_{TC} = {T^{10}}/{R_S} \qquad (7.5)$$

Where, T is the average optical transmittance and R_S is the sheet resistance of the films. The values of ϕ_{TC} for the ITO films with different thicknesses and RF sputtering powers are listed in Table 7.1.

Table 7.1: Thickness and RF sputtering power dependence of figure of merit values of ITO thin films.

RF Power (W)	Thickness (nm)	Average transmittance between 400-800nm (%)	Sheet Resistance (Ω/sq)	Figure of merit(ϕ_{TC}) ($\times 10^{-4}\ \Omega^{-1}$)
100	75	85.0	158.1	12.4
100	125	84.0	49.1	35.5
100	175	79.4	30.9	32.1
100	225	75.2	27.5	20.9
150	225	76.8	21.6	33.1
200	225	80.3	37.3	30.1
250	225	83.3	41.7	38.4

It can be seen that due to its high resistance, the75 nm thick ITO film prepared at 100 W RF power has a minimum ϕ_{TC} value. The highest value of ϕ_{TC} for films prepared at 100 W was obtained at a thickness of 125 nm. The overall optimum value of the figure of merit ϕ_{TC} is $38.4 \times 10^{-4}\ \Omega^{-1}$, this value was obtained for ITO film with a thickness of 225 nm and RF power of 250 W. This ITO film fulfills the optical and electrical requirements for efficient photovoltaic applications. The resistivity, optical

transmittance and carrier concentration of ITO thin films of this work are compared in Table 7.2 with previous reported works of ITO films prepared by different techniques.

Table 7.2: Comparison of values of electrical and optical properties for ITO thin films with previous reported works of ITO films prepared by different techniques.

Technique	**Thickness (nm)**	**Average transmittance between 400-800nm (%)**	**Resistivity (Ω.cm)**	**Carrier concentration (cm^{-3})**	**Reference**
RF magnetron sputtering	225	83.3	9.4×10^{-4}	6.1×10^{21}	In this work
Filtered cathodic vacuum arc deposition	50	95.0	6.57×10^{-4}	1.62×10^{21}	[214]
Pulsed laser deposition	400	85	2.4×10^{-3}	1.9×10^{20}	[197]
Ion beam sputtering	80	80	1.2×10^{-4}	2.3×10^{21}	[196]
Chemical vapor deposition	215	90	1.8×10^{-4}	3.4×10^{20}	[215]
RF magnetron sputtering	220	88	5.8×10^{-4}	3.4×10^{20}	[216]

7.3.4 Nanotextured ITO film for solar cells

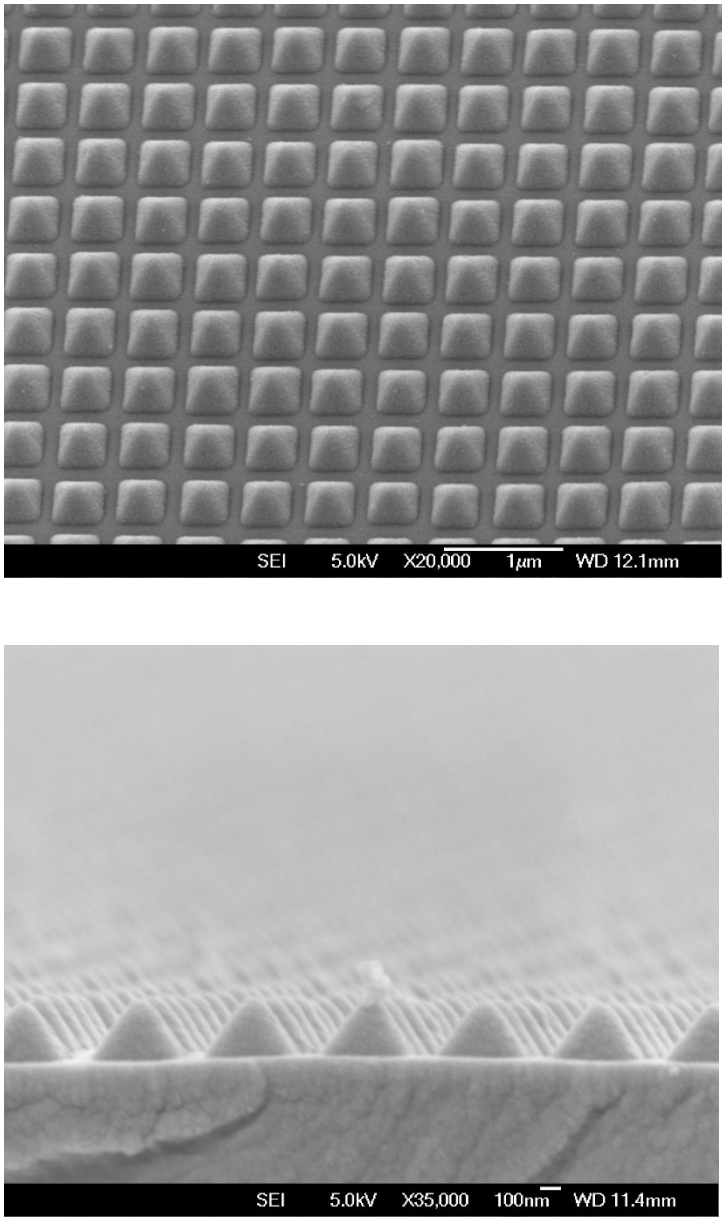

Figure 7.13: SEM images of ITO film deposited on upright nanopyramid structured glass substrate (a) top view and (b) cross-sectional view.

Figure 7.13 shows the top and cross-sectional view of the ITO film deposited on upright nanopyramid structured glass substrate at optimized conditions. The optimized values of the sputtering parameters can be found in the section 7.3.3. It can be clearly observed that

the ITO films were conformally coated the upright nanopyramid structured glass substrates.

Various light management scheme have been studied for enhancing light harvesting efficiencies in solar cells, such as anti-reflective coating [217], photonic crystals [218], Plasmonic nanostructures with periodic gratings [219], metal nanoparticles [220] and nanostructured transparent electrodes [221]. Nanostructured transparent electrodes have already been explored for a number of solar cells, such as organic based PV [222-224], perovskite [97] and thin film silicon solar cells [32, 93, 225, 226]. Such nanostructured transparent electrodes are intended to reduce the reflection and improve the light trapping properties.

Research on upright nanopyramid textured transparent electrodes for solar cells for enhanced light incoupling has not been demonstrated. Textured transparent electrodes have to fulfill a number of requirements on its electrical and optical properties, such as low resistivity and high optical transmittance in the relevant wavelength and light scattering features. As described in Chapter 5, upright nanopyramid structures offer a better-graded index medium to the incident light and possess strong light scattering properties. Therefore, the upright nanopyramid textured ITO electrode can be used for enhancing light harvesting efficiencies in organic, perovskite and thin film Si solar cells.

7.4 Summary

In this chapter, the surface morphological, optical and electrical properties of ITO thin films prepared by RF magnetron sputtering and the deposition of ITO films onto upright nanopyramid structured glass substrates were studied. The ITO films were prepared without introducing oxygen into the growth environment and deposited at different film thicknesses and RF powers at room temperature. This study reveals that both the electrical and optical properties are dependent on film thickness as well as sputtering RF power. AFM images of the ITO thin films reveal that surface roughness value increase with increasing the film thickness from 75 nm to 225 nm.

The grown ITO films exhibit low resistivity and high optical transmission in the visible region. The lowest sheet resistance of the ITO thin films obtained is 21.6 Ω/sq for 225 nm thickness deposited at 150 W RF power. The average optical transmittance (400-800 nm), carrier concentration, carrier mobility are 76.8 %, 10.6×10^{20} cm^{-3}, and 12.1 $cm^2/V.s$, respectively. For the photovoltaic applications, both excellent optical transmittance and high conductivity are required. The 225 m thickness ITO films prepared at 250 W RF power have a suitable figure of merits values, which exhibits 83.3 % average optical transmittance (400-800 nm), 9.4×10^{-4} Ω.cm resistivity, 6.1×10^{20} cm^{-3} carrier concentration and an 11 $cm^2/V.s$ carrier mobility.). Finally, the ITO films were conformally deposited onto upright nanopyramid structured glass substrate at optimized parameters. These nanostructured ITO electrodes are suitable for photovoltaic device applications with the potential to enhance the efficiency of different types of cells including organic, perovskite and thin film Si solar cells.

Chapter 8 Conclusions and future perspectives

8.1 Conclusions

Reducing optical losses in the solar cells has always been a key challenge in enhancing the power conversion efficiency of the solar cells without increasing the cost. In order to enhance the power conversion efficiency of the solar cells, a number of light trapping and antireflection schemes have been investigated to reduce the reflections and manipulate the light inside the absorber layer and to increase the effective optical path length of the light within the absorber layer of the solar cells. Optical optimizations on high performance c-Si solar cells have demonstrated that the inverted nanopyramid structures could be a more suitable candidate for an anti-reflection and light trapping due to their gradient refractive index tapered profile [60, 62, 227]. In addition, among all studied nanostructures, the inverted nanopyramid structures possess the advantages of achieving the desired function in a relatively low surface area and negligible surface damages, which reduces the electronic losses [67, 228]. It has also been demonstrated the effect of pyramid size on the reflectance over the wide wavelength range through optical simulation studies [61, 67]. It has been shown that as the feature size of the pyramid increases to the mid-wavelength, light absorption is enhanced over entire solar spectrum due to introduced better light coupling inside the solar cells.

In this work, periodic upright and inverted nanopyramid structures were explored as the light trapping nanostructures to improve the performance of the solar cells using UV nanoimprint lithography (UV-NIL). In addition, their superhydrophobic property was utilized to add a self-cleaning functionality to the front encapsulation.

Firstly, the inverted nanopyramid structures were fabricated on Si substrate by LIL and subsequent pattern transfer by combined reactive ion etching and KOH wet etching. Maskless LIL was employed as a high-throughput, high resolution and low cost technique for the fabrication of large scale periodic nanostructures. The pattern of nanoholes was recorded on AZMiR 701 i-line positive photoresist using LIL by double exposure. The CHF_3/Ar plasma etching was performed to transfer the nanoholes pattern into thin SiO_2 interlayer. Then, the O_2 plasma etching was performed to transfer the pattern into ARC layer with thin SiO_2 as a mask. After, the pattern was transferred into the thermal oxide layer using CHF_3/Ar plasma etching. The inverted pyramid structures were completely formed on Si substrate by KOH wet etching and the SiO_2 mask layer was removed by buffered HF etching.

The periodic inverted nanopyramid structures on a silicon substrate were used as a master mold substrate for the imprint process. In the first nanoimprint process, the upright nanopyramid structures with antireflective and hydrophobic properties were fabricated on the glass substrate by simple, high throughput and low cost UV nanoimprint lithography using Si master mold with inverted nanopyramid structures. The upright nanopyramid structures were fabricated on the OrmoStamp coated glass substrate using Si master mold with high fidelity. The upright nanopyramid structured glass substrate was used as protective cover glass for solar cells application and as a mold for the second imprint process.

The diffuse transmittance and haze ratio values were significantly increased for the upright nanopyramid patterned glass, especially, in the wavelength range 300-600 nm compared to the bare glass. This indicates that an antireflection and strong light scattering functions were achieved due to the upright nanopyramid structures. The use of upright nanopyramids patterned glass as a cover glass, the power conversion efficiency of the

encapsulated monocrystalline Si solar cell and commercially made polycrystalline Si solar cell were substantially enhanced by 10.888% and 8.216%, respectively. This is mainly due to the oblique scattering and prolonging the optical path length by the upright nanopyramid structures compared to the reference cells with bare glass. In addition, the fluorinated upright nanopyramid structured cover glass exhibited larger θ_{CA} ~132° and excellent self-cleaning properties for dust particles. This was confirmed by rolling down water droplets as compared with the bare cover glass (θ_{CA}~ 36°).

In the second nanoimprint process, the periodic inverted nanopyramid structures were fabricated on the monocrystalline solar cell and commercially made polycrystalline Si solar cell front surfaces using a UV nanoimprint lithography. The pyramid coating can be applied after cell fabrication to eliminate any losses due to surface damage by the etching processes. The inverted nanopyramid coating decreased the reflectance and increased the external quantum efficiency over a broad wavelength in the visible range. Reflection reduction can be explained by the nanostructured surfaces and the gradual change of the refractive index from air to Si. The gradual change of refractive index leads to a better light coupling inside the solar cells. It is also expected that light trapping is enhanced inside the solar cells since pyramidal tapered profile represents a gradual change from the uniform Si base to the periodic inverted nanopyramid structures at the apex. This allows the incident light to be coupled and guided inside the solar cells, resulting in an increased the effective optical path length of the light in the solar cells. The periodic inverted nanopyramid structures have successfully reduced the Fresnel reflection and led to directing and trapping the incident light into the monocrystalline and polycrystalline Si solar cells, thereby improving the short circuit current density from 29.442 $mAcm^{-2}$ to 32.793 $mAcm^{-2}$ and from 32.512 $mAcm^{-2}$ to 33.725 $mAcm^{-2}$ and enhancing the power conversion efficiency by 11.733% and 6.869%, respectively.

Moreover, the surface of the solar cells exhibited hydrophobic properties due to increased contact angle caused by the nanostructure patterns and the self-assembled monolayer coating. The enhanced hydrophobicity provided the solar cells with an added self-cleaning functionality.

These results also suggest that the periodic inverted nanopyramid and upright nanopyramid structures with light harvesting and self-cleaning properties have a considerable potential for various types of solar cells and optical systems in outdoor dusty environments.

Finally, the surface morphological, optical and electrical properties of ITO thin films prepared by RF magnetron sputtering and the fabrication of ITO films onto upright nanopyramid structured glass substrate were studied. The ITO films were prepared without introducing oxygen into the growth environment and deposited at different film thicknesses and RF powers at room temperature. This study reveals that both the electrical and optical properties are dependent on film thickness as well as sputtering RF power. AFM images of the ITO thin films reveal that surface roughness value increase with increasing the film thickness from 75 nm to 225 nm. The grown ITO films exhibit low resistivity and high optical transmission in the visible region. For the photovoltaic applications, both excellent optical transmittance and high conductivity are required. The 225 m thickness ITO films prepared at 250 W RF power have a suitable figure of merits values, which exhibits 83.3 % average optical transmittance (400-800 nm), 9.4×10^{-4} Ω.cm resistivity, 6.1×10^{20} cm^{-3} carrier concentration and an 11 $cm^2/V.s$ carrier mobility. The ITO films were conformally deposited onto upright nanopyramid structured glass substrate at optimized parameters. These nanostructured ITO electrodes are suitable for photovoltaic device applications to enhance the efficiency of organic, perovskite and thin film Si solar cells.

8.2 Future perspectives

This thesis has provided the methodologies to fabricate periodic nanopyramids structured glass substrates with multifunctional properties which can be applied as a protective cover glass and on the top and back side texturing to improve the performance of solar cells. However, further optimizing of the light trapping schemes and solar cells design to enable higher performance at low cost is still required. Some suggestions for future research and development are presented as follows:

8.2.1 Plasmonic nanostructures

The plasmonic back reflectors have been utilized for light trapping in thin film solar cells, which can be incorporated with the metal back reflector in a standard solar cell design. The integrated plasmonic nanostructures can couple the light into photonic modes or surface plasmon polariton (SPP) modes at the metal-semiconductor interfaces [229, 230]. It has been demonstrated that the performance of the solar cells can be enhanced by integrating the nanostructured back reflector into solar cells [160, 231, 232]. A variety of nanostructures, such as nanocones [178], nanodome [233], nanovoid [234], and nanocylinder-induced conformal structures [231], have been commonly used for plasmonic back reflectors for a-Si thin film solar cells. In the a-Si solar cell design, Ag can be deposited on the periodic upright nanopyramid structured glass substrate and implemented as a metal back reflector substrate for solar cells. This upright nanopyramid structured solar cell would provide several enhancement mechanisms.

8.2.2 Light trapping with dielectric nanoparticles and nanostructures

To avoid the inherent losses associated with metallic nanoparticles, dielectric nanoparticles have been extensively employed in solar cells, due to the almost negligible absorption loss in the visible to near infrared range and broadband scattering, which is useful to enhance the performance of the solar cells [235, 236]. Also, the refractive indices of the dielectric nanoparticles are normally from 1.5 to 2.0 making them potential candidates for antireflection components in the solar cell design, in particular, when they are integrated on the top side of solar cells. As discussed in Chapter 6, the power conversion efficiency of the solar cells was enhanced by incorporating the periodic inverted nanopyramid structures on the front side of the solar cells. The dielectric nanoparticles can be incorporated into the nanopyramid structures, which can further enhance the efficiency of the solar cells.

8.2.3 Nanophotonic transparent front electrodes for perovskite solar cells

Nanophotonic transparent electrodes have already been explored for a perovskite solar cells [97]. Such nanostructured transparent electrodes are intended to reduce the reflection at the interfaces of the front electrode and to improve the light trapping, resulting in an increase the effective optical path length of the light in the photoactive material. Research on upright nanopyramid textured transparent electrodes for solar cells for enhanced light incoupling has not been demonstrated. The transparent nanopyramid structured front electrodes can be fabricated as described in Chapter 7, section 7.3.4, and used for improved light incoupling in perovskite solar cells.

References

[1] U. E. I. Administration. (2016). *INTERNATIONAL ENERGY OUTLOOK 2016*. Available: http://www.eia.gov/outlooks/ieo/world.cfm

[2] I. E. Agency. (2016). *Key World Energy Statistics 2016*. Available: https://www.iea.org/publications/freepublications/publication/KeyWorld2016.pdf

[3] I. E. Agency. (2014). *Technology Roadmap Solar Photovoltaic Energy*. Available: https://www.iea.org/publications/freepublications/publication/TechnologyRoadmapSolarPhotovoltaicEnergy_2014edition.pdf

[4] F. ISE. (2016). *PHOTOVOLTAICS REPORT*. Available: https://www.ise.fraunhofer.de/de/downloads/pdf-files/aktuelles/photovoltaics-report-in-englischer-sprache.pdf

[5] C. Battaglia, C.-M. Hsu, K. Söderström, J. Escarré, F.-J. Haug, M. Charrière, *et al.*, "Light trapping in solar cells: can periodic beat random?," *ACS nano*, vol. 6, pp. 2790-2797, 2012.

[6] J. Zhu, C.-M. Hsu, Z. Yu, S. Fan, and Y. Cui, "Nanodome solar cells with efficient light management and self-cleaning," *Nano letters*, vol. 10, pp. 1979-1984, 2009.

[7] E. Garnett and P. Yang, "Light trapping in silicon nanowire solar cells," *Nano letters*, vol. 10, pp. 1082-1087, 2010.

[8] Y. Kuang, K. H. Van der Werf, Z. S. Houweling, and R. E. Schropp, "Nanorod solar cell with an ultrathin a-Si: H absorber layer," *Applied physics letters*, vol. 98, p. 113111, 2011.

[9] H.-C. Chang, K.-Y. Lai, Y.-A. Dai, H.-H. Wang, C.-A. Lin, and J.-H. He, "Nanowire arrays with controlled structure profiles for maximizing optical collection efficiency," *Energy & Environmental Science*, vol. 4, pp. 2863-2869, 2011.

[10] K. S. Cho, P. Mandal, K. Kim, I. H. Baek, S. Lee, H. Lim, *et al.*, "Improved efficiency in GaAs solar cells by 1D and 2D nanopatterns fabricated by laser interference lithography," *Optics Communications*, vol. 284, pp. 2608-2612, 2011.

[11] J. Kim, A. J. Hong, J.-W. Nah, B. Shin, F. M. Ross, and D. K. Sadana, "Three-dimensional a-Si: H solar cells on glass nanocone arrays patterned by self-assembled Sn nanospheres," *ACS nano*, vol. 6, pp. 265-271, 2011.

[12] C. Battaglia, J. Escarré, K. Söderström, M. Charrière, M. Despeisse, F.-J. Haug, *et al.*, "Nanomoulding of transparent zinc oxide electrodes for efficient light trapping in solar cells," *Nature Photonics*, vol. 5, pp. 535-538, 2011.

[13] C.-A. Lin, M.-L. Tsai, W.-R. Wei, K.-Y. Lai, and J.-H. He, "Packaging Glass with a Hierarchically Nanostructured Surface: A Universal Method to Achieve Self-Cleaning Omnidirectional Solar Cells," *ACS nano*, vol. 10, pp. 549-555, 2015.

[14] H. J. Gwon, Y. Park, C. W. Moon, S. Nahm, S.-J. Yoon, S. Y. Kim, *et al.*, "Superhydrophobic and antireflective nanograss-coated glass for high performance solar cells," *Nano Research*, vol. 7, pp. 670-678, 2014.

[15] Y. Song, R. P. Nair, M. Zou, and Y. Wang, "Superhydrophobic surfaces produced by applying a self-assembled monolayer to silicon micro/nano-textured surfaces," *Nano Research*, vol. 2, pp. 143-150, 2009.

[16] Y.-B. Park, H. Im, M. Im, and Y.-K. Choi, "Self-cleaning effect of highly water-repellent microshell structures for solar cell applications," *Journal of Materials Chemistry*, vol. 21, pp. 633-636, 2011.

[17] L. K. Verma, M. Sakhuja, J. Son, A. Danner, H. Yang, H. Zeng, *et al.*, "Self-cleaning and antireflective packaging glass for solar modules," *Renewable Energy*, vol. 36, pp. 2489-2493, 2011.

[18] P. Campbell and M. A. Green, "Light trapping properties of pyramidally textured surfaces," *Journal of Applied Physics*, vol. 62, pp. 243-249, 1987.

[19] A. Smith and A. Rohatgi, "Ray tracing analysis of the inverted pyramid texturing geometry for high efficiency silicon solar cells," *Solar energy materials and solar cells*, vol. 29, pp. 37-49, 1993.

[20] K. Kim, S. Dhungel, S. Jung, D. Mangalaraj, and J. Yi, "Texturing of large area multi-crystalline silicon wafers through different chemical approaches for solar cell fabrication," *Solar Energy Materials and Solar Cells*, vol. 92, pp. 960-968, 2008.

[21] D. Macdonald, A. Cuevas, M. J. Kerr, C. Samundsett, D. Ruby, S. Winderbaum, *et al.*, "Texturing industrial multicrystalline silicon solar cells," *Solar Energy*, vol. 76, pp. 277-283, 2004.

[22] G. Kumaravelu, M. Alkaisi, A. Bittar, D. Macdonald, and J. Zhao, "Damage studies in dry etched textured silicon surfaces," *Current Applied Physics*, vol. 4, pp. 108-110, 2004.

[23] S. Chattopadhyay, Y. Huang, Y.-J. Jen, A. Ganguly, K. Chen, and L. Chen, "Anti-reflecting and photonic nanostructures," *Materials Science and Engineering: R: Reports*, vol. 69, pp. 1-35, 2010.

[24] Y. Li, J. Zhang, and B. Yang, "Antireflective surfaces based on biomimetic nanopillared arrays," *Nano Today*, vol. 5, pp. 117-127, 2010.

[25] Z. Yu, A. Raman, and S. Fan, "Fundamental limit of nanophotonic light trapping in solar cells," *Proceedings of the National Academy of Sciences*, vol. 107, pp. 17491-17496, 2010.

[26] C. Eisele, C. Nebel, and M. Stutzmann, "Periodic light coupler gratings in amorphous thin film solar cells," *Journal of Applied Physics*, vol. 89, pp. 7722-7726, Jun 15 2001.

[27] L. Zeng, Y. Yi, C. Hong, J. Liu, N. Feng, X. Duan, *et al.*, "Efficiency enhancement in Si solar cells by textured photonic crystal back reflector," *Applied Physics Letters*, vol. 89, p. 111111, 2006.

[28] X. Sheng, S. G. Johnson, J. Michel, and L. C. Kimerling, "Optimization-based design of surface textures for thin-film Si solar cells," *Optics express*, vol. 19, pp. A841-A850, 2011.

[29] R. Biswas, J. Bhattacharya, B. Lewis, N. Chakravarty, and V. Dalal, "Enhanced nanocrystalline silicon solar cell with a photonic crystal back-reflector," *Solar Energy Materials and Solar Cells*, vol. 94, pp. 2337-2342, 2010.

[30] X. Sheng, J. Liu, I. Kozinsky, A. M. Agarwal, J. Michel, and L. C. Kimerling, "Design and non-lithographic fabrication of light trapping structures for thin film silicon solar cells," *Advanced Materials*, vol. 23, pp. 843-847, 2011.

[31] J. Li, H. Yu, Y. Li, F. Wang, M. Yang, and S. M. Wong, "Low aspect-ratio hemispherical nanopit surface texturing for enhancing light absorption in crystalline Si thin film-based solar cells," *Applied Physics Letters*, vol. 98, p. 021905, 2011.

[32] C. Battaglia, C.-M. Hsu, K. Söderström, J. Escarre, F.-J. Haug, M. Charrière, *et al.*, "Light trapping in solar cells: can periodic beat random?," *ACS nano*, vol. 6, pp. 2790-2797, 2012.

[33] P. Bermel, C. Luo, L. Zeng, L. C. Kimerling, and J. D. Joannopoulos, "Improving thin-film crystalline silicon solar cell efficiencies with photonic crystals," *Optics express,* vol. 15, pp. 16986-17000, 2007.

[34] M. Law, L. E. Greene, J. C. Johnson, R. Saykally, and P. Yang, "Nanowire dye-sensitized solar cells," *Nature materials,* vol. 4, pp. 455-459, 2005.

[35] J. Wallentin, N. Anttu, D. Asoli, M. Huffman, I. Åberg, M. H. Magnusson, *et al.*, "InP nanowire array solar cells achieving 13.8% efficiency by exceeding the ray optics limit," *Science,* vol. 339, pp. 1057-1060, 2013.

[36] O. L. Muskens, J. G. Rivas, R. E. Algra, E. P. Bakkers, and A. Lagendijk, "Design of light scattering in nanowire materials for photovoltaic applications," *Nano letters,* vol. 8, pp. 2638-2642, 2008.

[37] C. Battaglia, K. Söderström, J. Escarre, F.-J. Haug, D. Domine, P. Cuony, *et al.*, "Efficient light management scheme for thin film silicon solar cells via transparent random nanostructures fabricated by nanoimprinting," *Applied Physics Letters,* vol. 96, p. 213504, 2010.

[38] S. H. Zaidi, D. S. Ruby, and J. M. Gee, "Characterization of random reactive ion etched-textured silicon solar cells," *IEEE Transactions on Electron Devices,* vol. 48, pp. 1200-1206, 2001.

[39] V. E. Ferry, L. A. Sweatlock, D. Pacifici, and H. A. Atwater, "Plasmonic nanostructure design for efficient light coupling into solar cells," *Nano letters,* vol. 8, pp. 4391-4397, 2008.

[40] R. A. Pala, J. White, E. Barnard, J. Liu, and M. L. Brongersma, "Design of plasmonic thin-film solar cells with broadband absorption enhancements," *Advanced Materials,* vol. 21, pp. 3504-3509, 2009.

[41] M. J. Mendes, S. Morawiec, T. Mateus, A. Lyubchyk, H. Águas, I. Ferreira, *et al.*, "Broadband light trapping in thin film solar cells with self-organized plasmonic nano-colloids," *Nanotechnology,* vol. 26, p. 135202, 2015.

[42] H. Hauser, "Nanoimprint lithography for solar cell texturisation," Dissertation, Albert-Ludwigs-Universität Freiburg, 2013, 2013.

[43] F. Wu, G. Shi, H. Xu, L. Liu, Y. Wang, D. Qi, *et al.*, "Fabrication of antireflective compound eyes by imprinting," *ACS applied materials & interfaces,* vol. 5, pp. 12799-12803, 2013.

[44] K. R. Catchpole, S. Mokkapati, F. Beck, E.-C. Wang, A. McKinley, A. Basch, *et al.*, "Plasmonics and nanophotonics for photovoltaics," *MRS bulletin,* vol. 36, pp. 461-467, 2011.

[45] S. Mokkapati and K. Catchpole, "Nanophotonic light trapping in solar cells," *Journal of Applied Physics,* vol. 112, p. 101101, Nov 15 2012.

[46] Y. Kanamori, M. Sasaki, and K. Hane, "Broadband antireflection gratings fabricated upon silicon substrates," *Optics Letters,* vol. 24, pp. 1422-1424, Oct 15 1999.

[47] K. H. Tsui, Q. Lin, H. Chou, Q. Zhang, H. Fu, P. Qi, *et al.*, "Low-Cost, Flexible, and Self-Cleaning 3D Nanocone Anti-Reflection Films for High-Efficiency Photovoltaics," *Advanced Materials,* vol. 26, pp. 2805-2811, 2014.

[48] S. Jeong, E. C. Garnett, S. Wang, Z. Yu, S. Fan, M. L. Brongersma, *et al.*, "Hybrid silicon nanocone–polymer solar cells," *Nano letters,* vol. 12, pp. 2971-2976, 2012.

[49] S. Jeong, M. D. McGehee, and Y. Cui, "All-back-contact ultra-thin silicon nanocone solar cells with 13.7% power conversion efficiency," *Nature communications,* vol. 4, 2013.

[50] B. Wang and P. W. Leu, "Enhanced absorption in silicon nanocone arrays for photovoltaics," *Nanotechnology,* vol. 23, p. 194003, 2012.

[51] Y. Lu and A. Lal, "High-efficiency ordered silicon nano-conical-frustum array solar cells by self-powered parallel electron lithography," *Nano letters,* vol. 10, pp. 4651-4656, 2010.

[52] D.-S. Tsai, C.-A. Lin, W.-C. Lien, H.-C. Chang, Y.-L. Wang, and J.-H. He, "Ultra-high-responsivity broadband detection of Si metal–semiconductor–metal schottky photodetectors improved by ZnO nanorod arrays," *ACS nano,* vol. 5, pp. 7748-7753, 2011.

[53] Y.-R. Lin, H.-P. Wang, C.-A. Lin, and J.-H. He, "Surface profile-controlled close-packed Si nanorod arrays for self-cleaning antireflection coatings," *Journal of applied physics,* vol. 106, p. 114310, 2009.

[54] Q. Lin, B. Hua, S.-f. Leung, X. Duan, and Z. Fan, "Efficient light absorption with integrated nanopillar/nanowell arrays for three-dimensional thin-film photovoltaic applications," *ACS nano,* vol. 7, pp. 2725-2732, 2013.

[55] Z. Fan, H. Razavi, J.-w. Do, A. Moriwaki, O. Ergen, Y.-L. Chueh, *et al.*, "Three-dimensional nanopillar-array photovoltaics on low-cost and flexible substrates," *Nature materials,* vol. 8, pp. 648-653, 2009.

[56] R. Kapadia, Z. Fan, K. Takei, and A. Javey, "Nanopillar photovoltaics: materials, processes, and devices," *Nano Energy*, vol. 1, pp. 132-144, 2012.

[57] S.-F. Leung, M. Yu, Q. Lin, K. Kwon, K.-L. Ching, L. Gu, *et al.*, "Efficient photon capturing with ordered three-dimensional nanowell arrays," *Nano letters*, vol. 12, pp. 3682-3689, 2012.

[58] S. E. Han and G. Chen, "Optical absorption enhancement in silicon nanohole arrays for solar photovoltaics," *Nano letters*, vol. 10, pp. 1012-1015, 2010.

[59] K.-Q. Peng, X. Wang, L. Li, X.-L. Wu, and S.-T. Lee, "High-performance silicon nanohole solar cells," *Journal of the American Chemical Society*, vol. 132, pp. 6872-6873, 2010.

[60] A. Mavrokefalos, S. E. Han, S. Yerci, M. S. Branham, and G. Chen, "Efficient light trapping in inverted nanopyramid thin crystalline silicon membranes for solar cell applications," *Nano letters*, vol. 12, pp. 2792-2796, 2012.

[61] S. Sivasubramaniam and M. M. Alkaisi, "Inverted nanopyramid texturing for silicon solar cells using interference lithography," *Microelectronic Engineering*, vol. 119, pp. 146-150, 2014.

[62] G. Li, H. Li, J. Y. Ho, M. Wong, and H. S. Kwok, "Nanopyramid structure for ultrathin c-Si tandem solar cells," *Nano letters*, vol. 14, pp. 2563-2568, 2014.

[63] A. Gaucher, A. Cattoni, C. Dupuis, W. Chen, R. Cariou, M. Foldyna, *et al.*, "Ultrathin epitaxial silicon solar cells with inverted nanopyramid arrays for efficient light trapping," *Nano Letters*, vol. 16, pp. 5358-5364, 2016.

[64] J. Grandidier, D. M. Callahan, J. N. Munday, and H. A. Atwater, "Light Absorption Enhancement in Thin-Film Solar Cells Using Whispering Gallery Modes in Dielectric Nanospheres," *Advanced Materials*, vol. 23, pp. 1272-1276, 2011.

[65] Y. Yao, J. Yao, V. K. Narasimhan, Z. Ruan, C. Xie, S. Fan, *et al.*, "Broadband light management using low-Q whispering gallery modes in spherical nanoshells," *Nature communications*, vol. 3, p. 664, 2012.

[66] K. X. Wang, Z. Yu, V. Liu, Y. Cui, and S. Fan, "Absorption enhancement in ultrathin crystalline silicon solar cells with antireflection and light-trapping nanocone gratings," *Nano letters*, vol. 12, pp. 1616-1619, 2012.

[67] S. Zhou, Z. Yang, P. Gao, X. Li, X. Yang, D. Wang, *et al.*, "Wafer-Scale Integration of Inverted Nanopyramid Arrays for Advanced Light Trapping in

Crystalline Silicon Thin Film Solar Cells," *Nanoscale research letters,* vol. 11, p. 1, 2016.

[68] S. A. Maier and H. A. Atwater, "Plasmonics: Localization and guiding of electromagnetic energy in metal/dielectric structures," *Journal of Applied Physics,* vol. 98, p. 011101, Jul 1 2005.

[69] F. Beck, S. Mokkapati, and K. Catchpole, "Nanoplasmonics for Light Trapping in Solar Cells," *Nanotechnology in Australia: Showcase of Early Career Research,* p. 41, 2011.

[70] H. A. Atwater and A. Polman, "Plasmonics for improved photovoltaic devices," *Nat Mater,* vol. 9, pp. 205-13, Mar 2010.

[71] C. Eminian, F. J. Haug, O. Cubero, X. Niquille, and C. Ballif, "Photocurrent enhancement in thin film amorphous silicon solar cells with silver nanoparticles," *Progress in Photovoltaics: Research and Applications,* vol. 19, pp. 260-265, 2011.

[72] H. Tan, R. Santbergen, A. H. Smets, and M. Zeman, "Plasmonic light trapping in thin-film silicon solar cells with improved self-assembled silver nanoparticles," *Nano letters,* vol. 12, pp. 4070-4076, 2012.

[73] V. E. Ferry, M. A. Verschuuren, H. B. Li, R. E. Schropp, H. A. Atwater, and A. Polman, "Improved red-response in thin film a-Si: H solar cells with soft-imprinted plasmonic back reflectors," *Applied Physics Letters,* vol. 95, p. 183503, 2009.

[74] C. Hägglund, M. Zäch, G. Petersson, and B. Kasemo, "Electromagnetic coupling of light into a silicon solar cell by nanodisk plasmons," *Applied Physics Letters,* vol. 92, p. 053110, 2008.

[75] M. Totzeck, W. Ulrich, A. Göhnermeier, and W. Kaiser, "Semiconductor fabrication: Pushing deep ultraviolet lithography to its limits," *nature photonics,* vol. 1, pp. 629-631, 2007.

[76] L. Müller-Meskamp, Y. H. Kim, T. Roch, S. Hofmann, R. Scholz, S. Eckardt, *et al.*, "Efficiency enhancement of organic solar cells by fabricating periodic surface textures using direct laser interference patterning," *Advanced Materials,* vol. 24, pp. 906-910, 2012.

[77] K.-S. Han, J.-H. Shin, W.-Y. Yoon, and H. Lee, "Enhanced performance of solar cells with anti-reflection layer fabricated by nano-imprint lithography," *Solar Energy Materials and Solar Cells,* vol. 95, pp. 288-291, 2011.

[78] A. Kosiorek, W. Kandulski, H. Glaczynska, and M. Giersig, "Fabrication of nanoscale rings, dots, and rods by combining shadow nanosphere lithography and annealed polystyrene nanosphere masks," *Small*, vol. 1, pp. 439-444, 2005.

[79] H. Fredriksson, Y. Alaverdyan, A. Dmitriev, C. Langhammer, D. S. Sutherland, M. Zäch, *et al.*, "Hole–mask colloidal lithography," *Advanced Materials*, vol. 19, pp. 4297-4302, 2007.

[80] L. J. Guo, "Nanoimprint lithography: methods and material requirements," *Advanced Materials*, vol. 19, pp. 495-513, 2007.

[81] M. G. Kang, M. S. Kim, J. Kim, and L. J. Guo, "Organic solar cells using nanoimprinted transparent metal electrodes," *Advanced Materials*, vol. 20, pp. 4408-4413, 2008.

[82] C. Vieu, F. Carcenac, A. Pepin, Y. Chen, M. Mejias, A. Lebib, *et al.*, "Electron beam lithography: resolution limits and applications," *Applied Surface Science*, vol. 164, pp. 111-117, 2000.

[83] M. D. Stewart and C. G. Willson, "Imprint materials for nanoscale devices," *MRS bulletin*, vol. 30, pp. 947-951, 2005.

[84] M. Colburn, S. C. Johnson, M. D. Stewart, S. Damle, T. C. Bailey, B. Choi, *et al.*, "Step and flash imprint lithography: a new approach to high-resolution patterning," in *Microlithography'99*, 1999, pp. 379-389.

[85] S. Y. Chou, C. Keimel, and J. Gu, "Ultrafast and direct imprint of nanostructures in silicon," *Nature*, vol. 417, pp. 835-7, Jun 20 2002.

[86] M. Tormen, "Microcontact printing techniques," in *Alternative Lithography*, ed: Springer, 2003, pp. 181-212.

[87] L.-R. Bao, X. Cheng, X. Huang, L. Guo, S. Pang, and A. Yee, "Nanoimprinting over topography and multilayer three-dimensional printing," *Journal of Vacuum Science & Technology B*, vol. 20, pp. 2881-2886, Nov-Dec 2002.

[88] J. Ahopelto and T. Haatainen, "Step and stamp imprint lithography," in *Alternative Lithography*, ed: Springer, 2003, pp. 103-115.

[89] J.-Y. Chen, M.-H. Yu, C.-Y. Chang, Y.-H. Chao, K. W. Sun, and C.-S. Hsu, "Enhanced performance of organic thin film solar cells using electrodes with nanoimprinted light-diffraction and light-diffusion structures," *ACS applied materials & interfaces*, vol. 6, pp. 6164-6169, 2014.

[90] P. Wangyang, Y. Gan, Q. Wang, and X. Jiang, "A hybrid resist hemispherical-pit array layer for light trapping in thin film silicon solar cells via UV nanoimprint lithography," *Journal of Materials Chemistry C*, vol. 2, pp. 6140-6147, 2014.

[91] K. Wilken, U. Paetzold, M. Meier, N. Prager, M. Fahland, F. Finger, *et al.*, "Improved flexible thin-film solar cells with nanoimprinted light management textures," in *Photovoltaic Specialist Conference (PVSC), 2015 IEEE 42nd*, 2015, pp. 1-3.

[92] W. Yan, Z. Tao, T. M. B. Ong, and M. Gu, "Highly efficient ultrathin-film amorphous silicon solar cells on top of imprinted periodic nanodot arrays," *Applied Physics Letters*, vol. 106, p. 093902, 2015.

[93] C. Battaglia, J. Escarré, K. Söderström, L. Erni, L. Ding, G. Bugnon, *et al.*, "Nanoimprint lithography for high-efficiency thin-film silicon solar cells," *Nano letters*, vol. 11, pp. 661-665, 2010.

[94] K. Wilken, U. W. Paetzold, M. Meier, N. Prager, M. Fahland, F. Finger, *et al.*, "Nanoimprint texturing of transparent flexible substrates for improved light management in thin-film solar cells," *physica status solidi (RRL)-Rapid Research Letters*, vol. 9, pp. 215-219, 2015.

[95] J. D. Chen, L. Zhou, Q. D. Ou, Y. Q. Li, S. Shen, S. T. Lee, *et al.*, "Enhanced Light Harvesting in Organic Solar Cells Featuring a Biomimetic Active Layer and a Self-Cleaning Antireflective Coating," *Advanced Energy Materials*, vol. 4, 2014.

[96] S. H. Lee, K. S. Han, J. H. Shin, S. Y. Hwang, and H. Lee, "Fabrication of highly transparent self-cleaning protection films for photovoltaic systems," *Progress in Photovoltaics: Research and Applications*, vol. 21, pp. 1056-1062, 2013.

[97] U. W. Paetzold, W. Qiu, F. Finger, J. Poortmans, and D. Cheyns, "Nanophotonic front electrodes for perovskite solar cells," *Applied physics letters*, vol. 106, p. 173101, 2015.

[98] M. Meier, U. W. Paetzold, M. Prömpers, T. Merdzhanova, R. Carius, and A. Gordijn, "UV nanoimprint for the replication of etched ZnO: Al textures applied in thin-film silicon solar cells," *Progress in Photovoltaics: Research and Applications*, vol. 22, pp. 1226-1236, 2014.

[99] K.-S. Han, J.-H. Shin, and H. Lee, "Enhanced transmittance of glass plates for solar cells using nano-imprint lithography," *Solar Energy Materials and Solar Cells,* vol. 94, pp. 583-587, 2010.

[100] F. Jiao, Q. Huang, W. Ren, W. Zhou, F. Qi, Y. Zheng, *et al.*, "Enhanced performance for solar cells with moth-eye structure fabricated by UV nanoimprint lithography," *Microelectronic Engineering,* vol. 103, pp. 126-130, 2013.

[101] H.-C. Kim, S.-M. Park, and W. D. Hinsberg, "Block copolymer based nanostructures: materials, processes, and applications to electronics," *Chemical reviews,* vol. 110, pp. 146-177, 2009.

[102] Y. Li, N. Koshizaki, and W. Cai, "Periodic one-dimensional nanostructured arrays based on colloidal templates, applications, and devices," *Coordination Chemistry Reviews,* vol. 255, pp. 357-373, 2011.

[103] A. I. Hochbaum and J. Aizenberg, "Bacteria pattern spontaneously on periodic nanostructure arrays," *Nano letters,* vol. 10, pp. 3717-3721, 2010.

[104] H. D. Tong, H. V. Jansen, V. J. Gadgil, C. G. Bostan, E. Berenschot, C. J. van Rijn, *et al.*, "Silicon nitride nanosieve membrane," *Nano letters,* vol. 4, pp. 283-287, Feb 2004.

[105] S. Sivasubramaniam, A. Faramus, R. D. Tilley, and M. M. Alkaisi, "Performance enhancement in silicon solar cell by inverted nanopyramid texturing and silicon quantum dots coating," *Journal of Renewable and Sustainable Energy,* vol. 6, p. 011204, 2014.

[106] Z. Yu, H. Gao, W. Wu, H. Ge, and S. Y. Chou, "Fabrication of large area subwavelength antireflection structures on Si using trilayer resist nanoimprint lithography and liftoff," *Journal of Vacuum Science & Technology B,* vol. 21, pp. 2874-2877, Nov-Dec 2003.

[107] H. Y. Low, "Complex and useful polymer micro-and nanostructures via nanoimprint lithography," *International journal of nanotechnology,* vol. 4, pp. 389-403, 2007.

[108] J. C. Hulteen and R. P. Van Duyne, "Nanosphere lithography: a materials general fabrication process for periodic particle array surfaces," *Journal of Vacuum Science & Technology A,* vol. 13, pp. 1553-1558, May-Jun 1995.

[109] J. Y. Cheng, C. A. Ross, E. L. Thomas, H. I. Smith, and G. J. Vancso, "Fabrication of nanostructures with long-range order using block copolymer lithography," *Applied Physics Letters,* vol. 81, pp. 3657-3659, Nov 4 2002.

[110] L. R. Harriott, "Limits of lithography," *Proceedings of the IEEE,* vol. 89, pp. 366-374, 2001.

[111] H. Guo, D. Nau, A. Radke, X. Zhang, J. Stodolka, X. Yang, *et al.*, "Large-area metallic photonic crystal fabrication with interference lithography and dry etching," *Applied Physics B,* vol. 81, pp. 271-275, 2005.

[112] Y. Zhou, X. Chen, Y. Fu, G. Vienne, A. Kuznetsov, and B. Luk'yanchuk, "Fabrication of large-area 3D optical fishnet metamaterial by laser interference lithography," *Applied Physics Letters,* vol. 103, p. 123116, 2013.

[113] C. Lu and R. Lipson, "Interference lithography: a powerful tool for fabricating periodic structures," *Laser & Photonics Reviews,* vol. 4, pp. 568-580, 2010.

[114] M. O'Brien Ii, P. Bisong, L. Ista, E. Rabinovich, A. Garcia, S. Sibbett, *et al.*, "Fabrication of an integrated nanofluidic chip using interferometric lithography," *Journal of Vacuum Science & Technology B,* vol. 21, pp. 2941-2945, 2003.

[115] C. Ross, S. Haratani, F. Castano, Y. Hao, M. Hwang, M. Shima, *et al.*, "Magnetic behavior of lithographically patterned particle arrays," *Journal of applied physics,* vol. 91, pp. 6848-6853, 2002.

[116] C. Trompoukis, I. Abdo, R. Cariou, I. Cosme, W. Chen, O. Deparis, *et al.*, "Photonic nanostructures for advanced light trapping in thin crystalline silicon solar cells," *physica status solidi (a),* vol. 212, pp. 140-155, 2015.

[117] D. Xia, A. Biswas, D. Li, and S. R. Brueck, "Directed Self-Assembly of Silica Nanoparticles into Nanometer-Scale Patterned Surfaces Using Spin-Coating," *Advanced Materials,* vol. 16, pp. 1427-1432, 2004.

[118] T. Siegfried, M. Kind, A. Terfort, O. J. Martin, M. Zharnikov, N. Ballav, *et al.*, "Reusable plasmonic substrates fabricated by interference lithography: a platform for systematic sensing studies," *Journal of Raman Spectroscopy,* vol. 44, pp. 170-175, 2013.

[119] C. Lim, M. Hong, Y. Lin, Q. Xie, B. Luk'yanchuk, A. S. Kumar, *et al.*, "Microlens array fabrication by laser interference lithography for super-resolution surface nanopatterning," *Applied physics letters,* vol. 89, p. 191125, 2006.

[120] M. Farhoud, M. Hwang, H. I. Smith, M. Schattenburg, J. Bae, K. Youcef-Toumi, *et al.*, "Fabrication of large area nanostructured magnets by interferometric lithography," *IEEE transactions on magnetics,* vol. 34, pp. 1087-1089, 1998.

[121] C. G. Chen, P. T. Konkola, R. K. Heilmann, G. Pati, and M. L. Schattenburg, "Image metrology and system controls for scanning beam interference

lithography," *Journal of Vacuum Science & Technology B,* vol. 19, pp. 2335-2341, 2001.

[122] Q. Xie, M. Hong, H. Tan, G. Chen, L. Shi, and T. Chong, "Fabrication of nanostructures with laser interference lithography," *Journal of alloys and compounds,* vol. 449, pp. 261-264, 2008.

[123] M. E. Walsh, "On the design of lithographic interferometers and their application," Massachusetts Institute of Technology, 2004.

[124] R. Ji, "Templated fabrication of periodic nanostructures based on laser interference lithography," Ph. D. dissertation, Martin-Luther-Universität Halle-Wittenberg, 2008.

[125] W. Jung, F. Castaño, C. Ross, R. Menon, A. Patel, E. E. Moon, *et al.*, "Elliptical-ring magnetic arrays fabricated using zone-plate-array lithography," *Journal of Vacuum Science & Technology B,* vol. 22, pp. 3335-3338, 2004.

[126] H. Seidel, L. Csepregi, A. Heuberger, and H. Baumgärtel, "Anisotropic etching of crystalline silicon in alkaline solutions I. Orientation dependence and behavior of passivation layers," *Journal of the electrochemical society,* vol. 137, pp. 3612-3626, 1990.

[127] S. Y. Chou, P. R. Krauss, and P. J. Renstrom, "Imprint lithography with 25-nanometer resolution," *Science,* vol. 272, pp. 85-87, Apr 5 1996.

[128] K. Mohamed, M. Alkaisi, and R. Blaikie, "The replication of three dimensional structures using UV curable nanoimprint lithography," *Journal of Vacuum Science & Technology B,* vol. 26, pp. 2500-2503, 2008.

[129] S. Y. Chou, P. R. Krauss, W. Zhang, L. Guo, and L. Zhuang, "Sub-10 nm imprint lithography and applications," *Journal of Vacuum Science & Technology B,* vol. 15, pp. 2897-2904, 1997.

[130] S. Y. Chou, P. R. Krauss, and P. J. Renstrom, "Imprint of sub-25 nm vias and trenches in polymers," *Applied physics letters,* vol. 67, pp. 3114-3116, 1995.

[131] S. H. Ahn and L. J. Guo, "High-speed roll-to-roll nanoimprint lithography on flexible plastic substrates," *Advanced materials,* vol. 20, pp. 2044-2049, 2008.

[132] T. Haatainen, P. Majander, T. Riekkinen, and J. Ahopelto, "Nickel stamp fabrication using step & stamp imprint lithography," *Microelectronic Engineering,* vol. 83, pp. 948-950, 2006.

[133] M. Vogler, S. Wiedenberg, M. Mühlberger, I. Bergmair, T. Glinsner, H. Schmidt, *et al.*, "Development of a novel, low-viscosity UV-curable polymer system for

UV-nanoimprint lithography," *Microelectronic engineering,* vol. 84, pp. 984-988, 2007.

[134] U. Plachetka, M. Bender, A. Fuchs, B. Vratzov, T. Glinsner, F. Lindner, *et al.*, "Wafer scale patterning by soft UV-nanoimprint lithography," *Microelectronic Engineering,* vol. 73, pp. 167-171, 2004.

[135] J. Lee, S. Park, K. Choi, and G. Kim, "Nano-scale patterning using the roll typed UV-nanoimprint lithography tool," *Microelectronic Engineering,* vol. 85, pp. 861-865, 2008.

[136] A. Fuchs, M. Bender, U. Plachetka, L. Kock, N. Koo, T. Wahlbrink, *et al.*, "Lithography potentials of UV-nanoimprint," *Current Applied Physics,* vol. 8, pp. 669-674, 2008.

[137] M. C. McAlpine, R. S. Friedman, and C. M. Lieber, "Nanoimprint lithography for hybrid plastic electronics," *Nano Letters,* vol. 3, pp. 443-445, 2003.

[138] W. Zhang and S. Y. Chou, "Fabrication of 60-nm transistors on 4-in. wafer using nanoimprint at all lithography levels," *Applied physics letters,* vol. 83, pp. 1632-1634, 2003.

[139] D. Pisignano, L. Persano, E. Mele, P. Visconti, M. Anni, G. Gigli, *et al.*, "First-order imprinted organic distributed feedback lasers," *Synthetic metals,* vol. 153, pp. 237-240, 2005.

[140] X. Cheng, Y. Hong, J. Kanicki, and L. J. Guo, "High-resolution organic polymer light-emitting pixels fabricated by imprinting technique," *Journal of Vacuum Science & Technology B,* vol. 20, pp. 2877-2880, 2002.

[141] D. Cheyns, K. Vasseur, C. Rolin, J. Genoe, J. Poortmans, and P. Heremans, "Nanoimprinted semiconducting polymer films with 50 nm features and their application to organic heterojunction solar cells," *Nanotechnology,* vol. 19, p. 424016, 2008.

[142] S.-W. Ahn, K.-D. Lee, J.-S. Kim, S. H. Kim, J.-D. Park, S.-H. Lee, *et al.*, "Fabrication of a 50 nm half-pitch wire grid polarizer using nanoimprint lithography," *Nanotechnology,* vol. 16, p. 1874, 2005.

[143] J. Martın, J. Nogues, K. Liu, J. Vicent, and I. K. Schuller, "Ordered magnetic nanostructures: fabrication and properties," *Journal of magnetism and magnetic materials,* vol. 256, pp. 449-501, 2003.

[144] D. Falconnet, D. Pasqui, S. Park, R. Eckert, H. Schift, J. Gobrecht, *et al.*, "A novel approach to produce protein nanopatterns by combining nanoimprint lithography and molecular self-assembly," *Nano Letters,* vol. 4, pp. 1909-1914, 2004.

[145] H. Cao, J. O. Tegenfeldt, R. H. Austin, and S. Y. Chou, "Gradient nanostructures for interfacing microfluidics and nanofluidics," *Applied Physics Letters,* vol. 81, pp. 3058-3060, 2002.

[146] S. Park, H. Schift, C. Padeste, B. Schnyder, R. Kötz, and J. Gobrecht, "Anti-adhesive layers on nickel stamps for nanoimprint lithography," *Microelectronic Engineering,* vol. 73, pp. 196-201, 2004.

[147] R. Jaszewski, H. Schift, B. Schnyder, A. Schneuwly, and P. Gröning, "The deposition of anti-adhesive ultra-thin teflon-like films and their interaction with polymers during hot embossing," *Applied surface science,* vol. 143, pp. 301-308, 1999.

[148] J. Y. Kim, D.-G. Choi, J.-H. Jeong, and E.-S. Lee, "UV-curable nanoimprint resin with enhanced anti-sticking property," *Applied Surface Science,* vol. 254, pp. 4793-4796, 2008.

[149] H. Schift, S. Saxer, S. Park, C. Padeste, U. Pieles, and J. Gobrecht, "Controlled co-evaporation of silanes for nanoimprint stamps," *Nanotechnology,* vol. 16, p. S171, 2005.

[150] M. Beck, M. Graczyk, I. Maximov, E.-L. Sarwe, T. Ling, M. Keil, *et al.*, "Improving stamps for 10 nm level wafer scale nanoimprint lithography," *Microelectronic Engineering,* vol. 61, pp. 441-448, 2002.

[151] E.-J. Jang, Y.-B. Park, H.-J. Lee, D.-G. Choi, J.-H. Jeong, E.-S. Lee, *et al.*, "Effect of surface treatments on interfacial adhesion energy between UV-curable resist and glass wafer," *International Journal of Adhesion and Adhesives,* vol. 29, pp. 662-669, 2009.

[152] K. Söderström, J. Escarré, O. Cubero, F. J. Haug, S. Perregaux, and C. Ballif, "UV-nano-imprint lithography technique for the replication of back reflectors for n-i-p thin film silicon solar cells," *Progress in Photovoltaics: Research and Applications,* vol. 19, pp. 202-210, 2011.

[153] J. Escarre, K. Söderström, C. Battaglia, F.-J. Haug, and C. Ballif, "High fidelity transfer of nanometric random textures by UV embossing for thin film solar cells applications," *Solar Energy Materials and Solar Cells,* vol. 95, pp. 881-886, 2011.

[154] G. Jorgensen, K. Terwilliger, J. DelCueto, S. Glick, M. Kempe, J. Pankow, *et al.*, "Moisture transport, adhesion, and corrosion protection of PV module packaging materials," *Solar Energy Materials and Solar Cells,* vol. 90, pp. 2739-2775, 2006.

[155] J. H. Shin, K. S. Han, and H. Lee, "Anti-reflection and hydrophobic characteristics of M-PDMS based moth-eye nano-patterns on protection glass of photovoltaic systems," *Progress in Photovoltaics: Research and Applications,* vol. 19, pp. 339-344, 2011.

[156] J. Son, S. Kundu, L. K. Verma, M. Sakhuja, A. J. Danner, C. S. Bhatia, *et al.*, "A practical superhydrophilic self cleaning and antireflective surface for outdoor photovoltaic applications," *Solar Energy Materials and Solar Cells,* vol. 98, pp. 46-51, 2012.

[157] K.-S. Han, H. Lee, D. Kim, and H. Lee, "Fabrication of anti-reflection structure on protective layer of solar cells by hot-embossing method," *Solar Energy Materials and Solar Cells,* vol. 93, pp. 1214-1217, 2009.

[158] G. Kang, K. Bae, M. Nam, D.-H. Ko, K. Kim, and W. J. Padilla, "Broadband and ultrahigh optical haze thin films with self-aggregated alumina nanowire bundles for photovoltaic applications," *Energy & Environmental Science,* vol. 8, pp. 2650-2656, 2015.

[159] J. W. Leem and J. S. Yu, "Artificial inverted compound eye structured polymer films with light-harvesting and self-cleaning functions for encapsulated III–V solar cell applications," *RSC Advances,* vol. 5, pp. 60804-60813, 2015.

[160] V. E. Ferry, M. A. Verschuuren, M. C. v. Lare, R. E. Schropp, H. A. Atwater, and A. Polman, "Optimized spatial correlations for broadband light trapping nanopatterns in high efficiency ultrathin film a-Si: H solar cells," *Nano letters,* vol. 11, pp. 4239-4245, 2011.

[161] A. Bessonov, Y. Cho, S.-J. Jung, E.-A. Park, E.-S. Hwang, J.-W. Lee, *et al.*, "Nanoimprint patterning for tunable light trapping in large-area silicon solar cells," *Solar Energy Materials and Solar Cells,* vol. 95, pp. 2886-2892, 2011.

[162] A. Mellor, H. Hauser, C. Wellens, J. Benick, J. Eisenlohr, M. Peters, *et al.*, "Nanoimprinted diffraction gratings for crystalline silicon solar cells: implementation, characterization and simulation," *Optics express,* vol. 21, pp. A295-A304, 2013.

[163] Y. M. Song, H. J. Choi, J. S. Yu, and Y. T. Lee, "Design of highly transparent glasses with broadband antireflective subwavelength structures," *Optics express,* vol. 18, pp. 13063-13071, 2010.

[164] J. W. Leem, Y. Yeh, and J. S. Yu, "Enhanced transmittance and hydrophilicity of nanostructured glass substrates with antireflective properties using disordered gold nanopatterns," *Optics express,* vol. 20, pp. 4056-4066, 2012.

[165] S. H. Lee, J. W. Leem, and J. S. Yu, "Transmittance enhancement of sapphires with antireflective subwavelength grating patterned UV polymer surface structures by soft lithography," *Optics express,* vol. 21, pp. 29298-29303, 2013.

[166] B. Dudem, J. W. Leem, J. H. Lim, S. H. Lee, and J. S. Yu, "Multifunctional polymers with biomimetic compound architectures via nanoporous AAO films for efficient solar energy harvesting in dye-sensitized solar cells," *RSC Advances,* vol. 5, pp. 90103-90110, 2015.

[167] B. Janthong, Y. Moriya, A. Hongsingthong, P. Sichanugrist, and M. Konagai, "Management of light-trapping effect for a-Si: H/μc-Si: H tandem solar cells using novel substrates, based on MOCVD ZnO and etched white glass," *Solar Energy Materials and Solar Cells,* vol. 119, pp. 209-213, 2013.

[168] C.-H. Ho, D.-H. Lien, H.-C. Chang, C.-A. Lin, C.-F. Kang, M.-K. Hsing, *et al.*, "Hierarchical structures consisting of SiO 2 nanorods and p-GaN microdomes for efficiently harvesting solar energy for InGaN quantum well photovoltaic cells," *Nanoscale,* vol. 4, pp. 7346-7349, 2012.

[169] C.-A. Lin, K.-Y. Lai, W.-C. Lien, and J.-H. He, "An efficient broadband and omnidirectional light-harvesting scheme employing a hierarchical structure based on a ZnO nanorod/Si 3 N 4-coated Si microgroove on 5-inch single crystalline Si solar cells," *Nanoscale,* vol. 4, pp. 6520-6526, 2012.

[170] B. Qi and J. Wang, "Fill factor in organic solar cells," *Physical Chemistry Chemical Physics,* vol. 15, pp. 8972-8982, 2013.

[171] Y. D. Kim, J. H. Shin, J. Y. Cho, H. J. Choi, and H. Lee, "Nanosized patterned protective glass exhibiting high transmittance and self-cleaning effects for photovoltaic systems," *physica status solidi (a),* vol. 211, pp. 1822-1827, 2014.

[172] A. Cassie and S. Baxter, "Wettability of porous surfaces," *Transactions of the Faraday Society,* vol. 40, pp. 546-551, 1944.

[173] A. Tserepi, M. Vlachopoulou, and E. Gogolides, "Nanotexturing of poly (dimethylsiloxane) in plasmas for creating robust super-hydrophobic surfaces," *Nanotechnology,* vol. 17, p. 3977, 2006.

[174] K.-C. Park, H. J. Choi, C.-H. Chang, R. E. Cohen, G. H. McKinley, and G. Barbastathis, "Nanotextured silica surfaces with robust superhydrophobicity and omnidirectional broadband supertransmissivity," *ACS nano,* vol. 6, pp. 3789-3799, 2012.

[175] W. K. Cho and I. S. Choi, "Fabrication of hairy polymeric films inspired by geckos: wetting and high adhesion properties," *Advanced Functional Materials,* vol. 18, pp. 1089-1096, 2008.

[176] W. L. Min, B. Jiang, and P. Jiang, "Bioinspired Self-Cleaning Antireflection Coatings," *Advanced Materials,* vol. 20, pp. 3914-3918, 2008.

[177] B. Wang, T. Gao, and P. W. Leu, "Broadband light absorption enhancement in ultrathin film crystalline silicon solar cells with high index of refraction nanosphere arrays," *Nano Energy,* vol. 19, pp. 471-475, 2016.

[178] C. M. Hsu, C. Battaglia, C. Pahud, Z. Ruan, F. J. Haug, S. Fan, *et al.*, "High-Efficiency Amorphous Silicon Solar Cell on a Periodic Nanocone Back Reflector," *Advanced Energy Materials,* vol. 2, pp. 628-633, 2012.

[179] M. Moreno, D. Daineka, and P. R. i Cabarrocas, "Plasma texturing for silicon solar cells: From pyramids to inverted pyramids-like structures," *Solar Energy Materials and Solar Cells,* vol. 94, pp. 733-737, 2010.

[180] W. Wu, M. Hu, F. S. Ou, Z. Li, and R. S. Williams, "Cones fabricated by 3D nanoimprint lithography for highly sensitive surface enhanced Raman spectroscopy," *Nanotechnology,* vol. 21, p. 255502, 2010.

[181] L. Tsakalakos, J. Balch, J. Fronheiser, B. Korevaar, O. Sulima, and J. Rand, "Silicon nanowire solar cells," *Applied Physics Letters,* vol. 91, p. 233117, 2007.

[182] R. A. Puglisi, C. Garozzo, C. Bongiorno, S. Di Franco, M. Italia, G. Mannino, *et al.*, "Molecular doping applied to Si nanowires array based solar cells," *Solar Energy Materials and Solar Cells,* vol. 132, pp. 118-122, 2015.

[183] W. Xie, J. Oh, and W. Shen, "Realization of effective light trapping and omnidirectional antireflection in smooth surface silicon nanowire arrays," *Nanotechnology,* vol. 22, p. 065704, 2011.

[184] T. Gao, E. Stevens, J.-k. Lee, and P. W. Leu, "Designing metal hemispheres on silicon ultrathin film solar cells for plasmonic light trapping," *Optics letters,* vol. 39, pp. 4647-4650, 2014.

[185] S. Linic, P. Christopher, and D. B. Ingram, "Plasmonic-metal nanostructures for efficient conversion of solar to chemical energy," *Nature materials,* vol. 10, pp. 911-921, 2011.

[186] L.-B. Luo, C. Xie, X.-H. Wang, Y.-Q. Yu, C.-Y. Wu, H. Hu, *et al.*, "Surface plasmon resonance enhanced highly efficient planar silicon solar cell," *Nano Energy,* vol. 9, pp. 112-120, 2014.

[187] D. Shir, J. Yoon, D. Chanda, J.-H. Ryu, and J. A. Rogers, "Performance of ultrathin silicon solar microcells with nanostructures of relief formed by soft imprint lithography for broad band absorption enhancement," *Nano letters,* vol. 10, pp. 3041-3046, 2010.

[188] M. D. Kelzenberg, S. W. Boettcher, J. A. Petykiewicz, D. B. Turner-Evans, M. C. Putnam, E. L. Warren, *et al.*, "Enhanced absorption and carrier collection in Si wire arrays for photovoltaic applications," *Nature materials,* vol. 9, pp. 239-244, 2010.

[189] M. D. Kelzenberg, D. B. Turner-Evans, M. C. Putnam, S. W. Boettcher, R. M. Briggs, J. Y. Baek, *et al.*, "High-performance Si microwire photovoltaics," *Energy & Environmental Science,* vol. 4, pp. 866-871, 2011.

[190] H. Kim, A. Pique, J. Horwitz, H. Mattoussi, H. Murata, Z. Kafafi, *et al.*, "Indium tin oxide thin films for organic light-emitting devices," *Applied physics letters,* vol. 74, pp. 3444-3446, 1999.

[191] G. Li, C.-W. Chu, V. Shrotriya, J. Huang, and Y. Yang, "Efficient inverted polymer solar cells," *Applied Physics Letters,* vol. 88, pp. 253503-253503-3, 2006.

[192] N. Patel, P. Patel, and V. Vaishnav, "Indium tin oxide (ITO) thin film gas sensor for detection of methanol at room temperature," *Sensors and Actuators B: Chemical,* vol. 96, pp. 180-189, 2003.

[193] H. Liu, V. Avrutin, N. Izyumskaya, Ü. Özgür, and H. Morkoç, "Transparent conducting oxides for electrode applications in light emitting and absorbing devices," *Superlattices and Microstructures,* vol. 48, pp. 458-484, 2010.

[194] S. Najwa, A. Shuhaimi, N. Ameera, K. Hakim, M. Sobri, M. Mazwan, *et al.*, "The effect of sputtering pressure on structural, optical and electrical properties of

indium tin oxide nanocolumns prepared by radio frequency (RF) magnetron sputtering," *Superlattices and Microstructures*, vol. 72, pp. 140-147, 2014.

[195] A. Amaral, P. Brogueira, C. N. De Carvalho, and G. Lavareda, "Early stage growth structure of indium tin oxide thin films deposited by reactive thermal evaporation," *Surface and Coatings Technology*, vol. 125, pp. 151-156, 2000.

[196] D. Kim, Y. Han, J.-S. Cho, and S.-K. Koh, "Low temperature deposition of ITO thin films by ion beam sputtering," *Thin Solid Films*, vol. 377, pp. 81-86, 2000.

[197] J. H. Kim, K. A. Jeon, G. H. Kim, and S. Y. Lee, "Electrical, structural, and optical properties of ITO thin films prepared at room temperature by pulsed laser deposition," *Applied surface science*, vol. 252, pp. 4834-4837, 2006.

[198] T. Maruyama and K. Fukui, "Indium tin oxide thin films prepared by chemical vapour deposition," *Thin solid films*, vol. 203, pp. 297-302, 1991.

[199] S. Rozati and T. Ganj, "Transparent conductive Sn-doped indium oxide thin films deposited by spray pyrolysis technique," *Renewable Energy*, vol. 29, pp. 1671-1676, 2004.

[200] K. Ellmer and T. Welzel, "Reactive magnetron sputtering of transparent conductive oxide thin films: Role of energetic particle (ion) bombardment," *Journal of Materials Research*, vol. 27, pp. 765-779, 2012.

[201] H. Park, S. Q. Hussain, S. Velumani, A. H. T. Le, S. Ahn, S. Kim, *et al.*, "Influence of working pressure on the structural, optical and electrical properties of sputter deposited AZO thin films," *Materials Science in Semiconductor Processing*, 2015.

[202] D. Song, "Effects of rf power on surface-morphological, structural and electrical properties of aluminium-doped zinc oxide films by magnetron sputtering," *applied surface science*, vol. 254, pp. 4171-4178, 2008.

[203] Y. J. Kim, S. B. Jin, S. I. Kim, Y. S. Choi, I. S. Choi, and J. G. Han, "Effect of oxygen flow rate on ITO thin films deposited by facing targets sputtering," *Thin Solid Films*, vol. 518, pp. 6241-6244, 2010.

[204] H.-C. Lee and O. O. Park, "Electron scattering mechanisms in indium-tin-oxide thin films: grain boundary and ionized impurity scattering," *Vacuum*, vol. 75, pp. 275-282, 2004.

[205] F. Adurodija, H. Izumi, T. Ishihara, H. Yoshioka, M. Motoyama, and K. Murai, "Influence of substrate temperature on the properties of indium oxide thin films," *Journal of Vacuum Science & Technology A*, vol. 18, pp. 814-818, 2000.

[206] Y. Shigesato, R. Koshi-Ishi, T. Kawashima, and J. Ohsako, "Early stages of ITO deposition on glass or polymer substrates," *Vacuum*, vol. 59, pp. 614-621, 2000.

[207] R. Buzio, E. Gnecco, C. Boragno, U. Valbusa, P. Piseri, E. Barborini, *et al.*, "Self-affine properties of cluster-assembled carbon thin films," *Surface science*, vol. 444, pp. L1-L6, 2000.

[208] H. Kim, J. Horwitz, G. Kushto, A. Pique, Z. Kafafi, C. Gilmore, *et al.*, "Effect of film thickness on the properties of indium tin oxide thin films," *Journal of Applied Physics*, vol. 88, pp. 6021-6025, 2000.

[209] H. R. Fallah, M. Ghasemi, A. Hassanzadeh, and H. Steki, "The effect of deposition rate on electrical, optical and structural properties of tin-doped indium oxide (ITO) films on glass at low substrate temperature," *Physica B: Condensed Matter*, vol. 373, pp. 274-279, 2006.

[210] S. Ishibashi, Y. Higuchi, Y. Ota, and K. Nakamura, "Low resistivity indium–tin oxide transparent conductive films. II. Effect of sputtering voltage on electrical property of films," *Journal of Vacuum Science & Technology A*, vol. 8, pp. 1403-1406, 1990.

[211] E. Burstein, "Anomalous optical absorption limit in InSb," *Physical Review*, vol. 93, p. 632, 1954.

[212] T. Moss, "The interpretation of the properties of indium antimonide," *Proceedings of the Physical Society. Section B*, vol. 67, p. 775, 1954.

[213] G. Haacke, "New figure of merit for transparent conductors," *Journal of Applied Physics*, vol. 47, pp. 4086-4089, 1976.

[214] B. Chen, X. Sun, and B. Tay, "Fabrication of ITO thin films by filtered cathodic vacuum arc deposition," *Materials Science and Engineering: B*, vol. 106, pp. 300-304, 2004.

[215] T. Maruyama and K. Fukui, "Indium-tin oxide thin films prepared by chemical vapor deposition," *Journal of applied physics*, vol. 70, pp. 3848-3851, 1991.

[216] M. Chuang, "ITO films prepared by long-throw magnetron sputtering without oxygen partial pressure," *Journal of Materials Science & Technology*, vol. 26, pp. 577-583, 2010.

[217] K. Forberich, G. Dennler, M. C. Scharber, K. Hingerl, T. Fromherz, and C. J. Brabec, "Performance improvement of organic solar cells with moth eye anti-reflection coating," *Thin Solid Films*, vol. 516, pp. 7167-7170, 2008.

[218] D.-H. Ko, J. R. Tumbleston, L. Zhang, S. Williams, J. M. DeSimone, R. Lopez, *et al.*, "Photonic crystal geometry for organic solar cells," *Nano letters*, vol. 9, pp. 2742-2746, 2009.

[219] X. Li, W. C. Choy, L. Huo, F. Xie, W. E. Sha, B. Ding, *et al.*, "Dual plasmonic nanostructures for high performance inverted organic solar cells," *Advanced Materials*, vol. 24, pp. 3046-3052, 2012.

[220] S. Mokkapati, F. Beck, A. Polman, and K. Catchpole, "Designing periodic arrays of metal nanoparticles for light-trapping applications in solar cells," *Applied Physics Letters*, vol. 95, p. 053115, 2009.

[221] J. You, X. Li, F. x. Xie, W. E. Sha, J. H. Kwong, G. Li, *et al.*, "Surface Plasmon and Scattering-Enhanced Low-Bandgap Polymer Solar Cell by a Metal Grating Back Electrode," *Advanced Energy Materials*, vol. 2, pp. 1203-1207, 2012.

[222] S. Y. Chou and W. Ding, "Ultrathin, high-efficiency, broad-band, omni-acceptance, organic solar cells enhanced by plasmonic cavity with subwavelength hole array," *Optics express*, vol. 21, pp. A60-A76, 2013.

[223] D.-H. Ko, J. R. Tumbleston, A. Gadisa, M. Aryal, Y. Liu, R. Lopez, *et al.*, "Light-trapping nano-structures in organic photovoltaic cells," *Journal of Materials Chemistry*, vol. 21, pp. 16293-16303, 2011.

[224] D. H. Wang, D.-G. Choi, K.-J. Lee, J.-H. Jeong, S. H. Jeon, O. O. Park, *et al.*, "Effect of the ordered 2D-dot nano-patterned anode for polymer solar cells," *Organic Electronics*, vol. 11, pp. 285-290, 2010.

[225] Y. Wang, X. Zhang, B. Han, L. Bai, H. Zhao, F. Yang, *et al.*, "UV micro-imprint patterning for tunable light trapping in pin thin-film silicon solar cells," *Applied Surface Science*, vol. 355, pp. 14-18, 2015.

[226] U. Paetzold, M. Smeets, M. Meier, K. Bittkau, T. Merdzhanova, V. Smirnov, *et al.*, "Disorder improves nanophotonic light trapping in thin-film solar cells," *Applied physics letters*, vol. 104, p. 131102, 2014.

[227] P. Wang, S. Azimi, M. B. Breese, and M. Peters, "Theoretical investigation of "nano-muffin" and inverted nano-pyramid surface textures for energy harvesting in very thin c-Si solar cells," in *MRS Proceedings*, 2014, pp. mrsf13-1638-w05-20.

[228] M. S. Branham, W. C. Hsu, S. Yerci, J. Loomis, S. V. Boriskina, B. R. Hoard, *et al.*, "15.7% Efficient 10-µm-Thick Crystalline Silicon Solar Cells Using Periodic Nanostructures," *Advanced Materials*, vol. 27, pp. 2182-2188, 2015.

[229] B. Jia, "Nanophotonics silicon solar cells: status and future challenges," *Nanotechnology Reviews*, vol. 4, pp. 337-346, 2015.

[230] H. A. Atwater and A. Polman, "Plasmonics for improved photovoltaic devices," *Nature materials*, vol. 9, pp. 205-213, 2010.

[231] V. E. Ferry, M. A. Verschuuren, H. B. Li, E. Verhagen, R. J. Walters, R. E. Schropp, *et al.*, "Light trapping in ultrathin plasmonic solar cells," *Optics express*, vol. 18, pp. A237-A245, 2010.

[232] H. Huang, L. Lu, J. Wang, J. Yang, S.-F. Leung, Y. Wang, *et al.*, "Performance enhancement of thin-film amorphous silicon solar cells with low cost nanodent plasmonic substrates," *Energy & Environmental Science*, vol. 6, pp. 2965-2971, 2013.

[233] J. Zhu, Z. Yu, G. F. Burkhard, C.-M. Hsu, S. T. Connor, Y. Xu, *et al.*, "Optical absorption enhancement in amorphous silicon nanowire and nanocone arrays," *Nano letters*, vol. 9, pp. 279-282, 2008.

[234] T. Kelf, Y. Sugawara, R. Cole, J. Baumberg, M. Abdelsalam, S. Cintra, *et al.*, "Localized and delocalized plasmons in metallic nanovoids," *Physical Review B*, vol. 74, p. 245415, 2006.

[235] P. Matheu, S. Lim, D. Derkacs, C. McPheeters, and E. Yu, "Metal and dielectric nanoparticle scattering for improved optical absorption in photovoltaic devices," *Applied physics letters*, vol. 93, p. 113108, 2008.

[236] D. Wan, H. L. Chen, T. C. Tseng, C. Y. Fang, Y. S. Lai, and F. Y. Yeh, "Antireflective nanoparticle arrays enhance the efficiency of silicon solar cells," *Advanced Functional Materials*, vol. 20, pp. 3064-3075, 2010.

Appendix A-List of equipment used in this research work

Figure A-1: The Edwards Auto500 Magnetron sputtering system for material deposition using DC, RF sputtering and e-beam evaporation techniques.

Figure A-2: The Balzers BA 510A thermal evaporator system for depositing materials.

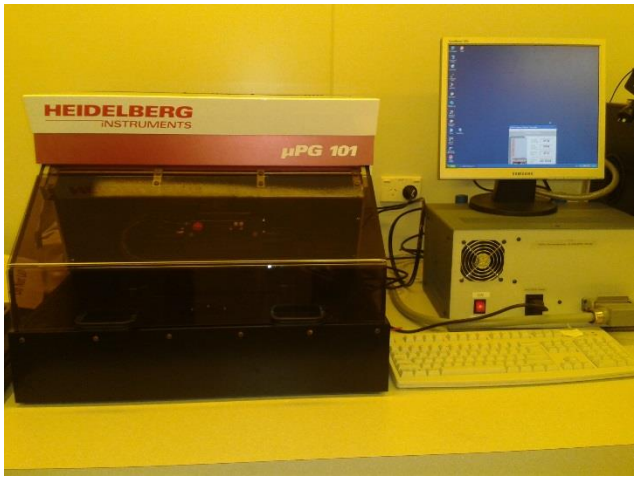

Figure A-3: The Heidelberg µPG101 Laser Mask Writer system for patterning mask.

Figure A-4: The Karl Suss mask aligner system (MA-6) for photolithography and UV-NIL.

Figure A-5: The Oxford Plasma 80plus Reactive Ion Etching System (RIE) for pattern transfer process.

Figure A-6: The Emitech K1050X oxygen plasma Asher for substrate cleaning and surface treatment.

Figure A-7: The Headway PWM32-PS-R790 spin coater for spin coating process.

Figure A-8: The quartz tube furnace for oxidation, diffusion and annealing process.

Figure A-9: The Elmasonic S 60H Ultrasonic bath from for ultrasonic cleaning process.

Figure A-10: The Lloyd's mirror laser interference lithography setup for patterning of the resist.

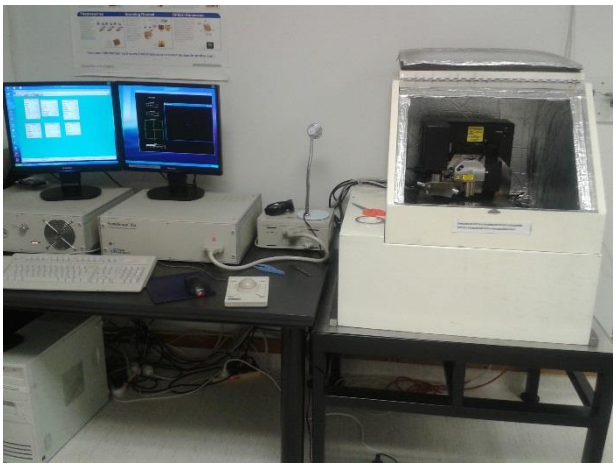

Figure A-11: The Digital Instruments Dimension 3100 Atomic Force Microscopy (AFM) system for imaging surface topography.

Figure A-12: The Au/Pd sputter coater from Polaron Equipment Ltd for SEM sample preparation.

Figure A-13: The Raith-150 electron beam lithography (EBL) system for imaging.

Figure A-14: The Veeco Dektak 150 profilometer system for surface profile tracing.

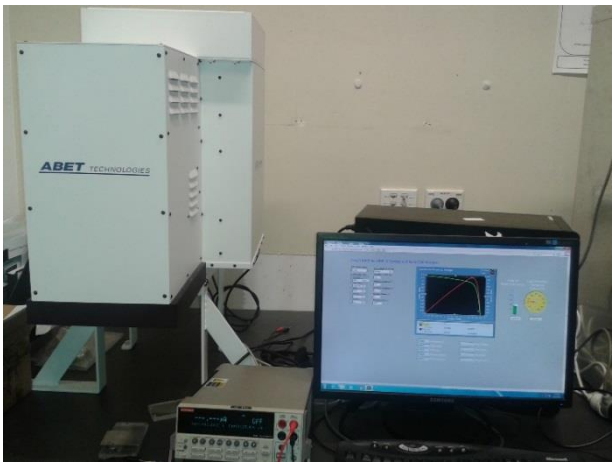

Figure A-15: The current density-voltage measurement setup for a solar cell using a solar simulator (ABET Sun3000) and Keithley 2400 source meter.

Figure A-16: The Van der Pauw Hall effect measurement setup for electrical measurements.

Figure A-17: The JEOL JSM 7000F field emission, high resolution scanning electron microscope for imaging.

Figure A-18: Cary Spectrophotometer 619 for transmittance measurements.

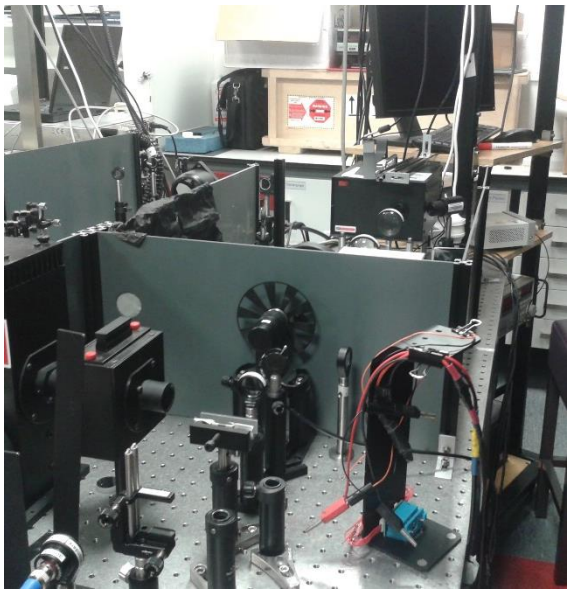

Figure A-19: A homebuilt typical setup for EQE measurements at Victoria University of Wellington.

Figure A-20: A contact angle goniometer with Edmund Scientific Camera for measuring surface wettability from Department of Chemistry, UC.

Figure A-21: The Tempress 602 dice saw system for cutting the substrates.

Figure A-22: A drying Oven from SANYO for baking samples.